An Implementation of an Optical Fourier-Transform Coprocessor using a Twisted-Nematic Liquid-Crystal Spatial Light Modulator

by

Pierre M. Lane

A Thesis Submitted to the
Faculty of Engineering
in Partial Fulfilment of the Requirements
for the Degree of

MASTER OF APPLIED SCIENCE

Major Subject: Electrical Engineering

APPROVED:

Dr. M. Cada, Supervisor

Dr. W. Robertson

Dr. W. Phillips

TECHNICAL UNIVERSITY OF NOVA SCOTIA

Halifax, Nova Scotia 1996

TECHNICAL UNIVERSITY OF NOVA SCOTIA LIBRARY

"Authority to Distribute Manuscript Thesis"

Title: An Implementation of an Optical Fourier-Transform Coprocessor using a Twisted-Nematic Liquid-Crystal Spatial Light Modulator

The above library may make available or authorize another library to make available individual photo/microfilm copies of this thesis without restrictions.

Full Name of Author: Pierre Mark Lane

Signature of Author: _____

Date: April 22, 1996

This thesis is dedicated
to my parents, Fenella and Alan Lane, for their
constant support and encouragement.

Table of Contents

List of Tables vii

List of Figures viii

List of Abbreviations and Symbols xii

Acknowledgements xvii

Abstract xviii

Introduction 1

1.1 Optical Computing 1
1.2 An Optical Fourier Transform Processor 2
1.3 Scope of the Thesis 3
1.4 Mathematical Preliminaries 4
1.4.1 Notation for Useful Functions 4
1.4.2 The Fourier Transform 5
1.4.3 Shift-Invariant Linear System 6
1.4.4 Wavefunction Nomenclature 7
1.4.5 Optical Intensity 9

Fourier Optics 10

2.1 Diffraction Theory 10
2.1.1 The Huygens-Fresnel Principle 13
2.1.2 Fresnel Diffraction 14
2.1.3 Fraunhofer Diffraction 16
2.2 Optical Fourier Transforming 18
2.2.1 Phase Transformation Introduced by a Lens 18
2.2.2 Transparency $t(x,y)$ Placed Immediately in Front of a Lens 21
2.2.3 Transparency $t(x,y)$ Placed a Distance d_o in Front of a Lens 23
2.3 Resolution of an Optical System 25

Liquid Crystal Spatial Light Modulators 27

3.1 Liquid Crystals 27
3.1.1 Nematic Phase 29
3.1.2 Smectic Phase 30
3.2 Switching in a Liquid Crystal 30
3.2.1 The Dielectric Effect 31
3.2.2 The Ferroelectric Effect 32
3.3 Liquid Crystal Devices 33
3.3.1 Field-Induced Birefringence Devices 33
3.3.2 Twisted Nematic (TN) Devices 35
3.3.3 Smectic-C* Ferroelectric Devices 37
3.3.4 Smectic A* Devices 39
3.4 Active Matrix Addressing 39
3.4.1 Thin-Film Transistors (TFTs) on a Transparent Substrate 40
3.4.2 VLSI on Single Crystal Silicon Substrate 40

The Optical Processor 42

4.1 Spatial Light Modulator Characterization 43
4.1.1 Pixel Pitch and Width 43
4.1.2 Voltage-Transmission 46
4.1.3 Response Time 48
4.1.4 Twist Angle 50
4.1.5 Summary of Specifications 53
4.2 The Optical Fourier Transform Processor 54
4.2.1 Helium-Neon Laser 55
4.2.2 Spatial Light Modulator 56
4.2.3 Fourier Lens 56
4.2.4 CCD Camera 57
4.3 Computer Control System and Software 58
4.3.1 SLM Video Signal 60
4.3.2 CCD Video Signal 60
4.3.3 Software 60

Experimental Results 62

5.1 Optical Fourier Transform Spectra 62
5.1.1 Bandwidth 63
5.1.2 Frequency Resolution 64
5.1.3 Modulation Transfer Function 66
5.1.4 Summary 72
5.2 Optical Fourier Transformer Characterization 73
5.2.1 Bandwidth 73
5.2.2 Frequency Resolution 74
5.3 Experimental Results 74
5.3.1 Constant Input 79
5.3.2 Single Cosinusoid Input 80
5.3.3 Multiple Cosinusoid Input 87

Summary and Conclusions 96

6.1 Analog and Digital Processing 96
6.2 Advantages and Disadvantages 97
6.3 Suggestions for Further Work 99
6.3.1 Increase Input Plane Size 99
6.3.2 Spatial Light Modulation 99
6.3.3 Recovery of Phase Information 100

List of References 102

List of Tables

Table 4-1:
Kodak LC500 spatial light modulator pixel pitch and width determined from the Fraunhofer diffraction pattern. 44

Table 4-2:
Measurements and the solution to TN-LCD twist angle equations. 53

Table 4-3:
Summary of the Kodak LC500 liquid crystal SLM specifications determined during its characterization. 54

Table 4-4:
Summary of the Pulnix TM-7AS CCD camera specifications. 57

Table 5-1:
SLM reconstruction parameters and their complementary frequency domain representations. 72

Table 5-2:
Summary of Optical Fourier Transformer Frequency Domain Specifications 73

Table 5-3:
Power spectra of functions containing a constant DC level and a single cosinusoid 80

Table 5-4:
Summary of power spectra containing a constant DC level and several cosinusoids. All spatial frequencies are in cycles/cm. 87

List of Figures

Figure 2-1: Diffraction of light by an aperture in an opaque screen indicating the regions where the Rayleigh-Sommerfeld, Fresnel, and Fraunhofer diffraction theories are valid. 11

Figure 2-2: Application of the Huygens-Fresnel principle to plane waves, spherical waves, and obstructed spherical waves. 14

Figure 2-3: Plane waves incident on a glass phase object of varying thickness $\Delta(x,y)$, maximum thickness Δ_0, and refractive index n. . . . 19

Figure 2-4: A transparency $t(x,y)$ placed immediately in front of a lens with focal length f and illuminated with plane waves. 22

Figure 2-5: A transparency $t(x,y)$ placed a distance d_o in front of a lens with focal length f and illuminated with plane waves. 24

Figure 3-1: Schematic representation of the (a) nematic, (b) smectic, and (c) cholesteric liquid crystal mesophases. 29

Figure 3-2: Schematic illustration of the induced birefringence effect (a) with no applied voltage; and (b) with an applied voltage $V > V_{TH}$. . . 34

Figure 3-3: Schematic illustration of the twisted nematic effect in a cell equipped with parallel polarizers for (a) zero applied voltage, (b) applied voltage $V > V_{TH}$, and (c) its transfer function. 36

Figure 3-4: Schematic representation of surface stabilized ferroelectric liquid crystal (SSFLC) bistability. The two possible ferroelectric polarizations point in the $\pm x$ directions. 38

Figure 4-1: Photograph of the twisted-nematic liquid crystal spatial light modulator removed from the Kodak LC500 video projector. The scale along the bottom is in centimeters. 44

Figure 4-2: Voltage-transmission curve for the Kodak LC500 SLM with parallel polarizers and optimized for minimum transmission at V = 120 mV. The voltage across the SLM is swept from 0 to 5 V rms. . . 47

Figure 4-3: Spatial light modulator rise time for 10% to 90% intensity change. (a) SLM driven directly with a function generator, (b) SLM driven with a CGA display card and LC500 video electronics. 49

Figure 4-4: Spatial light modulator decay time for 90% to 10% intensity change. (a) SLM driven directly with a function generator, (b) SLM driven with a CGA display card and LC500 video electronics. 50

Figure 4-5: Definition of the coordinate system and various angles in the measurement of the SLM twist angle. The Helium-Neon laser light is incident along the *z*-axis and directed out of the page. 51

Figure 4-6: Kodak LC500 TN-LCD twist angle characterization. The figure shows polarizer-analyzer orientation for minimum transmission and entrance-exit LC director orientation. 53

Figure 4-7: Schematic diagram of the optical Fourier transformer. A spatial domain input signal in the plane of the SLM is Fourier transformed into the output or frequency domain plane at the CCD array. 55

Figure 4-8: Block diagram of the optical Fourier transformer and computer control system. An input to the optical processor is generated by the CGA card and its transform is acquired by the CCD camera and frame grabber. 58

Figure 4-9: Photograph of the optical Fourier transformer. The HeNe laser is visible on the extreme left of the photograph followed by the polarizer, SLM, analyzer, lens, and CCD camera. 59

Figure 5-1: Spectrum of a sampled 1-D temporal signal and the transfer function of a zero-order hold interpolation function. The signal is sampled at $\nu' = 1/\Delta t$. 68

Figure 5-2: The modulation transfer function (MTF) and spectrum of a sampled 2-D signal along a co-ordinate axis for a SLM with square pixels and 100, 75, 50, and 25 percent fill factors. 70

Figure 5-3: Spatial bandwidth of the optical Fourier transformer along the ν_x-axis as defined by the zero-order sampled spectrum and its modulation transfer function (MTF). 74

Figure 5-4: Frequency resolution of the optical Fourier transformer. The figure shows the magnitude spectrum of unity input with the modulation transfer function. 75

Figure 5-5: The Liquid crystal SLM. The small box in the center of the screen indicates the area that is displayed in the SLM preview window and the black dot represents the circle in the preview window. 76

Figure 5-6: The SLM pixels illuminated by the 514 μm diameter beam. Beam intensity is shown and the SLM pixels illuminated by the Gaussian beam are indicated. The white boxes represent pixels and the shaded grid represents dead space. 77

Figure 5-7: The optical Fourier transform (power spectrum) of a constant input: (a) An illustration of the constant input function f(x,y) = 1 written to the SLM, and (b) its optical transform observed in the Fourier plane. 78

Figure 5-7(c): The zero-order spectrum from Figure 5-7(b). The Gaussian spike at the origin represents the DC component of the signal (ν_x = ν_y = 0). 79

Figure 5-8: The optical Fourier transform (power spectrum) of $f(x,y) = 1 + \cos(2\pi\upsilon_x x)$: (a) The input function written to the SLM, and (b) its optical transform observed in the Fourier plane. 81

Figure 5-8(c): The zero-order spectrum from Figure 5-8(b). The input function is $f(x,y) = 1 + \cos(2\pi\upsilon_x x)$, where $\nu_x = 63\text{cm}^{-1}$. 82

Figure 5-9: The optical Fourier transform (power spectrum) of $f(x,y) = 1 + \cos(2\pi\upsilon_y y)$: (a) The input function written to the SLM, and (b) its optical transform observed in the Fourier plane. 83

Figure 5-9(c): The zero-order spectrum from Figure 5-9(b). The input function is $f(x,y) = 1 + \cos(2\pi\upsilon_y y)$, where $\nu_y = 56\text{cm}^{-1}$. 84

Figure 5-10: The optical Fourier transform (power spectrum) of $f(x,y) = \cos[2\pi(\nu_x x + \nu_y y)]$: (a) The input function, and (b) its optical transform observed in the Fourier plane. 85

Figure 5-10(c): The zero-order spectrum from Figure 5-10(b). The input function is $f(x,y) = 1 + \cos[2\pi(63x + 56y)]$. 86

Figure 5-11: The optical Fourier transform (power spectrum) of $f(x,y) = 1 + \cos(2\pi\upsilon_0 y)$: (a) The input function, and (b) its optical transform observed in the Fourier plane. 88

Figure 5-11(c): The zero-order spectrum from Figure 5-11(b). The input function is $f(x,y) = 1 + \cos(2\pi\upsilon_0 y)$, where $\nu_1 = 27.8\text{cm}^{-1}$. 89

Figure 5-12: The optical Fourier transform (power spectrum) of $f(x,y) = 1 + \sum\cos(2\pi\upsilon_i y)$: (a) The input function, and (b) its optical transform observed in the Fourier plane. 90

Figure 5-12(c): The zero-order spectrum from Figure 5-12(b). The input function is $f(x,y) = 1 + \sum \cos(2\pi\upsilon_i y)$, where $\nu_1 = 18.5$, and $\nu_3 = 55.6\text{cm}^{-1}$. 91

Figure 5-13: The optical Fourier transform (power spectrum) of $f(x,y) = 1 + \sum\cos(2\pi\upsilon_i y)$: (a) The input function, and (b) its optical transform observed in the Fourier plane. 92

Figure 5-13(c): The zero-order spectrum of Figure 5-13(b). The input function is $f(x,y) = 1 + \sum \cos(2\pi\upsilon_i y)$, where $\nu_i = \{11.1, 33.4, 55.6\}$ cm^{-1}. 93

Figure 5-14: The optical Fourier transform (power spectrum) of $f(x,y) = 1 + \sum\cos(2\pi\upsilon_i y)$: (a) The input function, and (b) its optical transform observed in the Fourier plane. 94

Figure 5-14(c): The zero-order spectrum from Figure 5-14(b). The input function is $f(x,y) = 1 + \sum \cos(2\pi\upsilon_i y)$, where $\nu_i = \{8.1, 24.3, 40.4, 55.6\}$ cm^{-1}. 95

Figure 6-1: Processing an analog signal with (a) a digital signal processor, and (b) a digital signal processor with an optical coprocessor. 97

List of Abbreviations and Symbols

Greek Symbols

α	Arctan of the magnitude ratio a_y/a_x [rad]
γ	Dimensionless dummy variable, $\gamma = rD/\lambda f$
δ	Phase difference $\delta_y - \delta_x$ [rad]
δ_x, δ_y	Complex amplitude phase advance in the x- and y-directions [rad]
δx_{SLM}, δy_{SLM}	Width of SLM pixels [µm]
δx_{CCD}, δx_{CCD}	Width of CCD pixels [µm]
Δ_0	Maximum thickness of an optical element or lens [m]
$\Delta\epsilon$	Dielectric anisotropy of a liquid crystal [F/m]
$\Delta\nu$	Temporal frequency resolution [Hz]
$\Delta\nu_r$	Spatial frequency resolution [cm^{-1}]
Δn	Optical birefringence
Δt	Temporal sampling period [sec]
Δx_{SLM}, Δy_{SLM}	Pitch of SLM pixels [µm]
Δx_{CCD}, Δy_{CCD}	Pitch of CCD pixels [µm]
ϵ	Electric permittivity of a medium [F/m]
$\epsilon_\parallel$, $\epsilon_\perp$	Component of permittivity parallel/perpendicular to optic axis [F/m]
ϵ_0	Electric permittivity of free space [F/m]
θ	Arbitrary angle [rad]
θ_{max}	Ratio of r'_{max} over z [rad]
θ_t	Tilt angle in a smectic liquid crystal [rad]
Θ	Twisted nematic liquid crystal twist angle [rad]
λ	Wavelength [m]
ν	Temporal frequency [Hz]
ν'	Sampling frequency, spatial [cm^{-1}] or temporal [Hz]
ν_i	Harmonically related spatial frequencies, i = 1, 2, 3 ... [cm^{-1}]
ν_s	Spatial bandwidth of an imaging system [cm^{-1}]
ν_x, ν_y	Spatial frequency [cm^{-1}]
σ_x, σ_y	Power-rms width of Gaussian beam incident on SLM [m]
$\sigma_{\nu x}$, $\sigma_{\nu y}$	Spectral power-rms width [cm^{-1}]
ϕ	Arbitrary angle [rad]
ϕ_0	Angle ϕ_{ENT} for minimum transmission [rad]
$\phi`_0$	Iterative estimate of ϕ_0 [rad]
ϕ_{ENT}	Angle between x-axis and light polarization incident on SLM [rad]
ϕ_{EXT}	Angle between x-axis and TA-axis of exit polarizer [rad]
ϕ_{POL}	Angle between the entrance and exit polarizers [rad]
ϕ_{REF}	Angle between x-axis and $x`$-axis [rad]
ω	Temporal angular frequency [rad/sec]

Roman Symbols

a	Lens constant
a_x, a_y	Magnitudes of A_x and A_y [V/m]
A_x, A_y	Complex amplitude components in the x- and y-directions [V/m]
b	Lens constant
B	Temporal bandwidth of a sampled signal [Hz]
B_x, B_y	Spatial bandwidth of sampled signal [cm^{-1}]
c	Speed of light [m/s]
d	Distance or thickness of a liquid-crystal cell [m]
D	Diameter of a lens [m]
f	Focal length of a lens [m]
ENB_x, ENB_y	Effective noise bandwidth of a modulation transfer function [cm^{-1}]
E	Electric field vector [V/m] or [N/C]
i	Imaginary number $\sqrt{-1}$; Integer
I	Optical Intensity [W/m^2]
I_{ON}, I_{OFF}	Optical intensity transmitted in the ON- and OFF-states [W/m^2]
j	Integer
J	Jones vector
k	Wavevector [m^{-1}]
k_x, k_y, k_r	Spatial angular frequency or wave number [m^{-1}]
k_0	Free-space wave number [m^{-1}]
K_{11}, K_{22}, K_{33}	Liquid crystal elastic constants
n	Refractive index
$n_{\parallel}$, $n_{\perp}$	Refractive indices parallel and perpendicular to the optic axis
n_x, n_y	Integers
n	Director in a liquid crystal
N_F	Fresnel Number
N	Torque generated per unit volume [N/m^2]
m_x, m_y	Integers
$\mathbf{P_s}$	Spontaneous polarization vector [C/m^2]
q	Integer
r_0	Radius of a circular aperture [m]
r_{max}	Maximum radial dimension in an observation plane [m]
r_{max}	Maximum radial dimension of an aperture [m]
r_{min}	Minimum separation between two impulse-response functions [m]
r	Vector of Cartesian components (x,y,z)
R_1, R_2	Radius of curvature [m]
t	Time [sec]
t_{rise}	Liquid crystal rise time [sec]

t_{decay}	Liquid crystal decay time [sec]
$\mathbf{T}$	Jones matrix
T	Sampling interval [sec]; Temperature [°C]
T	Intensity [W/m^2] or power transmittance [W]; Transmission ratio
$T_{\parallel}$, $T_{\perp}$	Transmission ratio for parallel and crossed polarizers
u	Dimensionless parameter used in LC twist angle measurement
V	Voltage across a liquid crystal cell [V]
V_{ON}, V_{OFF}	Liquid crystal on- and off-voltages [V rms]
V_{TH}	Liquid crystal threshold voltage [V rms]
w_x, w_y	Waist radius of a Gaussian beam incident on the SLM [m]
x	Dummy variable used in LC twist angle measurement
x, y, z	Position coordinates in Cartesian coordinate system [m]
x', y'	Dummy variables for x and y [m]
x_0, y_0	Dimensions of a rectangular aperture [m]

Greek Functions

$\delta(x,y)$	Dirac delta or impulse function
$\Delta(x,y)$	Thickness function of an optical element or lens
$\Delta n(V)$	Optical birefringence in a liquid crystal cell
$\eta(T)$	Temperature-dependent liquid crystal viscosity
$\mathrm{III}(x,y)$	Sampling or replicating function
$\Pi(x,y)$	Rectangle function of unit height and base
$\phi(\mathbf{r})$	Phase of a complex wavefunction
$\phi(x,y)$	Phase advance introduced by a lens
$\Phi(x,y;f)$	Phase transformation introduced by a lens
$\psi(x,y,z,t)$	Arbitrary complex wavefunction
$\psi(x,y,z)$	Complex amplitude of an arbitrary wavefunction
$\psi_e(x,y)$	Complex envelope of an arbitrary wavefunction
$\psi_{e0}(x,y)$	Initial value of $\psi_e(x,y)$ at z=0
$\Psi(k_x,k_y)$	Fourier transform of $\psi_e(x,y,z)$

Roman Functions

$a(\mathbf{r})$	Amplitude of a complex wavefunction
$a_E(\mathbf{r})$	Amplitude of a complex wavefunction's electric field
$f(x)$	General functions of one or two variables
$f_s(x)$	Discrete function sampled from $f(x)$
$f_r(x)$	Continuous function reconstructed from $f_s(x)$
$F(\nu)$	Fourier transforms of general functions $f(x)$
$h(x,y)$	Impulse-response function of a linear system

$H(k_x,k_y)$	Transfer function of a linear system
$J_m(r)$	Bessel function of the first kind of order m
sinc(x)	Filtering or interpolation function
$t(x,y)$	Transparency function
$T(k_x,k_y)$	Fourier transform of $t(x,y)$
$w(x,y)$	Window function
$W(k_x,k_y)$	Fourier transform of window function $w(x)$

Operators and Mathematical Symbols

arg{•}	Phase of a complex value
$\mathcal{F}_t\{\cdot\}$	One-dimensional temporal Fourier Transform (minus-i)
$\mathcal{F}_t^{-1}\{\cdot\}$	Inverse one-dimensional temporal Fourier Transform (plus-i)
$\mathcal{F}_{xy}\{\cdot\}$	Two-dimensional spatial Fourier Transform (plus-i)
$\mathcal{F}_{xy}^{-1}\{\cdot\}$	Inverse two-dimensional spatial Fourier Transform (minus-i)
$f(t) * g(t)$	Convolution of $f(t)$ and $g(t)$
$f(t) \star g(t)$	Correlation of $f(t)$ and $g(t)$
∇^2	$\partial^2/\partial x^2 + \partial^2/\partial y^2$

Acronyms

ADC	Analog-to-Digital Converter
AGC	Automatic Gain Control
AMLCD	Active Matrix Liquid Display
CCD	Charge Coupled Device
CGA	Color Graphics Adaptor
CRT	Cathod Ray Tube
DAC	Digital-to-Analog Convertor
DFT	Discrete Fourier Transform
DMD	Deformable Mirror Device
DRAM	Dynamic Read Only Memory
DSP	Digital Signal Processor
ECE	ElectroClinic Effect
EGA	Extended Graphics Adaptor
ENB	Effective Noise Bandwidth
FET	Field Effect Transistor
FFT	Fast Fourier Transform
FLC	Ferroelectric Liquid Crystal
FLCD	Ferroelectric Liquid Crystal Display
LC	Liquid Crystal
LCD	Liquid Crystal Display

LCLV	Liquid Crystal Light Valve
LCTV	Liquid Crystal TeleVission
LHS	Left Hand Side
MOS	Metal Oxide Semiconductor
MTF	Modulation Transfer Function
OA	Optic Axis
OFT	Optical Fourier Transform
OTF	Optical Transfer Function
PC	Personal Computer
PLL	Phase Locked Loop
PMLCD	Passive Matrix Liquid Crystal Display
RHS	Right Hand Side
SLM	Spatial Light Modulator
SRAM	Static Read Only Memory
SSFLC	Surface Stabalized Ferroelectric Liquid Crystal
STN	Super Twisted Nematic
TEM	Transverse Electric Magnetic
TFT	Thin Film Transistor
TA	Transmission Axis
TN	Twisted Nematic
TV	TeleVission
VLSI	Very Large Scale Integration

Acknowledgements

I would like to thank my supervisor Dr. Michael Cada for suggesting the project, and for his guidance support, and encouragement during the course of the work. I would also like to thank Dr. Peter Gregson for his advice and expertise shared during several helpful discussions. Thanks to Dr. Zhou for his advice and assistance with optical equipment in the laboratory.

Support from the technical staff, in particular Mr. John Lee, Mr. Christopher Hill, Mr. Mark LeBlanc, and Mr. Joe Isenor is also appreciated. I also thank Mr. Ronnie Van Dommelen and Mr. Darren Hsiung for their participation and collaboration on the characterization and software phases of this project.

Financial support provided by TUNS, from Dr. Michael Cada, and Dr. Steven Knudsen, is gratefully acknowledged.

Abstract

The advantages of processing information with photons as opposed to electrons are well established; however, until recently, the technologies required to utilize these advantages have not been fully developed. This thesis describes the design, prototype construction, and characterization of an optical Fourier-transform processor based on a liquid-crystal (LC) spatial light modulator (SLM). The processor demonstrates the principles of optical computing and signal processing. In the optical Fourier processor, a twisted-nematic active-matrix liquid-crystal-display (TN-AMLCD) from a Kodak LC-500 video projector is used as a spatial light modulator in the front focal plane of a Fourier lens to calculate power spectra of arbitrary 2-D functions written to the SLM. A CCD camera and a frame grabber acquire the power spectra from the back focal plane of the Fourier lens. The SLM and frame grabber are interfaced to a 80386 computer with controlling software. Consequently, the system is capable of performing optical Fourier transforms at video frame rates. The SLM modulates the magnitude of incident wavefronts with an arbitrary 2-D input function and the CCD camera records the intensity of its Fourier transform. The power spectra of several 2-D sinusoidal input functions were processed with the optical processor. The processed spectra corresponded well with the results predicted by standard Fourier theory. The optical processor has the potential to process complex-valued inputs and provide complex-valued output.

Chapter 1
Introduction

The electronic digital computer has come a long way since ENIAC first glowed to life 50 years ago at the University of Pennsylvania. The modern computer has grown from a massive vacuum tube monster capable of a few thousand additions per second into an ubiquitous desktop thorough-bred built from VLSI (very large scale integration) technology and capable of millions, and in some cases even billions, of operations per second. This spectacular rate of growth, due to the invention of the transistor, the integrated circuit, and increasingly larger scales of integration, is slowing down as the capabilities of the electronic hardware nears its practical limit of size and efficiency. Any further leaps in computational power will need to be gained by exploiting more exotic technologies. These newer computational technologies will not replace conventional electronics, but will simply augment their computational power, specifically in power-hungry applications where the power of conventional electronics has been exhausted.

1.1 Optical Computing

At its very basic level, an optical computer is an information processing system that uses photons rather than electrons as the information carrier. There are several advantages to processing information with photons rather than electrons. Photons can pass through each other as if they were invisible without any mutual interference; an optical message can be transmitted over a single optical fiber in both directions simultaneously. The flow of electrons in a wire can be in only one direction. Photons propagate easily through free space and allow for massively parallel free-space optical inter-connects and cross-connects. A matrix of several thousand optical channels can operate in parallel,

each with a bandwidth much greater than that of any electronic circuit. The electrons of an electronic circuit must be routed through a conduit. Photons are charge neutral and are consequently immune to extraneous electro-magnetic interference. Electronic circuits are susceptible to cross-talk and other electro-magnetic interference mechanisms. Photons travel at the speed of light (0.3 mm/ps in free space) while electrons are typically 3 times as slow. More importantly, the velocity of light is independent of the number of interconnects branching from an node. The information velocity of an electronic transmission line is inversely proportional to its capacitance per unit length and as such the information velocity depends on the *electronic load* that must be driven.

1.2 An Optical Fourier Transform Processor

The field of optical computing is not well defined: two distinct branches of the field do exist however. The first branch of optical computers includes those general purpose digital optical computers that exploit certain non-linear optical effects to mimic the operation of logic gates and flip-flops in existing electronic computers. The second branch includes special purpose analog systems or optical signal processors that generally exploit the ability of a lens to perform a 2-D Fourier transform. The focus of this thesis is on the latter of these two branches.

The Fourier-transforming ability of a lens has been known for about a century but the implementation of a practical optical Fourier transformer lacked a device capable of spatially modulating an input optical wavefront in real time. Flat panel display technologies, fuelled primarily by the notebook computer and projection TV industries, have recently made some technological advances, and liquid crystal displays, originally designed for information display, are now being incorporated into optical signal processors.

Three liquid crystal displays from a Kodak video projector were made available for use as spatial light modulators in an optical signal processing experiment. It was proposed to design and build an optical Fourier transform coprocessor that could be incorporated into a PCs architecture and would be dedicated to processing 2-D optical Fourier transforms at video rates (30 frames per second). An optical Fourier transformer with a 256 by 256 spatial light modulator operating at video rates could calculate the equivalent of 64 1024-point FFTs in less than 17 ms. By comparison, the fastest digital signal processors (DSPs), at the time of writing, could process a single 1024 point complex fast Fourier transform (FFT) in less than 0.8 ms (50 ms on a 16 MHz 80386 and 600 ms on the 8088). Spatial light modulators with 1024 by 1024 pixels and sub-microsecond switching times are becoming reality; optical Fourier transformers based on these spatial light modulators would have data throughputs that are orders of magnitude higher than the best dedicated electronic DSP chips.

1.3 Scope of the Thesis

This thesis describes the theory, design, construction, and characterization of an optical Fourier transformer. The branch of physical optics known as Fourier optics is reviewed in chapter two after a brief discussion of some mathematical preliminaries at the end of this introductory chapter. Fourier optics uses a linear systems approach to describe the diffraction of light, and is used to develop the Fourier-transforming property of a lens. A review of the current state-of-the-art liquid-crystal spatial light modulators is presented in chapter three. For optical computing to become a viable alternative (or supplement) to conventional electronic computing, further advances in the speed, resolution and modulation capabilities of spatial light modulators must be made. Chapter four discusses the characterization of the Kodak liquid crystal spatial light modulator and the

construction of the optical Fourier transformer. The Kodak spatial light modulator was designed for projection, not optical processing, and important specifications for the device were not readily available. Therefore the device was reverse engineered and several important specifications were determined through experimentation. Several sinusoidal inputs were processed by the optical Fourier transformer and their spectra are presented in chapter five. A strategy is also identified in chapter five that permits the interpretation of a 2-D optical Fourier transform in terms of the familiar discrete Fourier transform. A summary and some suggestions for further work are outlined in the final chapter.

1.4 Mathematical Preliminaries

This section provides a brief review of some mathematical notation, 1-D and 2-D Fourier transforms, linear system theory, wavefunction nomenclature, and optical intensity, that will be used in this thesis.

1.4.1 Notation for Useful Functions

The gate or rectangle function with unit height and base is defined in the following manner,

$$\Pi(x) = \begin{cases} 0 & |x| > \frac{1}{2} \\ 1 & |x| < \frac{1}{2} \end{cases} \quad \text{and} \quad \Pi(x,y) = \Pi(x)\cdot\Pi(y) \qquad [1\text{-}1]$$

It follows that $h\Pi[(x - c)/b]$ represents a displaced rectangle function of height h and base b centred on $x = c$. The filtering, interpolating, or sinc function,

$$\text{sinc}(x) = \frac{\sin(\pi x)}{\pi x} \qquad \text{and} \qquad \text{sinc}(x,y) = \text{sinc}(x)\cdot\text{sinc}(y) \qquad [1\text{-}2]$$

is defined in the conventional manner such that its value at the origin is unity and the area under its curve is unity. By this choice of notation $\Pi(t)$ and sinc(ν) are a Fourier transform pair where $\nu = \omega/2\pi$. The replicating or sampling function is defined as,

$$\text{Ш}(x) = \sum_{n=-\infty}^{\infty} \delta(x - n) \qquad \text{and} \qquad \text{Ш}(x,y) = \text{Ш}(x)\cdot\text{Ш}(y) \qquad [1\text{-}3]$$

where $\delta(x)$ is the Dirac delta function. The function is its own Fourier transform and provides a sampling operation under multiplication and a replicating operation under convolution. The 2-D properties of the functions in Equations [1-1] through [1-3] are a natural extension of the 1-D properties since all of the functions are easily separable as shown.

1.4.2 The Fourier Transform

The forward 1-D *temporal* Fourier Transform of f(t) is a minus-i transform defined in the conventional manner,

$$F(\omega) = \mathcal{F}_t\{f(t)\} = \int_{-\infty}^{\infty} f(t)\, e^{-i\omega t}\, dt \qquad [1\text{-}4]$$

where t is time and ω is the temporal angular frequency. The inverse transform of F(ω) is a plus-i transform defined in the conventional manner,

$$f(t) = \mathcal{F}_t^{-1}\{F(\omega)\} = \frac{1}{2\pi}\int_{-\infty}^{\infty} F(\omega)\, e^{i\omega t}\, d\omega \qquad [1\text{-}5]$$

The forward 2-D *spatial* Fourier Transform of $f(x,y)$ is defined with a plus-i exponential term,

$$F(k_x, k_y) = \mathcal{F}_{xy}\left\{f(x,y)\right\} = \int_{-\infty}^{\infty}\int_{-\infty}^{\infty} f(x,y)\; e^{i(k_x x + k_y y)}\; dx\; dy \qquad \textbf{[1-6]}$$

where x and y are the spatial variables, and k_x and k_y are the spatial angular frequencies. The inverse transform is defined with a minus-i exponential term,

$$f(x,y) = \mathcal{F}_{xy}^{-1}\left\{F(k_x, k_y)\right\} = \frac{1}{4\pi^2}\int_{-\infty}^{\infty}\int_{-\infty}^{\infty} F(k_x, k_y)\; e^{-i(k_x x + k_y y)}\; dk_x\; dk_y \qquad \textbf{[1-7]}$$

The signs of the exponential arguments in the spatial transform pair are opposite to those of the temporal transform pair so as to be consistent with the engineering convention for a travelling wave. Under the engineering convention, a plane wave travelling in the +z-direction has a minus-i spatial exponential and a plus-i temporal exponential (see Equations [1-10] and [1-12] respectively). The inverse transform of Equation [1-7] is defined so that the synthesis of an arbitrary signal will have consistent signs with the engineering convention.

1.4.3 Shift-Invariant Linear Systems

A system is linear if its response to the sum of any two inputs is equal to the sum of its responses to each of the inputs considered separately (principle of superposition). A linear system is shift-invariant if, when its input is shifted in time or space, its output shifts by an equal amount, but otherwise remains the same.

The output $f_2(x,y)$ of a shift-invariant linear system is related to its input $f_1(x,y)$ by its convolution with the impulse-response function $h(x,y)$ of the linear system,

$$f_2(x,y) = h(x,y) * f_1(x,y) = \int_{-\infty}^{\infty}\int_{-\infty}^{\infty} h(x',y')\, f_1(x-x',y-y')\, dx'\, dy' \qquad [1\text{-}8]$$

In accordance with the convolution theorem of Fourier transforms, Equation [1-8] may also be recast as,

$$F_2(k_x,k_y) = H(k_x,k_y) \cdot F_1(k_x,k_y) \qquad [1\text{-}9]$$

where $F_1(k_x,k_y)$, $F_2(k_x,k_y)$, and $H(k_x,k_y)$ are the Fourier transforms of $f_1(x,y)$, $f_2(x,y)$, and $h(x,y)$ respectively. The multiplicative factor $H(k_x,k_y)$ in Equation [1-9] is the system's transfer function and is the Fourier transform of the impulse response function.

1.4.4 Wavefunction Nomenclature

A monochromatic wave is described by a complex wavefunction,

$$\psi(r,t) = a(r)\, e^{i\phi(r)} e^{i2\pi\nu t}, \quad r = (x,y,z) \qquad [1\text{-}10]$$

that must satisfy the wave equation, where $a(\mathbf{r})$ is amplitude, $\phi(\mathbf{r})$ is phase, and υ is frequency. The complex amplitude,

$$\psi(r) = a(r)\, e^{i\phi(r)} \qquad [1\text{-}11]$$

is the time independent part of the complex wavefunction and must satisfy the Helmholtz equation. The amplitude and phase are given by $|\psi(\mathbf{r})|$ and $\arg\{\psi(\mathbf{r})\}$ respectively, and the intensity is proportional to $|\psi(\mathbf{r})|^2$. The wavefronts are surfaces of constant phase $\phi(\mathbf{r}) = \arg\{\psi(\mathbf{r})\} = 2\pi q$, where q is an integer.

A wavefunction is paraxial if its wavefront normals make a small angle with an optic axis: for example the z-direction. A paraxial wave can be constructed by

modulating a plane wave with a complex envelope $\psi_e(\mathbf{r})$. The complex amplitude of a paraxial wavefunction is then given by,

$$\psi(\boldsymbol{r}) = \psi_e(\boldsymbol{r})\, e^{-ikz} \qquad [1\text{-}12]$$

where the complex envelope must satisfy the paraxial Helmholtz equation. The variation of $\psi_e(\mathbf{r})$ with respect to position must be small over a distance $\lambda = 2\pi/k$ in order for the paraxial wave to maintain its underlying plane wave nature.

When the polarization of a paraxial wavefunction is important the complex envelope becomes a vector with complex components. The complex amplitude and complex envelope are then described by,

$$\boldsymbol{\psi}(\boldsymbol{r}) = \boldsymbol{\psi}_e(\boldsymbol{r})\, e^{-ikz}, \quad \text{and} \quad \boldsymbol{\psi}_e(\boldsymbol{r}) = A_x(\boldsymbol{r})\hat{\boldsymbol{x}} + A_y(\boldsymbol{r})\hat{\boldsymbol{y}} \qquad [1\text{-}13]$$

respectively, where A_x and A_y are the complex components. At a fixed value of z the tip of the vector $\boldsymbol{\psi}(\mathbf{r})\, e^{-i2\pi\nu t}$ traces out an ellipse called a Lissajous figure that completely characterizes the state of polarization. The complex components A_x and A_y are often expressed as their magnitudes and phases in a Jones vector,

$$\boldsymbol{J} = \begin{bmatrix} A_x \\ B_y \end{bmatrix} = \begin{bmatrix} a_x e^{i\delta_x} \\ a_y e^{i\delta_y} \end{bmatrix} = \begin{bmatrix} \cos(\alpha) \\ e^{i\delta}\sin(\alpha) \end{bmatrix} \quad \text{with} \quad \tan(\alpha) = \frac{a_y}{a_x} \qquad [1\text{-}14]$$

where a_x and a_y are the magnitudes, and δ_x and δ_y are the phase advances, in the x- and y-directions respectively. The phase difference $\delta = \delta_y - \delta_x$ and ratio of magnitudes a_y/a_x, fully describe the state of polarization. A polarization device such as a wave plate can be described by a 2x2 Jones matrix $\mathbf{T}$. The output $\mathbf{J}_2$ from a polarization device $\mathbf{T}$ is given by the matrix product of its input Jones vector $\mathbf{J}_1$ and its Jones matrix $\mathbf{T}$,

$$\boldsymbol{J_2} = \boldsymbol{T}\boldsymbol{J_1} \qquad [1\text{-}15]$$

1.4.5 Optical Intensity

The optical intensity of a monochromatic wave is defined as its optical power per unit area and is proportional to the absolute square of its complex amplitude,

$$I = \frac{1}{2} c \epsilon_0 \left| a_E(\mathbf{r})\, e^{j\phi(\mathbf{r})} \right|^2 = \frac{1}{2} c \epsilon_0 \left| a_E(\mathbf{r}) \right|^2 \quad \left[\frac{W}{m^2}\right] \qquad \textbf{[1-16]}$$

where c is the velocity of light, ϵ_0 is the electric permittivity of free space, and $a_E(\mathbf{r})$ represents the amplitude of the electric field.

Chapter 2
Fourier Optics

Fourier optics is a branch of physical optics that uses harmonic analysis to describe the propagation of light through an optical system. It is particularly well suited to those people in electrical engineering and others disciplines who are familiar with signals and linear systems theory.

Fourier analysis permits one to represent an arbitrary function $f(x,y)$, of two spatial variables x and y, as a superposition of harmonic functions of the form $\exp[-i2\pi(\nu_x x + \nu_y y)]$, where ν_x and ν_y are spatial frequencies (cycles per unit length). Recall that a plane wave is given by $\exp[-i(k_x x + k_y y + k_z z)]$ where the coefficients (k_x,k_y,k_z) are components of the wavevector **k**. In an arbitrary plane, $z = 0$ for example, the equation for a plane wave is identical to the 2-D harmonic function if k_x and k_y are interpreted as angular spatial frequencies (radians per unit length). An arbitrary function $f(x,y)$ can therefore be analyzed as a superposition of plane waves. The plane wave is the 2-D spatial building block used to synthesize wavefronts of arbitrary complexity in the same way that the sinusoid is the 1-D building block used to synthesize temporal signals.

This chapter begins with a review of diffraction theory. The Fresnel diffraction equation is used in section 2.2 to derive the Fourier transforming property of a lens. The chapter concludes with a determination of the resolution of an optical system.

2.1 Diffraction Theory

Any deviation from geometric optics that results from wavefront obstruction or the local alteration of wavefront amplitude is a referred to as a diffraction

phenomena. Diffraction effects are a consequence of the wave nature of light and can not be explained by geometric optics. A diffraction pattern is the intensity distribution of an optical wave after it has been transmitted through an aperture in a opaque screen and has travelled some distance in free space. If the optical wave originates from a discrete number of sources, rather than from a continuous distribution of sources, the effect is termed an interference, rather than a diffraction phenomena. Diffraction in an optical system leads to a fundamental limitation in instrument resolution.

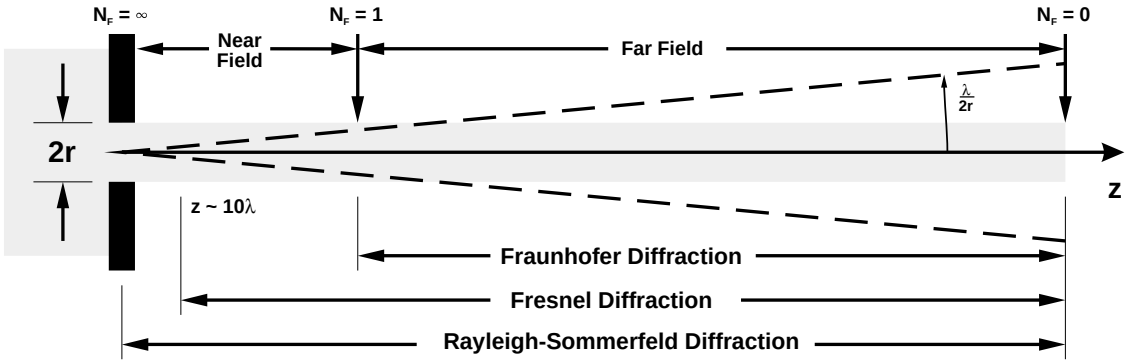


Figure 2-1: Diffraction of light by an aperture in an opaque screen indicating the regions where the Rayleigh-Sommerfeld, Fresnel, and Fraunhofer diffraction theories are valid.

It is desirable to be able to calculate the diffraction pattern generated by an arbitrary aperture. An exact pattern based on a solution of the Helmholtz equation under the boundary conditions imposed by the aperture is mathematically difficult in all but the most trivial cases. Several diffraction theories have been developed using a variety of assumptions leading to results with varying accuracies.

The Rayleigh-Sommerfeld diffraction theory, a mathematical extension of the Huygens-Fresnel principle (to be discussed below), is the most rigorous of the scalar diffraction theories. It treats light as a scalar phenomenon and neglects

the fact that the various components of the electric and magnetic fields are coupled through Maxwell's equations. Two approximations to the Rayleigh-Sommerfeld diffraction formula are possible if: (a) the maximum dimension of the aperture is much smaller than the wavelength of light; and (b) the observation plane is at least several wavelengths from the aperture. The validity of a particular approximation is determined by the value of the Fresnel number,

$$N_F = \frac{(r'_{max})^2}{\lambda z} \qquad [2\text{-}1]$$

where r'_{max} is the maximum radial dimension of the aperture, z is the distance from the aperture to the plane of interest, and λ is the wavelength of light.

When a diffraction pattern is calculated in the *near-field*, the curvature of the wavefronts must be taken into account at the aperture and in the observation plane. The Fresnel diffraction formula can be used in this regime to approximate the propagation of light when,

$$\frac{N_F \theta_{max}^2}{4} \ll 1, \quad \theta_{max} \approx \frac{r_{max}}{z}, \qquad [2\text{-}2]$$

where r_{max} is the largest radial distance in the observation plane, and F_N is the Fresnel number defined in Equation [2-1]. In the *far-field*, the light source and observation screen are effectively far enough from the aperture so the wavefronts arriving at the aperture and observation screen may be considered plane. The Fraunhofer diffraction formula can be used in this regime to approximate the propagation of light when $N_F \ll 1$. Figure 2-1 illustrates the conditions under which the Rayleigh-Sommerfeld, Fresnel, and Fraunhofer diffraction theories are valid.

The Fresnel and Fraunhofer diffraction formulae are developed in sections 2.1.2 and 2.1.3 respectively. They will be applied to propagating wavefronts using a linear systems approach. It is instructive to first consider a heuristic approach to wavefront propagation and diffraction.

2.1.1 The Huygens-Fresnel Principle

The Dutch physicist Christian Huygens suggested a principle, which was later extended by Fresnel, that offers an intuitive approach to the interpretation of diffraction.

> Huygens-Fresnel Principle: Every unobstructed point on an optical wavefront can be considered a source of secondary spherical wavelets of the same frequency, and the field at any point beyond the original wavefront is a superposition of all these wavelets.

The Huygens-Fresnel Principle is applied to a plane wave, spherical wave, and an obstructed spherical wavefront in Figure 2-2. Line segment AB forms the original wavefront and A'B' is the new wavefront a distance *ct* away, where *c* is the speed of light in the medium, and *t* is time. The new wavefront at A'B' is a superposition of all possible wavelets with source on AB.

The third application of the Huygens-Fresnel principle in Figure 2-2 shows a spherical wavefront with source at O incident on an aperture SS'. The propagated wavefront PP' is shown to the left of the aperture as a superposition of wavelets originating from points along SS'. The diffraction phenomena becomes quite apparent here as the geometric light rays appear to bend around the aperture SS' into the shadow region defined by rays OA and OB.

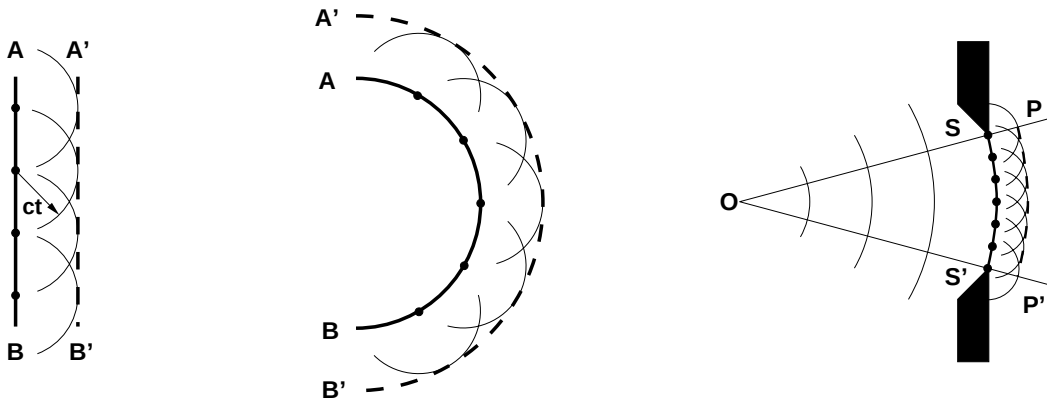


Figure 2-2: Application of the Huygens-Fresnel principle to plane waves, spherical waves, and obstructed spherical waves.

2.1.2 Fresnel Diffraction

The Fresnel diffraction formula is formally derived in this section. Using a linear systems approach it can be used to propagate a field with arbitrary amplitude and phase through an optical system. The derivation presented here closely follows that of Banerjee [7].

The starting point for the derivation of the Fresnel diffraction formula is the complex amplitude of the paraxial wavefunction,

$$\psi(x,y,z) = \psi_e(x,y,z)\, e^{-ik_0 z} \qquad [2\text{-}3]$$

which appeared in the previous chapter as Equation [1-12]. The complex amplitude in Equation [2-3] is interpreted as a plane wave carrier e^{-ikz}, travelling in the $+z$ direction, modulated by a complex envelope $\psi_e(x,y,z)$. Using this interpretation, only the spatial variation of the complex envelope must be tracked as the wavefront propagates, and the plane wave carrier can be ignored for the moment. The complex envelope $\psi_e(x,y,z)$ which must satisfy the paraxial Helmholtz Equation given by,

$$\frac{\partial^2 \psi_e}{\partial x^2} + \frac{\partial^2 \psi_e}{\partial y^2} = i2k_0 \frac{\partial \psi_e}{\partial z} \qquad [2\text{-}4]$$

can be obtained by substituting Equation [2-3] into the Helmholtz equation $(\nabla^2 + k^2)\,\psi(x,y,z) = 0$. A Fourier transform technique is now used to solve Equation [2-4]. Using the derivative theorem of Fourier transforms it is easy to show that the Fourier transform of Equation [2-4] is given by,

$$\frac{d\Psi_e(k_x,k_y;z)}{dz} = \frac{i}{2k_0}\left(k_x^2 + k_y^2\right)\Psi_e(k_x,k_y;z) \qquad [2\text{-}5]$$

where $\Psi_e(k_x,k_y;\, z)$ is the Fourier transform of $\psi_e(x,y,z)$, and $\Psi_{e0}(k_x,k_y)$ is the Fourier transform of $\psi_{e0}(x,y)$. Now solve Equation [2-5] for the Fourier spectrum $\Psi_e(k_x,k_y;z)$.

$$\Psi_e(k_x,k_y;z) = \Psi_{e0}(k_x,k_y)e^{\left[\frac{i(k_x^2 + k_y^2)z}{2k_0}\right]} \qquad [2\text{-}6]$$

The LHS of Equation [2-6] represents the spectrum of an initial wavefront $\psi_{e0}(x,y)$ with spectrum $\Psi_{e0}(k_x,k_y)$ after it has propagated through free space a distance z. It is convenient to interpret Equation [2-6] with the help of linear system theory. Consider a linear system with input spectrum $\Psi_{e0}(k_x,k_y)$ and output spectrum given by Equation [2-6]. The *spatial frequency response* of this linear system is given by,

$$H(k_x,k_y;z) = \frac{\Psi_e(k_x,k_y;z)}{\Psi_{e0}(k_x,k_y)} = e^{\left[\frac{i(k_x^2 + k_y^2)z}{2k_0}\right]} \qquad [2\text{-}7]$$

and the expression $H(k_x,k_y;\, z)$ is called the *spatial transfer function of free space*. It follows that one can multiply an initial spectrum $\Psi_{e0}(k_x,k_y)$ by the transfer function $H(k_x,k_y;z)$ to determine the spectrum of ψ_{e0} after propagation

through a distance *z*. The *spatial impulse-response function of free space* is given by the Fourier transform of Equation [2-7],

$$h(x,y,z) = \mathcal{F}_{xy}^{-1}\left\{H(k_x,k_y;z)\right\} = \frac{ik_0}{2\pi z}\, e^{\left[\frac{-i(x^2+y^2)k_0}{2z}\right]} \qquad \textbf{[2-8]}$$

The Fresnel diffraction formula can now be calculated using linear system theory and the spatial impulse response function derived in Equation [2-8]. An initial arbitrary complex envelope ψ_{e0} is propagated through a distance z by convolving it with the spatial impulse-response of free space h(*x,y,z*),

$$\psi_e(x,y,z) = \psi_{e0}(x,y) * h(x,y,z) \qquad \textbf{[2-9]}$$

When the convolution operation is expanded we get the *Fresnel diffraction formula*,

$$\psi_e(x,y,z) = \frac{ik_0}{2\pi z}\int_{-\infty}^{\infty}\int_{-\infty}^{\infty} \psi_{e0}(x',y')\, e^{\left[\frac{-ik_0}{2z}\left[(x-x')^2+(y-y')^2\right]\right]}\, dx'\, dy' \qquad \textbf{[2-10]}$$

The Fresnel diffraction formula is valid when Equation [2-2] is satisfied, or in general terms, when *z* is greater than about ten wavelengths. A far-field approximation to the Fresnel diffraction formula is developed in the next section.

2.1.3 Fraunhofer Diffraction

The Fraunhofer diffraction formula is a far-field approximation to the Fresnel diffraction formula. It is derived by expanding the Fresnel diffraction formula convolution integral and observing that some terms in the integral approach unity as z approaches infinity. When the convolution integral in Equation [2-10] is expanded, the Fresnel diffraction formula becomes,

$$\frac{ik_0}{2\pi z}\, e^{\left[\frac{-ik_0}{2z}(x^2+y^2)\right]} \int_{-\infty}^{\infty}\int_{-\infty}^{\infty} \psi_{e0}(x',y')\, e^{\left[\frac{-ik_0}{2z}(x'^2+y'^2)\right]}\, e^{\left[\frac{ik_0}{z}(xx'+yy')\right]}\, dx'\, dy' \qquad [2\text{-}11]$$

In the far-field z is large compared to both x' and y'. As z approaches infinity, the argument of the first exponent in the integral approaches zero. More specifically, when N_F is much less than unity,

$$N_F = \frac{(r'_{max})^2}{\lambda z} = \frac{k_0\left(x'^2+y'^2\right)_{max}}{2\pi z} \ll 1 \qquad [2\text{-}12]$$

the value of the first exponent in the integral of Equation [2-11] is unity over the *x'y'*-plane. Under this condition, known as the *Fraunhofer approximation*, the first exponent in the integral of Equation [2-11] disappears, and we are left with the *Fraunhofer diffraction formula*,

$$\psi_e(x,y,z) = \frac{ik_0}{2\pi z}\, e^{\left[\frac{-ik_0}{2z}(x^2+y^2)\right]} \int_{-\infty}^{\infty}\int_{-\infty}^{\infty} \psi_{e0}(x',y')\, e^{\left[\frac{ik_0}{z}(xx'+yy')\right]}\, dx'\, dy' \qquad [2\text{-}13]$$

Note that the integral in Equation [2-13] represents the 2-D Fourier transform of the initial profile $\psi_{e0}(x',y')$. Rewriting the Fraunhofer diffraction formula in terms of a 2-D Fourier transform,

$$\psi_e(x,y,z) = \frac{ik_0}{2\pi z}\, e^{\left[\frac{-ik_0}{2z}(x^2+y^2)\right]}\, \mathcal{F}_{xy}\left\{\psi_{e0}(x,y)\right\}\Big|_{\substack{k_x = k_0 x / z \\ k_y = k_0 y / z}} \qquad [2\text{-}14]$$

The Fraunhofer diffraction formula is valid in the far-field when the Fresnel number F_N is less than unity. For example, consider the far-field diffraction pattern of a helium-neon (λ = 632nm) laser beam with a 1mm waist-radius. The Fraunhofer diffraction formula is valid for *z* greater than 2m by Equation [2-1].

2.2 Optical Fourier Transforming

The Fraunhofer diffraction formula demonstrated that the far-field diffraction pattern of a wavefront is proportional to its spatial Fourier transform. Using Fraunhofer diffraction to perform image processing in the Fourier domain has two major disadvantages: (a) The Fourier transform is available in the far-field which is not very space efficient; and (b) The quadratic phase term introduced by the Fraunhofer diffraction formula may cause phase distortions.

In this section the Fresnel diffraction formula is used to develop an efficient optical Fourier-transformer. It was shown in the previous section that the far-field diffraction pattern of a wavefront is proportional its Fourier transform. It will be shown that a simple lens (a) brings the Fourier transform from the far-field into the near-field; and (b) cancels out the quadratic phase term pre-multiplying the Fourier transform. The optical element required to bring the Fourier transform from the far-field into the near-field is determined in the following section.

2.2.1 Phase Transformation Introduced by a Lens

The optical element required to bring the far-field into the near-field, or more specifically, transform a plane wave into a spherical wave, is determined in this section. The optical field at an arbitrary distance z behind a plane wave illuminated phase object (or optical element) is calculated using the Fresnel diffraction formula and the conditions under which the field converges to a focus are determined. Consider the glass phase object shown in Figure 2-3 with unit amplitude plane waves incident from the left.

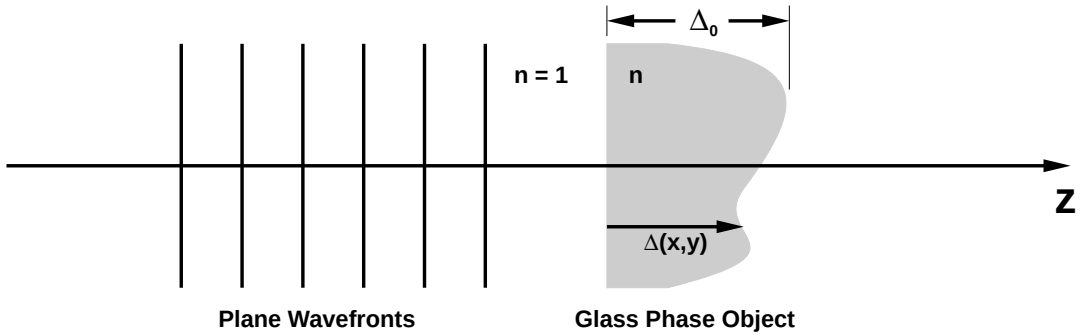


Figure 2-3: Plane waves incident on a glass phase object of varying thickness $\Delta(x,y)$, maximum thickness Δ_0, and refractive index n.

The glass phase object has thickness in the z-direction given by $\Delta(x,y)$ and maximum thickness Δ_0. The phase delay of a unit amplitude plane wave incident from the left is given by,

$$\phi(x,y) = nk_0\Delta(x,y) + k_0\left[\Delta_0 - \Delta(x,y)\right] \qquad \textbf{[2-15]}$$

where n is the refractive index of the glass. The first term in the RHS of Equation [2-15] represents the phase change due to propagation in glass and the second term is the contribution due to propagation in air. The complex amplitude of the field immediately to the right of the phase object is,

$$\psi(x,y)\Big|_{\substack{right\ of\\ glass}} = e^{-i\phi(x,y)} = e^{\left[-i\left(nk_0\Delta(x,y) + k_0\left(\Delta_0 - \Delta(x,y)\right)\right)\right]} \qquad \textbf{[2-16]}$$

The Fresnel diffraction formula is used to propagate the complex envelope of Equation [2-16] from the glass phase object into an arbitrary plane a distance z from the phase object. The complex envelope $\psi_{e0}(x,y) = e^{ik\Delta}\psi(x,y)$ is convolved with the spatial impulse response $h(x,y;z)$ and after simplification we get,

$$\psi_e(x,y,z) = \psi_{e0}(x,y) * h(x,y;z) = \frac{ik_0}{2\pi z} e^{\left[\frac{-ik_0}{2z}(x^2+y^2)\right]} \times \mathrm{I} \qquad \textbf{[2-17]}$$

where I is an integral given by,

$$I = \int_{-\infty}^{\infty}\int_{-\infty}^{\infty} e^{\left[-ik_0(n-1)\Delta(x',y')\right]}\, e^{\left[\frac{-ik_0}{2z}(x'^2+y'^2)\right]}\, e^{\left[\frac{ik_0}{z}(xx'+yy')\right]}\, dx'\, dy' \qquad \textbf{[2-18]}$$

The first exponential term in the integral of Equation [2-18] is due to the phase object, the second term represents a quadratic phase curvature, and the third term is the basis of the Fourier transforming property we are trying to exploit. An optical Fourier transformer would require us to save the third exponential term and eliminate the first two. The thickness function $\Delta(x',y')$ in the argument of the first term can be tailored such that the first and second terms cancel each other out. It can be shown that choosing a phase object with thickness function,

$$\Delta(x',y') = a + \frac{b}{2}\left(x'^2 + y'^2\right) \qquad \textbf{[2-19]}$$

will cause the product of the first and second exponential terms in the integral of Equation [2-18] to equal unity when,

$$z = \frac{-(1/b)}{n-1} = f \qquad \textbf{[2-20]}$$

Equations [2-19] and [2-20] are substituted into Equation [2-17] to get an expression for the complex envelope in the focal plane of the phase object,

$$\psi_e(x,y)\Big|_{\substack{focal\\plane}} = \frac{ik_0}{2\pi f}\, e^{\left[\frac{-ik_0}{2f}(x^2+y^2)\right]} \int_{-\infty}^{\infty}\int_{-\infty}^{\infty} e^{\left[\frac{ik_0}{f}(xx'+yy')\right]}\, dx'\, dy' \qquad \textbf{[2-21]}$$

Note that Equation [2-21] contains the 2-D spatial Fourier transform of the unit amplitude plane wave incident on the glass phase object when,

$$k_x = \frac{k_0 x}{f} \quad \text{and} \quad k_y = \frac{k_0 y}{f} \qquad [2\text{-}22]$$

It can be shown using analytical geometry that Equations [2-19] and [2-20] represent the paraxial approximation to a plano-convex lens with radius $R = 1/b$ and thickness $a = \Delta_0$ (Banerjee [7], pages 125-127). Two plano-convex lenses with radii R_1 and R_2 (where $R_1 > 0$ and $R_2 < 0$) may be placed back-to-back to create a convex lens with effective focal length given by,

$$\frac{1}{f} = (n - 1)\left(\frac{1}{R_1} - \frac{1}{R_2}\right) \qquad [2\text{-}23]$$

the *lens makers equation*. The phase transformation introduced by a convex lens can then be calculated by substituting Equations [2-20] and [2-23] into Equation [2-16],

$$\Phi(x, y; f) = e^{\left[\frac{ik_0}{2f}(x^2 + y^2)\right]} \qquad [2\text{-}24]$$

The optical field on the LHS of a lens with focal length f can now be calculated as the product of the phase transformation given by Equation [2-24] and the field incident on the lens.

It has been shown that a simple lens is the required phase object to bring the Fourier transform of an initial profile from the far-field into the focal plane of the lens. The next section investigates the effect of placing a transparency $t(x,y)$ directly in front of a lens illuminated by plane waves.

2.2.2 Transparency $t(x,y)$ Placed Immediately in Front of a Lens

Consider a transparency to be some kind of spatial light modulator (SLM) that is able to alter the amplitude and preserve the phase of *pixels* in an optical field

propagating through the plane of the transparency; a transparency modulates an incident wavefront in the same way that an acetate sheet modulates the light in an overhead projector. The transparency $t(x,y)$ shown in Figure 2-4 is placed immediately in front of a biconvex lens with infinite aperture and illuminated by plane waves of unit amplitude.

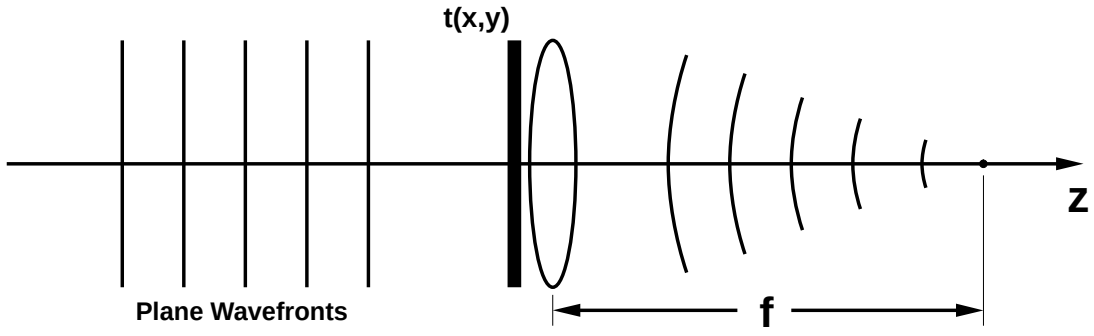


Figure 2-4: A transparency $t(x,y)$ placed immediately in front of a lens with focal length f and illuminated with plane waves.

The complex envelope immediately behind the lens is given by the product of the transparency function $t(x,y)$ and the phase transformation introduced by the lens of focal length f,

$$\psi_e(x,y)\Big|_{\substack{back\\of\ lens}} = t(x,y)\cdot\Phi(x,y;f) = t(x,y)\cdot e^{\left[\frac{ik_0}{2f}\left(x^2+y^2\right)\right]} \qquad \textbf{[2-25]}$$

The Fresnel diffraction formula is now applied to determine the field in the back focal plane of the lens by convolving Equation [2-25] with the spatial impulse response of free space $h(x,y;f)$,

$$\psi_e(x,y)\Big|_{\substack{focal\\plane}} = \frac{ik_0}{2\pi f}\, e^{\left[\frac{-ik_0}{2f}(x^2+y^2)\right]} \int_{-\infty}^{\infty}\int_{-\infty}^{\infty} t(x',y')\, e^{\left[\frac{ik_0}{f}(xx'+yy')\right]}\, dx'\, dy' \qquad \textbf{[2-26]}$$

The quadratic phase term that appeared in the integral of Equation [2-18] has been cancelled by the introduction of the biconvex lens as required. Recasting Equation [2-26] in terms of the Fourier transform of the transparency function $t(x,y)$ we get,

$$\psi_e(x,y)\Big|_{\substack{focal\\plane}} = \frac{ik_0}{2\pi f}\, e^{\left[\frac{-ik_0}{2f}(x^2+y^2)\right]} \mathcal{F}_{xy}\left\{t(x,y)\right\}\Big|_{\substack{k_x=k_0x/f\\k_y=k_0y/f}} \qquad \textbf{[2-27]}$$

and note that the Fourier transform of $t(x,y)$ is recoverable but is pre-multiplied by a quadratic phase term.

2.2.3 Transparency $t(x,y)$ Placed a Distance d_o in Front of a Lens

Consider the plane wave illumination of a transparency $t(x,y)$ placed a distance d_o in front of a lens with infinite aperture as shown in Figure 2-5.

The complex envelope at the transparency is first propagated a distance d_o to the front of the lens using the Fresnel diffraction formula. The transfer function approach to wave propagation is appropriate here and the Fourier spectrum of the transparency function $T(k_x,k_y)$ is multiplied by the spatial transfer function of free space,

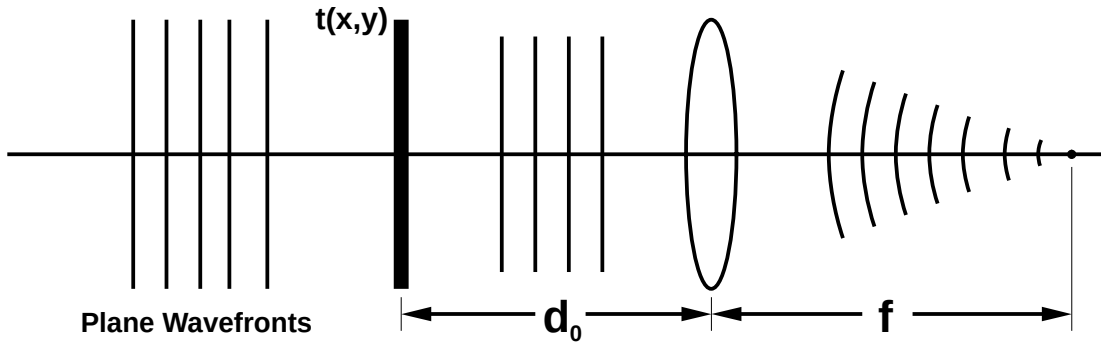


Figure 2-5: A transparency $t(x,y)$ placed a distance d_o in front of a lens with focal length f and illuminated with plane waves.

$$\Psi_e(k_x,k_y)\Big|_{\substack{front\\of\ lens}} = T(k_x,k_y)\cdot H(k_x,k_y;d_o) = T(k_x,k_y)\,e^{\left[\frac{i(k_x^2+k_y^2)d_o}{2k_0}\right]} \qquad \textbf{[2-28]}$$

Equation [2-27] from the previous section is used to propagate the spectrum from the front of the lens into the back focal plane of the lens. The Fourier operators cancel when the Fourier transform of Equation [2-28] is substituted for $t(x,y)$ in Equation [2-27], and after simplification the field becomes,

$$\psi_e(x,y)\Big|_{\substack{focal\\plane}} = \frac{ik_0}{2\pi f}\,e^{\left[\frac{-ik_0}{2f}\left(1-\frac{d_o}{f}\right)(x^2+y^2)\right]}\;T(k_x,k_y)\Big|_{\substack{k_x=k_0x\,/\,f\\k_y=k_0y\,/\,f}} \qquad \textbf{[2-29]}$$

Note that a quadratic phase term again pre-multiplies the Fourier transform of $t(x,y)$ in Equation [2-29] but vanishes when f equals d_o. When a transparency $t(x,y)$ is placed in the front focal plane of a lens, the quadratic phase curvatures disappear, and the exact Fourier transform of the transparency is recoverable in the back focal plane,

$$\psi_e(x,y)\Big|_{\substack{focal\\plane}} = \frac{ik_0}{2\pi f}\,\mathcal{F}_{xy}\left\{t(x,y)\right\}\Big|_{\substack{k_x=k_0x\,/\,f\\k_y=k_0y\,/\,f}} \qquad \textbf{[2-30]}$$

2.3 Resolution of an Optical System

The resolution of an optical system is determined by the f-number of its lens defined as the ratio of its focal length to its aperture. The resolution and spatial bandwidth of a single-lens optical system is derived below.

The resolution of any linear system is determined by its impulse response function. The impulse response of a single-lens optical system is the Fourier transform of the aperture at the lens. Consider a lens with focal length f and aperture D. A circular aperture of diameter D can be represented in a cylindrical coordinate system as $\Pi(r/D)$. The Fourier-Bessel transform of a circular aperture is given by,

$$\mathcal{F}_r\left\{ \Pi\left(\frac{r}{D}\right) \right\} = \frac{\pi D}{k_r} J_1\left(\frac{k_r D}{2}\right) \qquad \textbf{[2-31]}$$

where $J_1(\cdot)$ is a first-order Bessel function and k_r is the angular spatial frequency. Now scale the spatial frequency k_r-axis as a spatial r-axis by substituting $k_r = k_0 r/f$ into the Fourier-Bessel transform given by equation,

$$\mathcal{F}_r\left\{ \Pi\left(\frac{r}{D}\right) \right\}\Bigg|_{k_r=\frac{k_0 r}{f}} = \pi\left(\frac{D}{2}\right)^2 \frac{2J_1(\pi\gamma)}{\pi\gamma}, \quad \text{with} \quad \gamma = \frac{k_0 r D}{2\pi f} \qquad \textbf{[2-32]}$$

and define the new variable γ as shown. Rayleigh's criterion for just-resolvable images, a somewhat arbitrary but useful criterion, requires that the centres of two impulse response functions can be no closer than the radius defined by their first minima. In other words, the argument of the Bessel function of Equation [2-32] must be equal to its first minimum at the limit of resolution,

$$\gamma = \frac{3.832}{\pi} = \frac{k_0 r D}{2\pi f} = \frac{rD}{\lambda f} \qquad [2\text{-}33]$$

This equation is often recast as the Abbe condition, or the minimum separation between two impulse response functions,

$$r_{min} = 1.22\,\lambda_0\left(\frac{f}{D}\right) \qquad [2\text{-}34]$$

where *f/D* is the *f*-number of the lens. The spatial bandwidth is then given by $(r_{min})^{-1}$ cycles per unit length.

Chapter 3
Liquid Crystal Spatial Light Modulators

The spatial light modulator (SLM) is a relatively new optical device. It is fundamental to the fields of optical signal processing, optical computing, and flat panel display systems. A spatial light modulator is any device that is able to alter the intensity of pixels in an optical field propagating through it. A simple example of an SLM is a transparency on an overhead projector - the pixels in the beam's cross section have different intensities after passing through the transparency and the beam is spatially modulated. It is generally agreed that the lack of fast, high-resolution SLMs is the major obstacle that has prevented many optical computing systems from achieving reality, Feitelson [25].

Spatial light modulators come in many flavours: photographic film, liquid crystal light valves (LCLVs), deformable mirror devices (DMDs), and electro- and magneto-optic devices. Liquid Crystal (LC) spatial light modulators have received a lot of attention recently due to technological advances prompted by the demand for flat panel televisions and notebook computers. High resolution LC-SLMs with contrast ratios suitable for optical computing are now available off-the-shelf.

The remainder of this chapter is a brief review of LC-SLM technology. The chapter reviews liquid crystal phases, liquid crystal field-effects, the electro-optics of several devices, and active matrix addressing.

3.1 Liquid Crystals

Several organic materials exhibit an intermediate phase between the solid and liquid states. This transitional phase is called a *mesophase* and is characterized

by a molecular structure that lies between that of the solid and liquid states. The liquid-crystal state is a mesophase in which constituent molecules have orientational order (like crystals) but lack positional order (like liquids). The molecules of a liquid crystal are cigar-shaped and consequently their properties are highly anisotropic.

Traditionally, liquid crystal mesophases are grouped into three classes: nematic, smectic, and cholesteric. These classes are illustrated in Figure 3-1. The molecules of the **nematic** liquid crystal shown in Figure 3-1(a) tend to be parallel but their positions are random. The molecules of the **smectic** liquid crystal shown in Figure 3-1(b) are also parallel but their centres are stacked in parallel layers within which they have random positions. When the constituent molecules of a nematic liquid crystal are *chiral*[1] they undergo helical rotation about an axis, as shown in Figure 3-1(c), and the phase is called **chiral nematic** or **cholesteric**.

[1]Liquid crystal molecules are chiral or *asymmetric* if they have no plane of symmetry. A chiral molecule has two possible mirror image structures each of which are optically active: The *dextrorotatory* (right) structure rotates the plane of linearly-polarized light clockwise and the *levorotatory* (left) structure rotates plane-polarized light counter-clockwise.

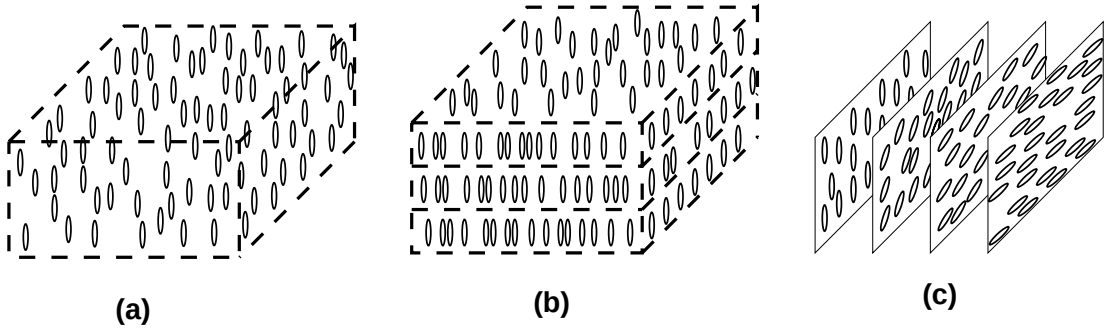


Figure 3-1: Schematic representation of the (a) nematic, (b) smectic, and (c) cholesteric liquid crystal mesophases.

The transitions, with increasing temperature, from the solid state, through the liquid crystal mesophases, to the liquid state follows the order shown,

$$\textbf{solid} \rightarrow \text{semectic B} \rightarrow \text{semectic C} \rightarrow \text{semectic A} \rightarrow \text{nematic} \rightarrow \textbf{liquid} \qquad [3\text{-}1]$$

where A, B, and C represent different classes of the smectic phase. The properties of the nematic and smectic phases are expanded upon below.

3.1.1 Nematic Phase

The nematic phase is characterized by orientational order and random translational order as shown in Figure 3-1(a). This ordering causes the molecules to align parallel to one another but still remain fluid. The preferred molecular orientation or principle axis in space is called the *director* and is denoted by the vector **n**. The nematic phase is symmetric about ±**n** providing uniaxial optical properties.

The cholesteric (chiral nematic) phase is a distorted form of the nematic phase where the constituent molecules of the phase are chiral and exhibit *optical*

activity[2]. The cholesteric phase is characterized by a director **n** that follows a helix with an axis perpendicular to **n** as shown in Figure 3-1(c). The order is periodic with a spatial period derived from the pitch of the helix. If the pitch of the helix is much larger than optical wavelengths, the direction of linearly polarized light incident on the liquid crystal is rotated by the helix as it propagates through the medium.

3.1.2 Smectic Phase

The smectic phase is characterized by one degree of translational ordering resulting in a layered structure as shown in Figure 1-3(b). Molecules within each layer are aligned with a vector **n** called the *director* and have random translational ordering. Several smectic phases have been identified, most notably the smectic A and C phases, which demonstrate uniaxial and biaxial optical properties, respectively. Smectic phases with chiral molecules are indicated by appending an asterisk (*) to the phase identifier. Most notable is the ferroelectric smectic-C* phase.

3.2 Switching in a Liquid Crystal

It is instructive to examine how liquid crystal molecules are re-oriented by an external electric field before considering liquid crystal devices. This section reviews the dielectric and ferroelectric effects.

[2]An optically active substance rotates the plane of polarization of a beam of light as the beam passes through the substance.

3.2.1 The Dielectric Effect

An external electric field can achieve molecular reorientation in a nematic liquid crystal using the dielectric effect. The effect is typically very slow. The molecules of a liquid crystal seek to minimize the thermodynamic potential of the fluid. The potential is proportional to the *dielectric anisotropy*[3] $\Delta\epsilon$ and the square of the inner-product of the director **n** and external electric field **E**,

$$\text{Thermodynamic Potential} \propto -\Delta\epsilon\,(\boldsymbol{n}\cdot\boldsymbol{E})^2 \qquad [3\text{-}2]$$

The thermodynamic potential is minimized when **n** is either parallel or perpendicular to **E** depending on the sign of $\Delta\epsilon$. When an electric field **E** is applied across a nematic liquid crystal of *positive dielectric anisotropy*, the director **n** tries to align parallel with the electric field **E**; if the material displays *negative dielectric anisotropy* the director **n** tries to align perpendicular to the electric field **E**. Note that parallel alignment can mean either $\mathbf{n}\parallel\mathbf{E}$ or $\mathbf{n}\parallel\text{-}\mathbf{E}$ (similarly for the perpendicular alignment $\mathbf{n}\perp\mathbf{E}$ or $\mathbf{n}\perp\text{-}\mathbf{E}$) so the direction of the electric field has no effect on the direction of the molecular director.

When a voltage is applied across a nematic liquid crystal, reorientation is observed to begin when the electric field exceeds a certain threshold. The threshold is defined by the voltage,

$$V_{TH}^2 = \frac{1}{\Delta\epsilon\epsilon_0}\left[K_{11}\pi^2 + (K_{33} - 2K_{22})\Theta^2\right] \qquad [3\text{-}3]$$

at which the electric torques exceed the elastic molecular forces and distortion of the original orientation begins, where K_{11}, K_{22}, and K_{33} are elastic constants of

---

[3]The dielectric anisotropy $\Delta\epsilon$ of a liquid crystal is the difference between the dielectric constant parallel and perpendicular to the optic axis, $\Delta\epsilon = \epsilon_{\parallel} - \epsilon_{\perp}$. The optic axis (OA) in a nematic liquid crystal is parallel to the local director **n**.

the liquid crystal, and Θ is the twist angle. Upon removal of the applied voltage the molecular alignment returns to its original equilibrium orientation established by the elastic forces. This re-alignment to the original orientation is much slower than the reorientation caused by the electric field. The analogue nature of the dielectric effect lends itself well to devices that require gray-scale capability.

The rise and decay times, defined to be those times for a 10% to 90% contrast ratio change at normal incidence, are given by,

$$t_{rise} \propto \frac{\eta(T)\,d^2}{\epsilon V^2} \quad \text{and} \quad t_{decay} \propto \frac{\eta(T)\,d^2}{K} \qquad \text{[3-4]}$$

where $\eta(T)$ is the temperature-dependent liquid crystal viscosity, and K is an elastic parameter. Only the rise time is a function voltage--elastic forces are required to restore the liquid crystal cell to its equilibrium state and consequently the decay time greatly exceeds the rise time.

3.2.2 The Ferroelectric Effect

The ferroelectric effect is used to achieve molecular reorientation in ferroelectric liquid crystals such as the smectic-C* phase. The effect is very fast and two bistable orientations of the director **n** are possible, one for each polarity of the applied electric field.

A ferroelectric liquid crystal (FLC) will reorient its *spontaneous polarization*[4] $\mathbf{P_s}$ in response to an electric field and consequently its optic axis can be toggled

[4]Spontaneous polarization refers to the establishment of permanent dipole moment domains under the application of an electric field. It is the electric analogue to the magnetic process where the domains of a ferromagnetic material grow under a magnetic field until the material becomes permanently magnetized.

between two bistable orientations. A spontaneous polarization $\mathbf{P}_s$ in a uniform electric field **E** will experience a torque,

$$\boldsymbol{N} = \boldsymbol{P}_s \times \boldsymbol{E}, \qquad [3\text{-}5]$$

where the direction of the torque is such that it tries to align $\mathbf{P}_s$ with **E** and point them in the same direction. This effect is substantially faster than the dielectric effect; sub-microsecond switching times have been observed with ferroelectric smectic C* liquid crystals. The effect is inherently bistable and has no analog or gray-scale properties.

3.3 Liquid Crystal Devices

This section reviews the electro-optic characteristics of some of the more important spatial light modulators: field-induced birefringence, twisted nematic, ferroelectric, and electroclinic devices.

Two distinct surface alignments are possible in a liquid crystal cell. When the molecular director **n** is parallel to the cell's surface the cell has *homogeneous alignment*; when the molecular director **n** is perpendicular to the cell's surface the cell has *homeotropic alignment*. These alignments can be induced by treating the cell surfaces: A homogeneous alignment is induced if the surface is *rubbed* or polished in a particular direction with certain chemicals and homeotropic alignment is induced by chemical treatment or additives to the liquid crystal.

3.3.1 Field-Induced Birefringence Devices

A liquid crystal cell is constructed by sandwiching a nematic liquid crystal with negative dielectric anisotropy between two parallel glass plates as illustrated in

Figure 3-2. An electric field can be established in the cell by applying a voltage across two transparent electrodes on the inside surface of each glass plate. The electrodes on each plate are rubbed such that the liquid crystal prefers a homeotropic alignment - its director is parallel to the direction of incident light. The liquid crystal cell is then placed between a pair of crossed polarizers.

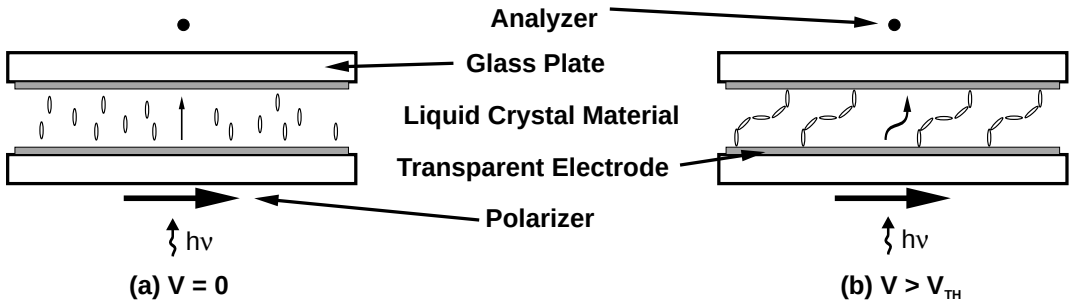


Figure 3-2: Schematic illustration of the induced birefringence effect (a) with no applied voltage; and (b) with an applied voltage $V > V_{TH}$.

The off-state (no applied voltage) is illustrated in Figure 3-2(a). The nematic liquid crystal appears isotropic to light incident normal to the cell. An incident beam polarized at the entrance is extinguished by the crossed polarizer at the back of the cell. When a voltage $V > V_{TH}$ is applied to the cell, the molecules in the centre of the cell begin to distort, and the liquid crystal appears birefringent to the incident light. As the voltage is increased, the cell switches to its on-state, and a fraction of the light is passed through the crossed polarizes, as shown in Figure 3-2(b). The optical transmission of the cell is given by,

$$T = \sin^2 2\phi \, \sin^2 \frac{\delta}{2}, \qquad \delta = \frac{2\pi}{\lambda} d\,\Delta n(V), \qquad \text{[3-6]}$$

where ϕ is the angle between the transmit axis (TA) of the entrance polarizer and the projection of the director on the glass plate, d is the cell thickness, and

$\Delta n(V)$ is the voltage-induced change in *birefringence*[5]. Transmission is maximized by forcing $\phi = 45°$ in Equation [3-6]. This is realized by rubbing the conductive coatings on the cell such that the preferred molecular deformation angle is 45° to the crossed polarizes.

3.3.2 Twisted Nematic (TN) Devices

A liquid crystal cell is constructed by sandwiching a chiral nematic liquid crystal with positive dielectric anisotropy between two parallel glass plates as illustrated in Figure 3-3. An electric field is established in the cell by applying a voltage across two transparent electrodes on the inside surface of each glass plate. The electrodes on each plate are rubbed such that the liquid crystal prefers a homogeneous alignment; its directors are perpendicular to the incident light. In addition, the electrodes are treated such that the director next to the lower electrode prefers to lie in the plane of the figure, and the director next to the upper electrode prefers to lie in the plane perpendicular to the figure. Consequently, the directors of the liquid crystal must undergo a gradual twist of 90° between the lower and the upper glass plates. The liquid crystal cell is placed between a pair of parallel polarizes.

The off-state (no applied voltage) is illustrated in Figure 3-3(a). A light beam incident on the cell is plane polarized by the entrance polarizer and its plane of polarization is rotated by 90° as it passes through the chiral liquid crystal. The beam is extinguished at the analyzer because its plane of polarization is now perpendicular to the transmission axis (TA) of the analyzer. When a voltage $V > V_{TH}$ is applied to the cell, the chiral nematic helix starts to untwist as the

[5]Optical birefringence Δn is the difference between the refractive index parallel and perpendicular to the optic axis, $\Delta n = n_{\parallel} - n_{\perp}$.

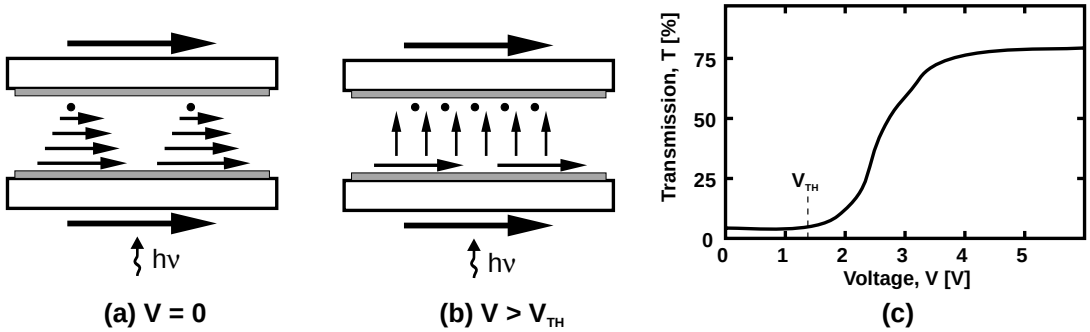


Figure 3-3: Schematic illustration of the twisted nematic effect in a cell equipped with parallel polarizers for (a) zero applied voltage, (b) applied voltage $V > V_{TH}$, and (c) its transfer function.

directors attempt to align with the electric field. When the voltage is much greater than the threshold, the helix breaks down completely, and the cell switches to its fully-on state as shown in Figure 3-3(b). As the helix collapses, the intensity transmitted increases, because the liquid crystal cell no longer actively rotates the plane polarized light between the parallel polarizes. The optical transmission of the cell is given by,

$$T = \frac{1}{1+u^2}\sin^2\left(\frac{\pi}{2}\sqrt{1+u^2}\right), \qquad u = \frac{2d}{\lambda}\Delta n(V) \qquad \text{[3-7]}$$

where d is the cell thickness, and $\Delta n(V)$ is the voltage-induced change in birefringence. Optical transmission as a function voltage for a typical TN-SLM with parallel polarizers is shown in Figure 3-3(c). Transmission may be achieved with zero voltage, and extinction with a voltage greater than threshold, by using crossed rather than parallel polarizes. In this way either black-on-white or white-on-black displays can be realized, depending on the orientation of the polarizer-analyzer pair.

A TN-SLM is an intensity modulating device, and consequently, the amplitude of an optical wavefront can not be modulated independently of its phase. Numerical modelling of TN modulation has shown that while intensity is

modulated from one extreme to the other, the phase is modulated by at least $\pi/3$ radians, Day [22]. Phase modulation, independent of amplitude modulation, can be achieved using a parallel nematic SLM (a TN-SLM with zero twist). The phase of an optical wavefront has been modulated by 2π radians in this way most recently by Amako [3], [4], and by others, most notably Barns et al. [9], and Konforti [47].

Twisted nematic devices are based on the dielectric effect and consequently switching is generally very slow. Most devices are designed for television applications and switch at television frame rates. Rise and fall times are in the 10 ms to 50 ms range.

3.3.3 Smectic-C* Ferroelectric Devices

A surface stabilized ferroelectric liquid crystal (SSFLC) device is constructed by sandwiching a smectic-C* liquid crystal between two parallel glass plates. The technique known as surface stabilization is used to promote the formation of two bistable director orientations of opposite ferroelectric polarization. The electrodes on each plate are rubbed such that the liquid crystal prefers a homogeneous alignment. When the cell thickness is less than the pitch of the chiral material the boundary conditions imposed by surface stabilization promote an unwinding of the chiral helix. In the absence of the helix there are only two stable and equal energy configurations available to the molecular director. The bistable states, referred to as *up* and *down*, have opposite ferroelectric polarizations and are illustrated in Figure 3-4 pointing in the $\pm x$-directions. When the device is toggled by an external electric field, the director $\mathbf{n}$ swings through an angle of $2\theta_t$ and the spontaneous polarization $\mathbf{P}_s$ switches direction. Assume that the device illustrated in Figure 3-4 is sandwiched between a crossed analyzer-polarizer pair, where the down-state director $\mathbf{n}$ is parallel to

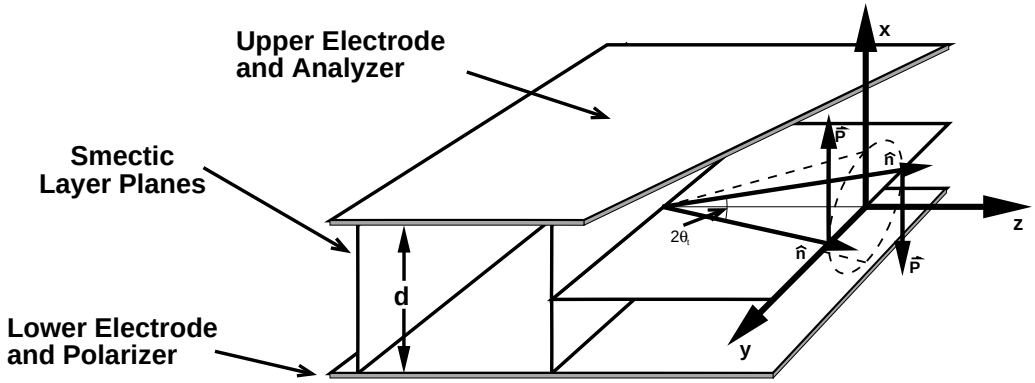


Figure 3-4: Schematic representation of surface stabilized ferroelectric liquid crystal (SSFLC) bistability. The two possible ferroelectric polarizations point in the ±*x* directions.

the transmission axis (TA) of the polarizer. First consider what happens when the cell is in its down-state. An incident beam of light is plane polarized by the entrance polarizer, its plane of polarization is not altered by the cell, and the beam is extinguished by the crossed analyzer. When the cell is toggled into its up-state by an external electric field, the director **n** swings through an angle $2\theta_t$ in the plane of the cell. An incident beam of light, plane polarized by the entrance polarizer, is now effectively rotated by the cell and a fraction of its intensity is allowed to pass through the analyzer. The optical transmission of a surface stabilized FLC-SLM is given by,

$$T = \sin^2(4\theta_t)\sin^2\left(\frac{\pi \Delta n d}{\lambda}\right) \qquad \text{[3-8]}$$

where Δn is the liquid crystal birefringence, d is the cell thickness, and θ_t is the cone angle of the smectic-C* liquid crystal. The best contrast ratio is achieved when $\theta_t = 22.5°$. Sub-microsecond switching of SSFLC devices with a contrast in excess of 2000:1 have been demonstrated. Such a device is bistable and has no gray-scale response.

3.3.4 Smectic A* Devices

Spatial light modulators, based on the new smectic-A* liquid crystal, use the electroclinic effect to induce an effective director tilting in the non-tilted liquid crystal. Induced director rotation, upon the application of an electric field, depends on both the polarity and strength of the field. It exhibits a linear coupling of applied electric field to molecular tilt, and consequently the effect shows analog or gray-scale response without bistability. A device based on the electroclinic effect is similar in construction to the SSFLC device, and is generally assembled as a variably rotatable wave plate sandwiched between crossed polarizes. The effect shows analog or gray-scale response without bistability and sub-microsecond switching times. The amplitude and phase of an optical wavefront can be modulated independently, Day [22].

3.4 Active Matrix Addressing

The spatial modulation of an optical wavefront requires the ability to selectively excite multiple positions in the plane of the device, while leaving other positions unaffected. This process of distributing a 2-D signal through the device, and exciting the required pixels, is known as addressing. Active matrix addressing grew out of a need for high-resolution, high-speed, and high-contrast display devices suitable for television signals.

An active matrix architecture is constructed by inserting a non-linear active device, such as a transistor, at each liquid crystal element or pixel. An active matrix consists of an array of field effect transistors (FETs) with row and column address lines. The rows are connected to the gates of the transistors, the columns to the sources, and the pixel pads to the drains. The FETs are

fabricated on either a transparent substrate using thin-film transistors (TFTs) or a single-crystal silicon substrate using standard VLSI techniques.

3.4.1 Thin-Film Transistors (TFTs) on a Transparent Substrate

Thin-film transistors (TFTs), integrated on a transparent substrate of fused quartz or glass, are generally used in notebook computers and other display devices that require modulation of a transmitted light source. Traditionally TFTs have been fabricated in amorphous silicon (a-Si). The advantages of polycrystalline silicon (poly-Si) and cadmium selenide (CdSe) TFTs have long been realized however devices using amorphous silicon TFTs are more economical to construct, Brody [14]. The alternatives offer increased speed and performance, and more importantly, the ability to fabricate integrated line and column driving electronics on the same substrate.

3.4.2 VLSI on Single Crystal Silicon Substrate

Standard VLSI techniques can be used to fabricate MOS transistors and aluminum mirrors on a single-crystal silicon backplane, for video projection systems, or spatial light modulators which modulate a reflected light source. The VLSI technology offers a high resolution MOS process and consequently smaller devices, higher quality transistors, and a predictable yield over those fabricated as TFTs, McKnight [55].

An active SLM can be classified as either *static* or *dynamic*, analogous to SRAM and DRAM devices. A dynamic backplane uses an array of FETs to isolate a desired charge across each pixel, using the liquid crystal material as the dielectric of a storage capacitor. A static backplane uses an array of latches to establish a constant voltage across each pixel that doesn't need to be

dynamically refreshed. The latter configuration is expected to provide more stable drive conditions for the liquid crystal material, and consequently better optical performance, but at the expense of increased complexity.

Chapter 4
The Optical Processor

The description of free-space light propagation with Fourier optics and the so called Fourier transforming property of a lens has been known for about a century. The lack of fast, high-resolution spatial light modulators however, has prevented these principles from being used in practical optical signal processing applications until recently.

When portable liquid crystal televisions (LCTVs) first became available in the early 1980s, researchers in optical signal processing removed the liquid crystal displays (LCDs) from the TVs and used them as spatial light modulators in their experiments. Several papers were published during this time describing processors designed for optical correlation [36], [37], [45], holographic optical interconnects [8], [64], computer generated holograms [60], and other applications [71], [78], [82]. The author did not find any papers describing a coherent optical Fourier processor dedicated for the calculation of Fourier transform amplitude and phase.

Liquid crystal spatial light modulators are commonly found in video projectors and notebook computer displays. Three such displays from a Kodak LC500 video projector were made available for use as spatial light modulators in an optical signal processing project. The purpose of this chapter is to describe how an SLM from the video projector was incorporated into a computer controlled optical signal processing demonstration system, capable of performing optical Fourier transforms at video rates.

This chapter is divided into three sections. The first section describes the procedure used in characterizing the video projector's SLM. The optics and

electro-optics used to construct the optical Fourier processor are described in the second section and the final section describes the computer control system and software.

4.1 Spatial Light Modulator Characterization

The consumer grade spatial light modulator found in the Kodak LC500 video projector was designed for intensity modulation of a broadband incoherent light source. Several key specifications required for its use as an amplitude and phase modulation device were not readily available (and probably not important or documented by the manufacturer) and consequently had to be measured through experiment. A photograph of the twisted nematic SLM found in the Kodak LC500 is shown in Figure 4-1. The scale along the bottom of the photograph is in centimeters.

The pixel pitch and width, electro-optic voltage-transmission curve, temporal response, and liquid crystal twist and director angles were measured through experiment and are described in the following sections.

4.1.1 Pixel Pitch and Width

The pixel pitch and width, of the video projector's spatial light modulator, were determined by illuminating the modulator with plane waves from a Helium-Neon laser and observing the resulting far field diffraction pattern. The SLM generated a Fraunhofer diffraction pattern consisting of a sinc-modulated array of delta functions. Fourier theory suggested that pixel pitch was inversely proportional to the delta function spacing in the diffraction pattern and pixel width was inversely proportional to the width of the sinc modulating function. The values determined for pixel pitch and width are summarized in Table 4-1.

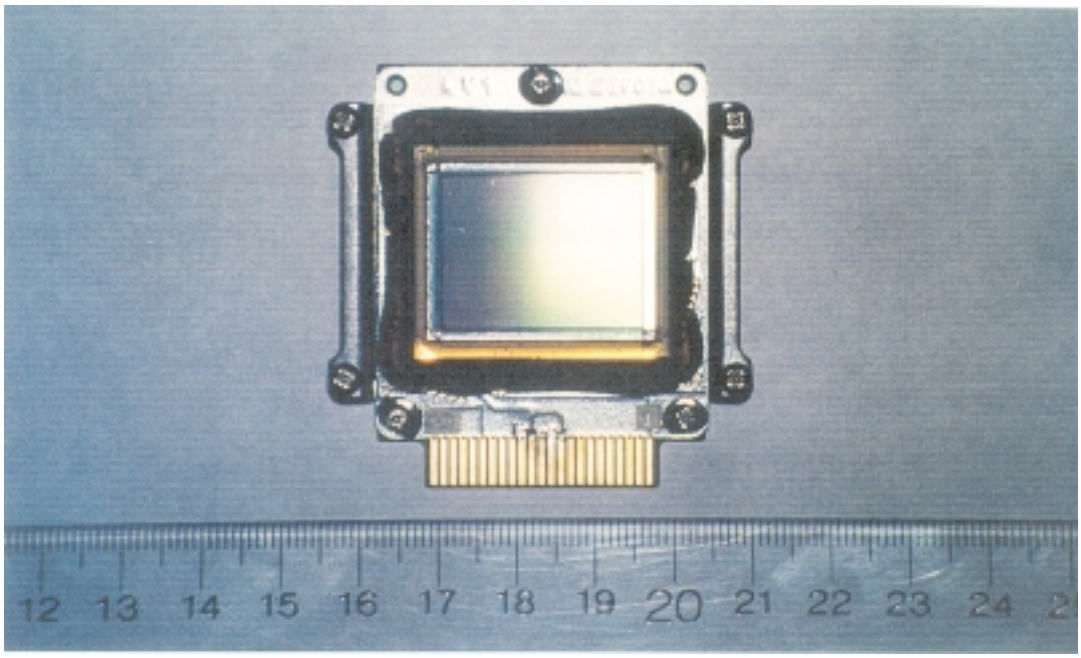


Figure 4-1: Photograph of the twisted-nematic liquid crystal spatial light modulator removed from the Kodak LC500 video projector. The scale along the bottom is in centimeters.

Table 4-1:
Kodak LC500 spatial light modulator pixel pitch and width determined from the Fraunhofer diffraction pattern.

	***x*-direction**	***y*-direction**
Pixel Pitch, Δ	80 μm	90 μm
Pixel Width, δ	56 μm	60 μm

Video images projected by the LC500 suggested that the SLM pixels were rectangular with pitch (Δx_{SLM}, Δy_{SLM}) and width (δx_{SLM}, δy_{SLM}). Fourier theory was used to determine the SLMs far-field diffraction pattern; the Fraunhofer diffraction pattern had an intensity distribution proportional to,

$$|F(x)|^2 \propto \text{Ш}\left(\frac{k_x \Delta x_{SLM}}{2\pi}, \frac{k_y \Delta y_{SLM}}{2\pi}\right) \text{sinc}^2\left(\frac{k_x \delta x_{SLM}}{2\pi}, \frac{k_y \delta y_{SLM}}{2\pi}\right) \qquad [4\text{-}1]$$

where Δx_{SLM} and Δy_{SLM} represent the pixel pitch in the *x*- and *y*-directions respectively and δx_{SLM} and δy_{SLM} represent the pixel widths. Recall from chapter

two that the Fraunhofer diffraction pattern is only valid in the far field; if a Helium-Neon laser of wavelength λ = 632.8 nm and waist radius r'_{max} = 1 mm is used to illuminate the SLM, the Fraunhofer diffraction pattern is only valid at a distance much greater than 2 m (by Equation [2-12] solved for z). The diffraction pattern was observed in a plane 9.6 m from the SLM.

The pixel pitch was determined from the spacing of the delta functions in the diffraction pattern. The delta functions, or interference-maxima, are observed when the arguments of the first term in Equation [4-1] go to zero. The conditions for interference-maxima are given by,

$$m_x\lambda = \Delta x_{SLM}\frac{x}{z} \quad \text{and} \quad m_y\lambda = \Delta y_{SLM}\frac{y}{z}, \qquad \textbf{[4-2]}$$

where x and y represent the coordinate system in the plane of the diffraction pattern, z is the distance from the SLM to the diffraction pattern, and m_x, m_y = 0, ±1, ±2, ±3, ... are integers. The pixel pitch in the x- and y-directions can be calculated by measuring the distance between any two interference-maxima and applying Equation [4-2].

The pixel width was determined from the bandwidth of the sinc-modulating function. The modulating function, or diffraction-envelope, has a minima when the arguments of the second term in Equation [4-1] are non-zero multiples of π. The conditions for diffraction-envelope minima are given by,

$$n_x\lambda = \delta x_{SLM}\frac{x}{z} \quad \text{and} \quad n_y\lambda = \delta y_{SLM}\frac{y}{z}, \qquad \textbf{[4-3]}$$

where n_x, n_y = ±1, ±2, ±3, ... are integers. When an interference maxima and a diffraction minima occur at the same time, an interference maxima will be

missing from the diffraction pattern. The condition for missing orders is obtained by dividing Equation [4-2] by Equation [4-3],

$$\delta x_{SLM} = \frac{n_x}{m_x} \Delta x_{SLM} \quad \text{and} \quad \delta y_{SLM} = \frac{n_y}{m_y} \Delta y_{SLM} \qquad \text{[4-4]}$$

The pixel width in the *x*- and *y*-directions were calculated by determining the ratio of integers *n* and *m* for missing orders.

4.1.2 Voltage-Transmission

The spatial light modulator's electro-optic voltage-transmission curve was determined by measuring its optical transmission as a function of applied voltage. The SLM was illuminated by a Helium-Neon laser and the optical power transmitted through the SLM was recorded as the rms voltage across the SLM was swept from 0 to 5 volts.

The spatial light modulator was placed between parallel polarizers and was rotated to provide minimum optical transmission. With a voltage of 120 mV rms applied across the SLM, the polarizer and analyzer were then iteratively rotated with respect to the SLM until an absolute minimum optical transmission was established. The voltage across the SLM was swept from 0 to 5 volts rms, and the optical power transmitted through it was recorded on an x-y plotter. The electro-optic transfer function is illustrated in Figure 4-2.

The electro-optic transfer function exhibits the same shape as the example illustrated in Figure 3-3(c). The scale in Figure 4-2 is 0.5 V rms per division along the *x*-axis and 7.8 µW per division along the *y*-axis. As the voltage was swept from 0 to 5 V rms, the optical power transmitted by the SLM increased from 51 nW to 45 µW which represents a contrast ratio of better than 800 to 1.

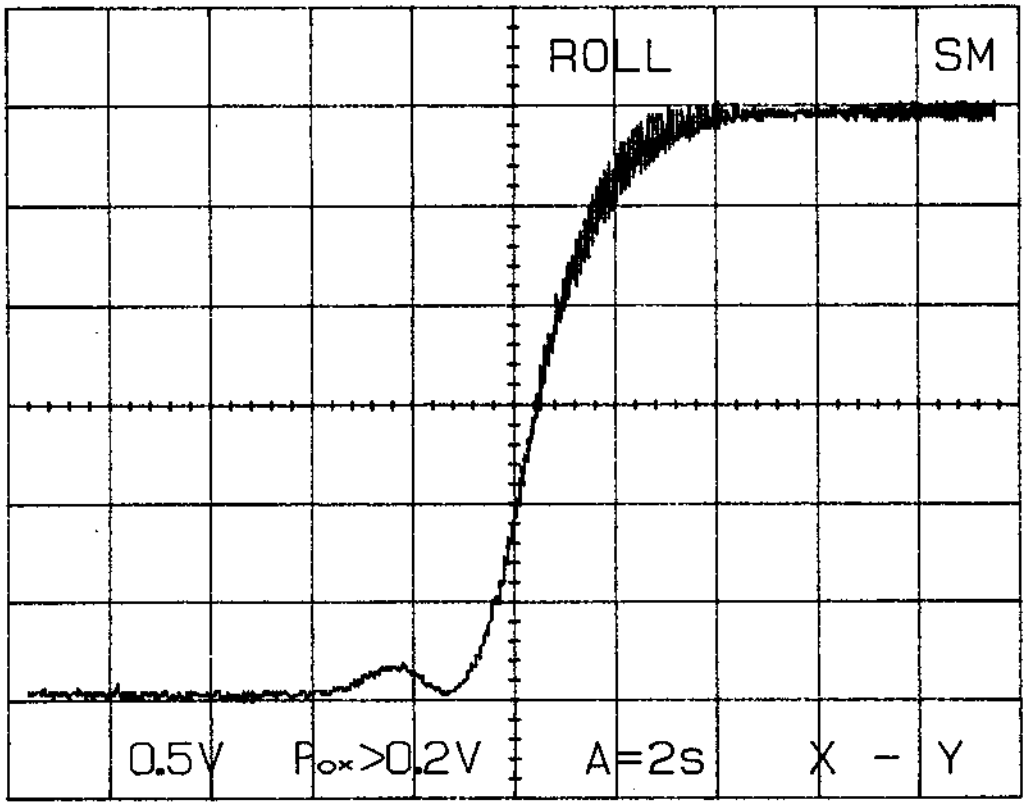


Figure 4-2: Voltage-transmission curve for the Kodak LC500 SLM with parallel polarizers and optimized for minimum transmission at V = 120 mV. The voltage across the SLM is swept from 0 to 5 V rms.

The optical threshold V_{TH} = 2.2 V rms is at the base of the linear region. The small hump just before the optical threshold is characteristic of TN-LCDs and is due to phase modulation prior to the onset of amplitude modulation immediately after the optical threshold (Konforti, [49]).

The apparent variation in power transmitted for V > 2.5 V rms, indicated in the figure by a thicker curve in the upper left-hand portion, is due to the temporal response of the spatial light modulator. The power transmitted in the off-state, defined by V_{OFF} = 1.68 V rms, was measured to be 175 ± 1.4 nW. The power transmitted in the on-state, defined by V_{ON} = 3.52 V rms, was measured to be

41.6 ± 2.5 µW. Choosing these on- and off-states provided a contrast ratio of 230 to 1.

4.1.3 Response Time

The temporal response of the spatial light modulator was measured by toggling between its on- and off-states and recording the subsequent variation in transmitted power. The response time was determined under two SLM driving conditions: (a) the SLM was driven directly by a function generator; and (b) the SLM was driven by a CGA (color graphics adaptor) video card using the video electronics in the LC500 video projector.

When the spatial light modulator was driven directly by the function generator, it was toggled between an off-state of V_{OFF} = 1.0 V rms and an on-state of V_{ON} = 4.0 V rms. When the SLM was driven by the CGA display card and the LC500 video electronics, it was toggled between V_{OFF} = 1.68 V rms and V_{ON} = 3.52 V rms. The video circuitry of the LC500 did not allow very much flexibility in the selection of operating points. The operating points used to drive the SLM directly with the function generator were chosen because they minimized the response time.

The rotation of the analyzer and polarizer with respect to the SLM was chosen to minimize the optical transmission in the off-state. The rise and decay times are defined to be the times required for a 10% to 90% or 90% to 10% change in optical power transmitted. The rise time observed when the SLM was driven directly by the function generator is illustrated in Figure 4-3(a) and the rise time observed when the SLM was driven with the CGA card and LC500 is illustrated in Figure 4-3(b).

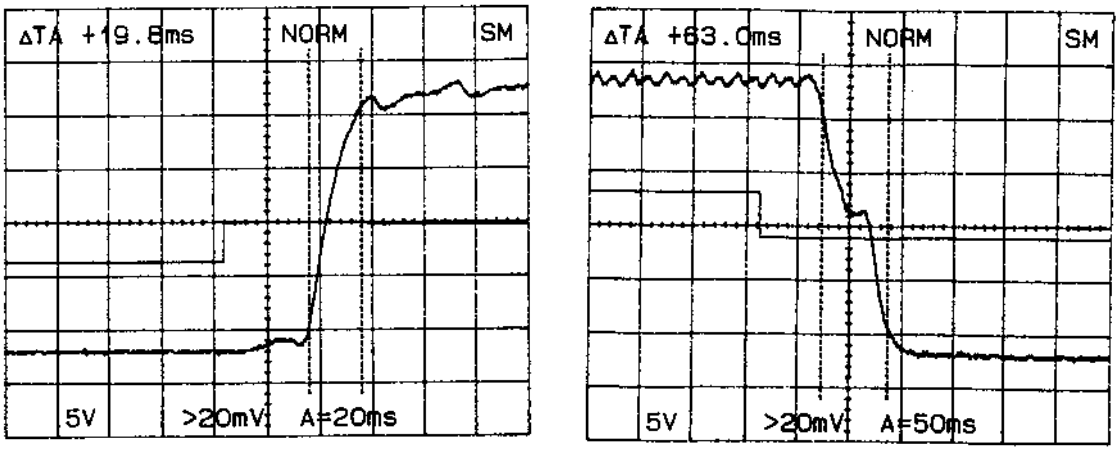


Figure 4-3: Spatial light modulator rise time for 10% to 90% intensity change. (a) SLM driven directly with a function generator, (b) SLM driven with a CGA display card and LC500 video electronics.

The scale in Figure 4-3(a) is 20 ms per division (50 ms per divison for part (b)) along the *x*-axis and normalized intensity along the *y*-axis. The rise time observed when the SLM was driven by the function generator directly is less that a quarter of the rise time observed when the SLM was driven by the CGA card and projector video electronics; the function generator driven rise time indicated between the dashed lines of Figure 4-3(a) is 19.8 ms and the CGA driven rise time indicated in Figure 4-3(b) is 82.5 ms.

The decay times observed when the SLM was driven directly with a function generator and with the CGA display card and LC500 combination are illustrated in Figures 4-4(a) and 4-4(b) respectively. The decay time observed when the SLM was driven by the function generator directly is one third of the decay time observed when it was driven with the CGA card and LC500 combination. The dashed lines in Figure 4-4(a) indicate a decay time of 18.6 ms for the function generator driven SLM and Figure 4-4(b) shows a decay time of 63.0 ms for the CGA and LC500 driven SLM.

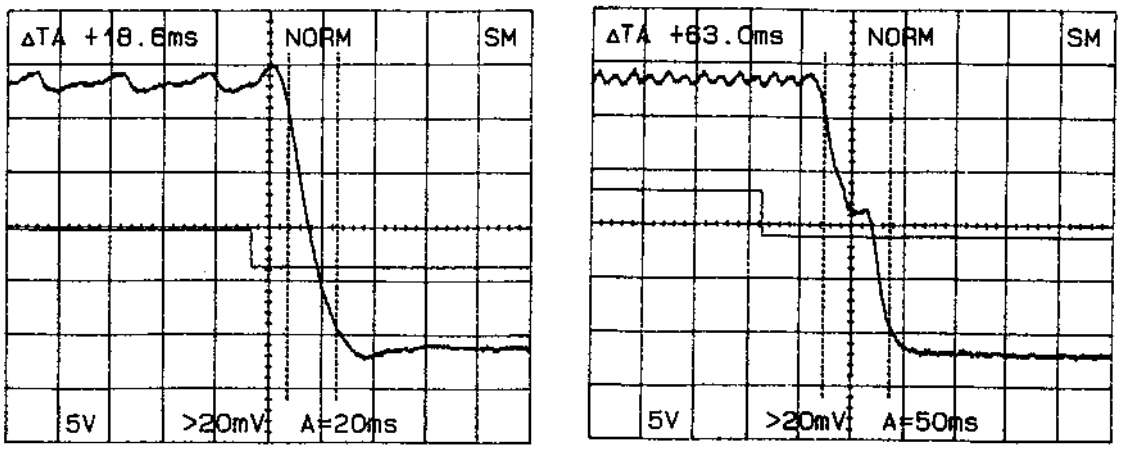


Figure 4-4: Spatial light modulator decay time for 90% to 10% intensity change. (a) SLM driven directly with a function generator, (b) SLM driven with a CGA display card and LC500 video electronics.

Three factors have been identified that contribute to the different response times observed under the two driving conditions. First, the video electronics in the LC500 projector do not facilitate the selection of optimum on- and off-states that would minimize the response times. Secondly, the video buffer RAM on the CGA display card is painfully slow. Thirdly, the interlaced architecture of the CGA video card is such that adjacent lines on its display are not updated in order and consequently there is a substantial delay between the update of adjacent lines, due mainly to the slow RAM.

4.1.4 Twist Angle

The spatial light modulator's twist angle and liquid crystal director orientations were measured using an optical method. The procedure is described only briefly here; a full discussion of the optical method and corresponding theory can be found in Lien, [51] and [52].

The optical method required several iterations. The spatial light modulator was illuminated with a Helium-Neon laser and the optical transmission through the SLM was measured with an optical power meter. The entrance polarizer and exit analyzer were rotated until a minimum optical transmission was observed. The angle between the entrance polarizer and exit analyzer, shown as ϕ_{POL} in Figure 4-5, was measured and recorded.

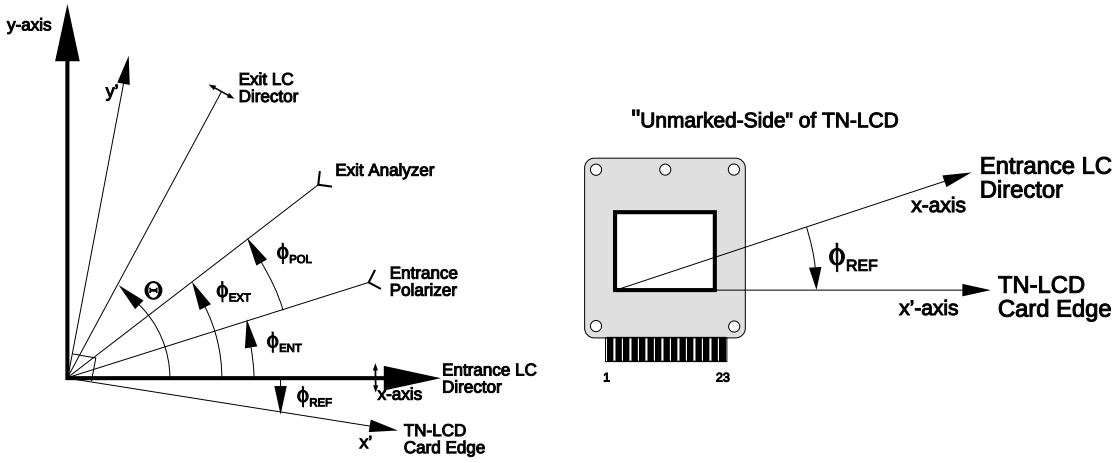


Figure 4-5: Definition of the coordinate system and various angles in the measurement of the SLM twist angle. The Helium-Neon laser light is incident along the *z*-axis and directed out of the page.

The angle between the entrance polarizer and the liquid crystal (LC) director was measured under minimum transmission; The angle ϕ_0 is defined to be the angle between the entrance polarizer and the LC director when the polarizer is oriented for minimum transmission; under minimum transmission ϕ_{ENT} is equal to ϕ_0 and is indicated in Figure 4-5. Because the orientation of the LC director is completely unknown during the first iteration, only a *best-guess* for ϕ_0 denoted by ϕ_0' is possible. The final measurement of a given iteration is the determination of the phase difference δ behind the SLM under the condition $\phi_{ENT} = -\phi_{EXT} = 45°$. The phase difference δ represents the phase advance or delay between orthogonal components of the transmitted optical wavefront and

partially describes the state of its polarization (the polarization of an optical wavefront is completely described by the relative amplitude and phase difference between orthogonal components; see the Jones vector representation given by Equation 1-14). The values of ϕ_{POL} and δ are used to solve two equations simultaneously in order to obtain values for the twist angle Θ and the dimensionless parameter u. The first equation,

$$\frac{1}{x}\sin(x\Theta)\sin(\Theta - \phi_{POL}) + \cos(x\Theta)\cos(\Theta - \phi_{POL}) = 0 \qquad [4\text{-}5]$$

is derived from the minimum transmission condition where x is given by,

$$x = \sqrt{1 + u^2}, \quad \text{with} \quad u = \frac{\pi d}{\lambda\Theta}\Delta n, \qquad [4\text{-}6]$$

d is the thickness of the liquid crystal cell, Δn is the birefringence of the liquid crystal, and λ is the wavelength of the Helium-Neon laser source. The second equation is an expression for the phase between orthogonal components of the optical wavefront transmitted through the liquid crystal cell,

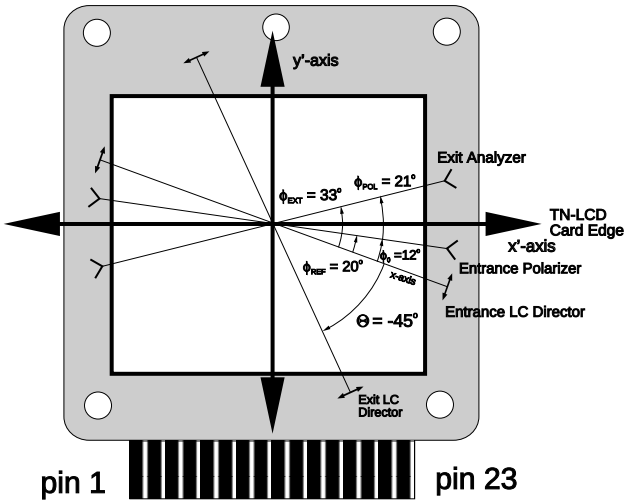
$$\frac{\frac{u}{x}\sin(2x\Theta)}{\cos(2\Theta)\cos(2x\Theta) + \frac{1}{x}\sin(2\Theta)\sin(2x\Theta)} = \tan(\delta) \qquad [4\text{-}7]$$

The simultaneous solution to Equations [4-5] and [4-7] yields values for twist angle Θ and dimensionless parameter u. The twist angle Θ can be used to refine the estimate for ϕ_0. Several iterations were required to get a consistent set of values for Θ, ϕ_0, and dimensionless parameter u. The results are tabulated in Table 4-2.

A schematic diagram of the liquid crystal spatial light modulator is illustrated in Figure 4-6. The figure indicates polarizer-analyzer orientation with respect to the card edge for minimum transmission, the entrance and exit liquid crystal directors, and the twist angle.

Table 4-2:
Measurements and the solution to TN-LCD twist angle equations.

Measurements		**Solution to Equations [4-5] and [4-7]**	
Polarizer Angle for Min. Trans.	ϕ_{POL} = 21°	**Twist Angle**	Θ = - 45°
Entrance Angle for Min. Trans.	$\phi_0 = \phi_{ENT}$ = 12°	**Dimensionless Parameter**	u = - 2.6686
Phase Difference	$\delta = \delta_y - \delta_x$ = 110°	**Cell Thickness**	$d\Delta n$ = 0.422 µm



Notes:

1. **Measurements are for the green TN-LCD.**
2. **The "un-marked" side of TN-LCD is shown.**
3. **Light is incident on the "marked-side" of the display.**

Figure 4-6: Kodak LC500 TN-LCD twist angle characterization. The figure shows polarizer-analyzer orientation for minimum transmission and entrance-exit LC director orientation.

4.1.5 Summary of Specifications

A summary of the experimental measurements made on the Kodak LC500 liquid crystal SLM are presented in Table 4-3.

The values indicated in the table for the on- and off-state voltages and the minimum transmission polarizer angle were the values used in the optical Fourier processor.

Table 4-3:
Summary of the Kodak LC500 liquid crystal SLM specifications determined during its characterization.

Pixel Pitch, Δ	Δx_{SLM} = 80 µm	Δy_{SLM} = 90 µm
Pixel Width, δ	δx_{SLM} = 56 µm	δy_{SLM} = 60 µm
ON- and OFF-Voltages	V_{OFF} = 1.68 v rms	V_{ON} = 3.52 v rms
LC Threshold Voltage	V_{TH} = 2.20 v rms	
Temporal Response	t_{rise} = 82.5 ms	t_{decay} = 63.0 ms
TN-LCD Twist Angle	Θ = - 45°	
Minimum Transmission Polarizer Angle	ϕ_{POL} = 21°	

4.2 The Optical Fourier Transform Processor

The electro-optic components and construction of the optical Fourier processor are discussed in this section while its associated driving electronics, computer control system, and software are discussed in the following section. A schematic diagram of the optical Fourier transformer is illustrated in Figure 4-7.

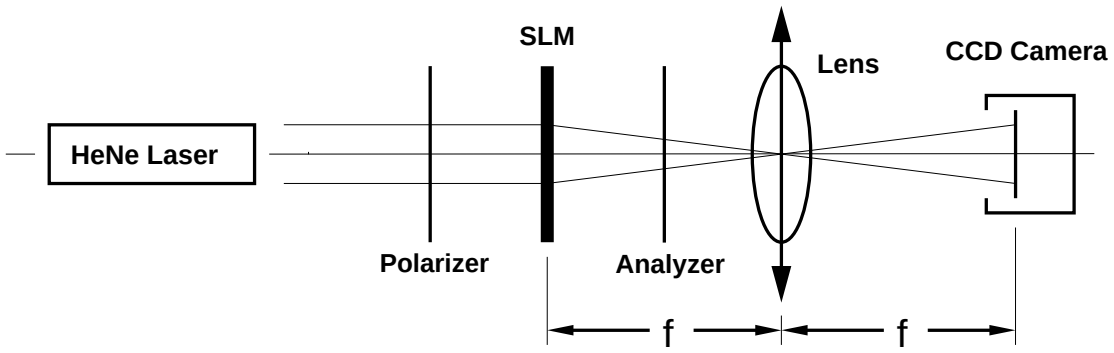


Figure 4-7: Schematic diagram of the optical Fourier transformer. A spatial domain input signal in the plane of the SLM is Fourier transformed into the output or frequency domain plane at the CCD array.

As shown in the figure, a spatial domain input signal written to the spatial light modulator is Fourier transformed by the lens into the frequency domain located in the plane of the CCD array. The SLM is in the front focal plane of the lens and the CCD array is in the back focal plane. The SLM is sandwiched between a polarizer and an analyzer which are oriented for minimum optical transmission when the SLM is in its off-state. The intensity of plane waves from the Helium-Neon laser are spatially modulated by the SLM. The plane waves, which now carry the information written to the SLM, are Fourier transformed by the lens, and the power spectrum of the input signal is recorded by the CCD camera at the back focal plane of the lens.

The electro-optic components are now discussed in greater detail in the order described by signal propagation from left to right in Figure 4-7.

4.2.1 Helium-Neon Laser

A stabilized 1 mW Helium-Neon (HeNe) laser operating at 632.8 nm was used in the optical Fourier processor. The laser was operated in a frequency-stabilized mode that provided a single longitudinal mode with a nominal

frequency of 473.61254 THz. The laser confined its radiation to the lowest order transverse mode (TEM_{00}) which provided a Gaussian beam profile. The beam was plane polarized and its diameter at the waist was 0.514mm.

4.2.2 Spatial Light Modulator

The spatial light modulators found in the Kodak LC500 video projector are active matrix liquid crystal displays (AMLCDs). The active area had dimensions 25.4mm (H) by 19.7mm (V) providing an aspect ratio of 4:3.1. Each SLM had a resolution of 320 (H) by 220 (V) for a total of 70,400 pixels. Each pixel resided in a unit cell of dimensions 80µm (H) by 90µm (V) with a 47 percent fill factor and was individually addressable. Specifications that were not readily available for the SLM were determined during its characterization and were summarized in the previous section.

The Helium-Neon laser illuminated a circular region of the SLM roughly equivalent to the laser's beam diameter. The illuminated region of the SLM had a diameter of roughly six pixels.

4.2.3 Fourier Lens

The lens used in the optical processor (Newport PAC076) was a symmetric lens specifically designed for Fourier transform applications and was composed of three cemented lens. The lens combination was diffraction limited at 632 nm and its design was optimized from 1:1 imaging. It was an f/ 3.3 lens with an effective focal length of 125 mm and a back focal length of 117.5 mm.

4.2.4 CCD Camera

A high resolution 1/2" interline transfer CCD (charge coupled device) camera was used in the optical processor. The Pulnix TM-7AS is an asynchronous video camera with an RS-170 output and is equipped with a 768 (H) by 494 (V) Sony CCD array. The more important specifications are summarized in Table 4-4.

Table 4-4:
Summary of the Pulnix TM-7AS CCD camera specifications.

Resolution	768 pixels (H)	494 pixels (V)
Pixel Pitch	Δx_{CCD} = 8.4 µm	Δy_{CCD} = 9.8 µm
Active Area	6.451 mm (H)	4.841 mm (V)
Pixel Clock	14.28571 MHz	
S/N Ratio (Electrical)	50 dB (minimum, AGC off)	
Saturation Equivalent Exposure (Frame Mode)	SEE = 60 nJ•cm^{-2}	

The camera was used in its frame mode and integration time was set such that the CCD just saturated for a given optical input signal. The automatic gain control (AGC) was turned off and the gain was manually adjusted for each exposure to keep the CCD array from saturating. The gamma was set to unity.

The camera was used without its standard C-mount lens and its CCD array was placed in the back focal plane of the Fourier lens. The camera was assembled in the factory with an protective optical window between the C-mount and the CCD array. This window was removed to reduce reflections and phase distortions.

The intensity of the laser beam was attenuated by a factor of about 1000 by rotating the laser beam's plane of polarization to ensure orthogonality with the transmission axis of the polarizer shown in Figure 4-7. The beam's intensity was attenuated to prevent the CCD array from saturating when all pixels in the SLM were in their on-state. This condition represented the maximum optical transmission through the SLM and required that the camera be operated with its minimum integration time of 1/10,000 second. When only a single SLM pixel is on and all others are off, the integration time could be increased up to a maximum of 1/60 second in order to increase the dynamic range.

4.3 Computer Control System and Software

The input signal written to the spatial light modulator and the output signal received from the CCD array were controlled by a 80386 computer and appropriate software. A block diagram of the optical Fourier transformer and computer control system is illustrated in Figure 4-8.

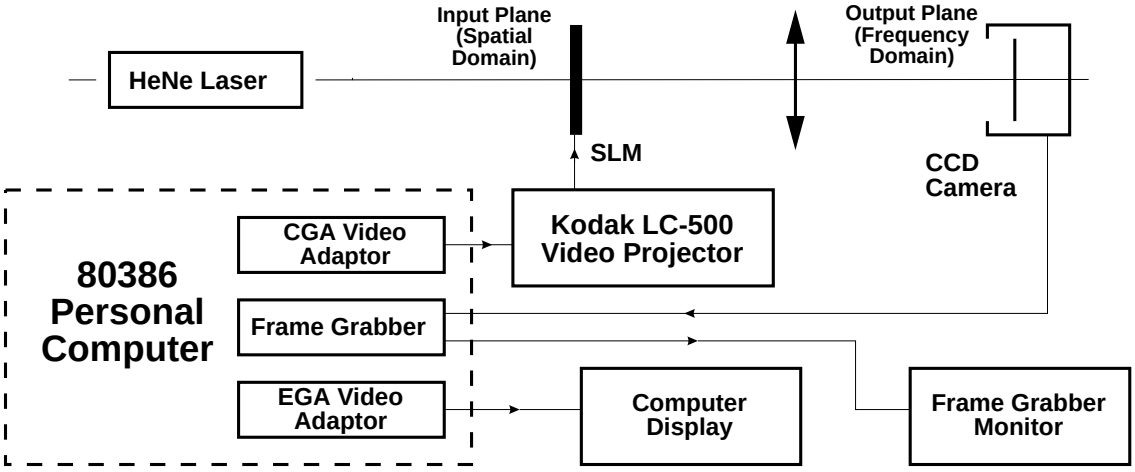


Figure 4-8: Block diagram of the optical Fourier transformer and computer control system. An input to the optical processor is generated by the CGA card and its transform is acquired by the CCD camera and frame grabber.

An input to the optical processor, shown at the top of Figure 4-8, is generated by the CGA (color graphics adaptor) video card and its Fourier transform is acquired by the CCD camera and frame grabber. A software package was written that allowed arbitrary 2-D signals to be written to the spatial light modulator through the CGA card and its Fourier transform to be read back from the CCD array through the frame grabber. The computer controlled optical processor could calculate the 2-D Fourier transform of arbitrary input signals at video rates. A photograph of the optical Fourier transformer is shown in Figure 4-9.

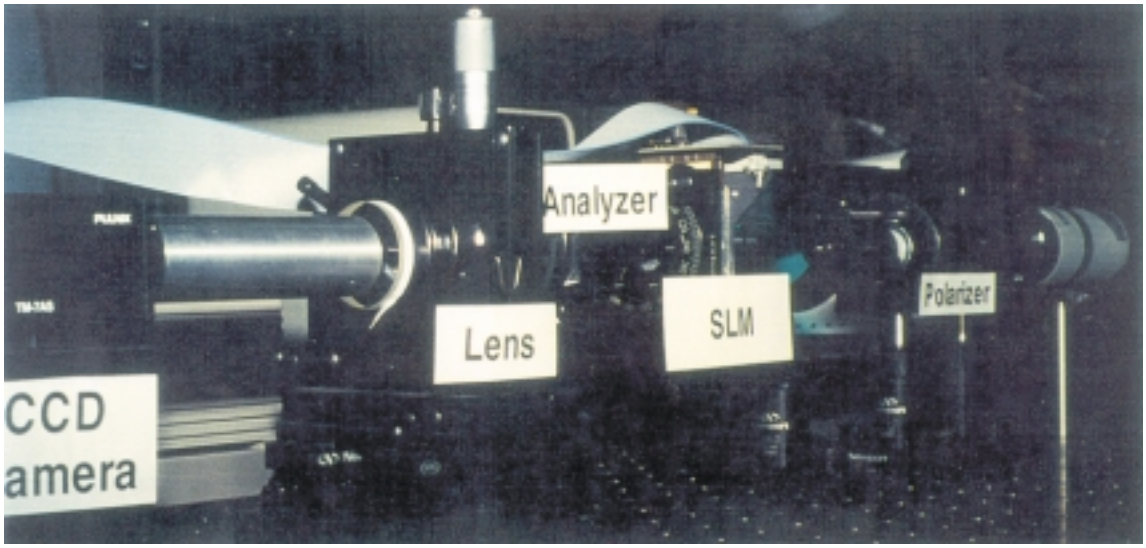


Figure 4-9: Photograph of the optical Fourier transformer. The HeNe laser is visible on the extreme left of the photograph followed by the polarizer, SLM, analyzer, lens, and CCD camera.

The controlling 80386 computer was equipped with two video cards and a frame grabber. The address decoding circuitry of the CGA video card was modified to allow it to be co-resident with a second EGA (extended graphics adaptor) video card. The input and output video sub-systems and the computer control software are briefly discussed in the following sections.

4.3.1 SLM Video Signal

A CGA video card in the PC was used to generate the video signal for the SLM driving electronics. The address and port I/O decoding circuitry on the video card were modified such that the card could reside in the same computer as the EGA video card used to drive the primary display.

The spatial light modulator driving electronics were left in the video projector chassis and the SLM was connected to the driving electronics via a 26-conductor ribbon cable. The phase-locked loop (PLL) used for CGA mode timing in the video projector was modified to correct an inaccurate pixel-clock frequency. The driver circuitry in the video projector supported only binary images (each SLM pixel must be either transparent or opaque) and as such no grey-scale capabilities were available. The image on the SLM could be refreshed at video rates.

4.3.2 CCD Video Signal

The frequency domain image in the back plane of the Fourier lens was recorded by the CCD camera and its RS-170 signal was digitized in the computer by an ImageNation CX-100 frame grabber. Fields rather than frames were grabbed in a low resolution 256 (H) by 243 (V) mode with 8 bits of resolution or 256 grey levels. New fields could be acquired and digitized every 1/30 of a second and each field required 60 kbytes of storage space.

4.3.3 Software

A software package was written for the optical Fourier transformer to demonstrate its processing abilities. The software is responsible for writing an

arbitrary 2-D input signal on the spatial light modulator, acquiring and digitizing its Fourier transform, and then saving the result to a mass storage device. The input signal and its Fourier transform can be viewed in real-time on the computer display and the frame grabber monitor respectively.

The software includes routines to generate and process four types of 2-D input signals:

1. Sinusoids of spatial frequencies (ν_x, ν_y)
2. Rectangular apertures with dimensions (x_0, y_0)
3. Circular apertures of radius r_0
4. Bit-mapped images

The parameters of the first three input types can be modified and their Fourier transforms are updated in real-time. A software calibration routine can be executed at start-up to search the input and output planes for their respective origins. This routine locates the origin of the input plane's coordinate system on the SLM, and the origins of the zero- and replicated first-order spectra on the CCD array.

An input signal and its Fourier transform can be viewed in real-time on separate display monitors. In order to maximize dynamic range, the maximum intensity of the Fourier transform image was also displayed in real-time permitting interactive modification of the CCD integration time. Fourier transform images can be saved to a disk file and loaded into MATLAB for post-processing, plotting on a 3-D axis, or hard-copy generation.

Chapter 5
Experimental Results

The purpose of this chapter is to present a selection of the spectra processed with the optical Fourier transformer during its characterization and to identify a strategy that allows one to interpret these 2-D optical Fourier transforms (OFT) in terms of the familiar discrete Fourier transform (DFT).

An optical Fourier processor calculates the continuous Fourier transform of a discrete input signal. The effects of reconstructing a discrete input signal on the spatial bandwidth and frequency resolution of the optical Fourier transformer are determined in the first half of the chapter. The pixel dimensions, measured during SLM characterization in the previous chapter, are used to describe the frequency domain parameters of the optical Fourier transformer. The power spectra of selected sinusoidal input functions that were processed by the optical Fourier transformer are presented and discussed as a conclusion to the chapter.

5.1 Optical Fourier Transform Spectra

It is instructive to interpret an optical Fourier transform using the same framework as would be used for a discrete Fourier transform. The input to an optical Fourier transformer is discrete and it must be converted to a continuous form, or rather, it must be reconstructed by the spatial light modulator, before it is transformed by the inherently continuous optical Fourier transform. The following three sections describe the bandwidth, frequency resolution, and modulation transfer function (MTF) of an optical Fourier processor using a DFT framework.

5.1.1 Bandwidth

The bandwidth of an optical Fourier processor is determined by one of three limiting factors: (1) the wavelength of light used in the processor; (2) the bandwidth of the optical processor itself; and (3) the resolution of the spatial light modulator. It was the resolution of the spatial light modulator that limited the bandwidth of the optical processor in the current work.

5.1.1.1 Fundamental Bandwidth of Light

The spatial bandwidth of free-space is generally regarded to be $1/\lambda$ cycles per unit length. Recall that a paraxial wave propagating in the *z*-direction has a wavevector given by $k_z = (k^2 - k_x^2 - k_y^2)^{1/2}$. The wavevector must be real-valued for the wave to propagate through space unattenuated which restricts $(\nu_x^2 + \nu_y^2)^{1/2} = \nu$ to values less that $1/\lambda$. We may therefore regard $1/\lambda$ as a spatial cutoff frequency and define the spatial bandwidth of light propagation in free space to be $1/\lambda$ cycles per unit length. In other words details smaller than λ spatial units cannot be transmitted by an optical wave of wavelength λ.

5.1.1.2 Bandwidth of the Optical Processor

The spatial resolution of a single-lens optical system was derived in chapter two and given by Equation [2-34]. The spatial bandwidth of a single-lens system is simply the inverse of its spatial resolution,

$$\nu_s = (r_{\min})^{-1} = \frac{1}{1.22\lambda}\,\frac{D}{f} \quad \left[\frac{\text{cycles}}{\text{unit length}}\right] \qquad \textbf{[5-1]}$$

where *D* is the diameter of the lens, *f* is its focal length, and λ is the wavelength of light. Again note the $1/\lambda$ dependence.

5.1.1.3 Resolution of the Spatial Light Modulator

Information theory says that the sampling frequency of a band-limited signal must be at least twice its bandwidth in order to reconstruct the original signal without errors. A spatial light modulator re-constructs a sampled signal using a spatial frequency determined by its pixel pitch. A signal reconstructed by a spatial light modulator will have bandwidth,

$$B_x = \frac{1}{2\Delta x_{SLM}}, \quad \text{and} \quad B_y = \frac{1}{2\Delta y_{SLM}} \quad \left[\frac{\text{cycles}}{\text{unit length}}\right], \qquad \text{[5-2]}$$

along the ν_x- and ν_y-directions where Δx_{SLM} and Δy_{SLM} represent SLM pixel pitch in the *x*- and *y*-directions respectively.

5.1.2 Frequency Resolution

The frequency resolution of an optical Fourier transformer is determined by the diameter of the beam incident on its spatial light modulator. The SLM is illuminated by a Helium-Neon laser that oscillates in a TEM_{00} transverse spatial mode. This fundamental mode has a Gaussian amplitude profile. The amplitude of the plane waves incident on the spatial light modulator therefore has a Gaussian amplitude distribution which provides a built-in window function for the optical Fourier processor. The amplitude of the beam as a function of spatial coordinates in the *x*-*y* plane at the SLM is given by,

$$w(x,y) = e^{-\frac{1}{4}\left[\frac{x^2}{\sigma_x^2} + \frac{y^2}{\sigma_y^2}\right]}, \qquad \text{[5-3]}$$

where σ_x and σ_y are the power-rms widths[6] of the Gaussian beam. The width of

[6]The power-rms width of a function *f*(*x*) is the root-mean-square (rms) width (continued...)

a Gaussian laser beam is usually stated in terms of its waist-radius[7]. The waist-radii w_x and w_y of a Gaussian laser beam are related to its power-rms widths by the following relation,

$$\sigma_x = \frac{1}{2} w_x \quad \text{and} \quad \sigma_y = \frac{1}{2} w_y, \qquad [5\text{-}4]$$

The shape and width of the window function $w(x,y)$ determine the spectral characteristics of the Fourier processor. The frequency resolution is proportional to the width of the Gaussian window's Fourier transform,

$$W(\nu_x, \nu_y) = \frac{1}{4\pi \sigma_{\nu x} \sigma_{\nu y}} e^{-\frac{1}{4}\left[\frac{\nu_x^2}{\sigma_{\nu x}^2} + \frac{\nu_y^2}{\sigma_{\nu y}^2}\right]}, \qquad [5\text{-}5]$$

where the spectral power-rms widths are given by,

$$\sigma_{\nu x} = \frac{1}{4\pi \sigma_x} \quad \text{and} \quad \sigma_{\nu y} = \frac{1}{4\pi \sigma_y}, \qquad [5\text{-}6]$$

Using the Schwarz inequality it can be shown that the product of the power-rms widths of the window function, and the spectral power-rms widths of the Fourier transform of the window function, must be greater or equal to $1/4\pi$, as described by the duration-bandwidth reciprocity relation,

$$\sigma_x \sigma_{\nu x} \geq \frac{1}{4\pi} \quad \text{and} \quad \sigma_y \sigma_{\nu y} \geq \frac{1}{4\pi}, \qquad [5\text{-}7]$$

In other words spatial extent and spectral width cannot simultaneously be made arbitrarily small. From Equation [5-6] it is obvious that the Gaussian window has minimum permissible value of the duration-bandwidth product.

---

[6](...continued)
of its squared-absolute value $|f(x)|^2$. This is the appropriate measure of width for functions with negative or complex values.

[7]The waist-radius of a Gaussian laser beam is the half-width at e^{-1}-maximum amplitude or half-width at e^{-2}-maximum intensity.

The spectral resolution may now be determined by substituting Equation [5-4] into Equation [5-6]. The spectral resolution of an optical Fourier transformer is given by,

$$\Delta\nu_r = \sigma_{\nu x} = \sigma_{\nu y} = \frac{1}{2\pi w} \quad \left[\frac{\text{cycles}}{\text{unit length}}\right], \qquad \textbf{[5-8]}$$

when it is illuminated by a Gaussian beam of waist-radius w spatial units.

5.1.3 Modulation Transfer Function

The modulation transfer function (MTF) of an optical system represents its spatial frequency response to a point source input, or more specifically, the modulus of the system's optical transfer function (OTF). At a given frequency the MTF is equivalent to the peak-to-peak response of an aperture as it is scanned across a sinusoidal pattern.

The reconstruction aperture of a spatial light modulator and its optical transfer function are a Fourier transform pair. A spatial light modulator with rectangular pixels has a reconstruction-aperture optical-transfer-function pair given by,

$$\Pi\left(\frac{x}{\delta x}, \frac{y}{\delta y}\right) \quad \Leftrightarrow \quad \delta x\, \delta y\, sinc\left(\frac{\nu_x}{1/\delta x}, \frac{\nu_y}{1/\delta y}\right), \qquad \textbf{[5-9]}$$

where δx and δy represent the dimensions of each SLM pixel (note the SLM subscript has been dropped for simplicity). The modulation transfer function is simply the absolute value of the sinc function on the LHS of Equation [5-9]. It represents a low-pass filter with shallow high frequency roll-off and equivalent-noise bandwidth (ENB) $\pm 1/2\delta x$ and $\pm 1/2\delta y$ cycles per spatial unit. A reconstructed signal is completely attenuated by the MTF at the zeros of the sinc function which occur at $\pm n/\delta x$ and $\pm m/\delta y$ cycles per spatial unit, where n and m are non-zero integers.

In order to determine how the modulation transfer function effects the spectrum of a sampled signal it is instructive to review how the signal is reconstructed by the spatial light modulator. First consider the reconstruction of a 1-D temporal signal.

5.1.3.1 Reconstruction of 1-D Temporal Signal

Consider a continuous temporal signal $f(t)$. If the signal is sampled every Δt seconds it can be represented mathematically by,

$$f_s(t) = f(t) \cdot \text{Ш}\left(\frac{t}{\Delta t}\right), \qquad \textbf{[5-10]}$$

where the continuous signal $f(t)$ is assumed to be band-limited such that its bandwidth $B < (2\Delta t)^{-1}$. The frequency domain representation of the sampled function is given by its Fourier transform,

$$F_s(\nu) = F(\nu) * \Delta t \,\text{Ш}(\nu\,\Delta t) = \sum_{n=-\infty}^{\infty} F\left(\nu - \frac{n}{\Delta t}\right), \qquad \textbf{[5-11]}$$

where $F_s(\nu)$ and $F(\nu)$ are the Fourier transforms of the sampled and continuous signals respectively. It is clear from Equation [5-11] that the spectrum of a sampled 1-D temporal signal is a series of replicated spectra separated in frequency space by $\nu' = 1/\Delta t$. The spectrum of a sampled signal is illustrated in Figure [5-1].

A band-limited signal sampled at twice its bandwidth can be reconstructed without error. Perfect reconstruction however requires an infinite-order interpolation between the samples using a sinc function of infinite extent. In practice signal reconstruction is done using zero-, first-, or second-order holds which correspond to constant, linear, and quadratic interpolation respectively. If

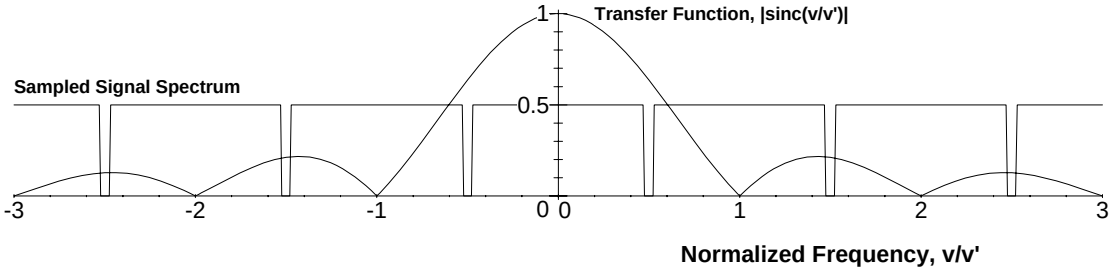


Figure 5-1: Spectrum of a sampled 1-D temporal signal and the transfer function of a zero-order hold interpolation function. The signal is sampled at $\nu' = 1/\Delta t$.

the sampled signal $f_s(t)$ is reconstructed using zero-order hold interpolation, the reconstructed signal can be represented by,

$$f_r(t) = f_s(t) * \Pi\left(\frac{t}{\Delta t}\right) = \left[f(t) \cdot \text{III}\left(\frac{t}{\Delta t}\right)\right] * \Pi\left(\frac{t}{\Delta t}\right), \qquad \textbf{[5-12]}$$

where the replicating property of convolution has been used to generate each zero-order hold of length Δt and amplitude $f_s(t)$. The spectrum of the reconstructed signal is given by its Fourier transform,

$$F_r(\nu) = \Delta t \ \text{sinc}(\nu \Delta t) \cdot F_s(\nu) = \Delta t \ \text{sinc}(\nu \Delta t) \sum_{n=-\infty}^{\infty} F\left(\nu - \frac{n}{\Delta t}\right), \qquad \textbf{[5-13]}$$

Note that the sampled spectrum is modulated by the transfer function of the zero-order hold interpolator - the sinc function of Equation [5-9]. It functions as a low-pass reconstruction filter as illustrated in Figure 5-1. The filter doesn't have an optimum brick-wall cutoff at $\nu'/2$ cycles per second and consequently the amplitude of the desired spectra centred on the origin is tapered while frequency components from other replicated spectra are not completely attenuated.

5.1.3.2 Reconstruction of 2-D Spatial Signal

Consider a continuous spatial signal $f(x,y)$ in 2-D. If the signal is sampled every Δx and Δy spatial units in the x- and y-directions respectively it can be represented mathematically by,

$$f_s(x,y) = f(x,y) \cdot \text{Ш}\left(\frac{x}{\Delta x}, \frac{y}{\Delta y}\right), \qquad \text{[5-14]}$$

where the continuous signal $f(x,y)$ is assumed to be band-limited such that its bandwidth $B_x < (2\Delta x)^{-1}$ and $B_y < (2\Delta x)^{-1}$. The frequency domain representation of the sampled function is given by its Fourier transform,

$$F_s(\nu_x, \nu_y) = F(\nu_x, \nu_y) * \Delta x \Delta y \, \text{Ш}(\nu_x \Delta x, \nu_y \Delta y) = \sum_{n=-\infty}^{\infty} \sum_{m=-\infty}^{\infty} F\left(\nu_x - \frac{n}{\Delta x}, \nu_y - \frac{m}{\Delta y}\right), \qquad \text{[5-15]}$$

where $F_s(\nu_x,\nu_y)$ and $F(\nu_x,\nu_y)$ are the Fourier transforms of the sampled and continuous signals respectively. It is clear from Equation [5-15] that the spectrum of a sampled 2-D spatial signal is a series of replicated spectra separated in frequency space by $1/\Delta x$ cycles per spatial unit in the ν_x-direction and $1/\Delta y$ cycles per spatial unit in the ν_y-direction.

A spatial light modulator uses zero-order hold interpolation during signal reconstruction but the area of the zero-order hold is less that the area of the sampling interval. The active area of a SLM pixel is a rectangular region centred on the pixel with dimensions δx and δy over which the samples are interpolated with a zero-order hold. The non-active region around the edge of each pixel is referred to as dead space. A spatial light modulator's *fill factor* is defined as the ratio of its active area to its pixel area,

$$\text{Fill Factor} = \frac{\text{Active Area}}{\text{Pixel Area}} = \frac{\delta x\, \delta y}{\Delta x\, \Delta y}, \qquad \textbf{[5-16]}$$

where δx and δy represent the pixel width. If the sampled signal $f_s(x,y)$ from Equation [5-14] is reconstructed by a spatial light modulator using zero-order hold interpolation, the reconstructed signal can be represented by,

$$f_r(x,y) = f_s(x,y) * \Pi\left(\frac{x}{\delta x}, \frac{y}{\delta y}\right) = \left[f(x,y) \cdot \text{Ш}\left(\frac{x}{\Delta x}, \frac{y}{\Delta y}\right)\right] * \Pi\left(\frac{x}{\delta x}, \frac{y}{\delta y}\right), \qquad \textbf{[5-17]}$$

where the replicating property of convolution has been used to generate each zero-order hold of pitch (Δx,Δy), width (δx,δy), and amplitude $f_s(x,y)$. The spectrum of the reconstructed signal is given by its Fourier transform,

$$F_r(\nu_x, \nu_y) = \delta x \delta y\ \text{sinc}\left(\frac{\nu_x}{1/\delta x}, \frac{\nu_y}{1/\delta y}\right) \sum_{n=-\infty}^{\infty} \sum_{m=-\infty}^{\infty} F\left(\nu_x - \frac{n}{\Delta x}, \nu_y - \frac{m}{\Delta y}\right), \qquad \textbf{[5-18]}$$

Note that the replicated spectra are pre-multiplied by the modulation transfer function from Equation [5-9]. The MTF and spectrum of a sampled signal for a SLM with square pixels are illustrated in Figure 5-2.

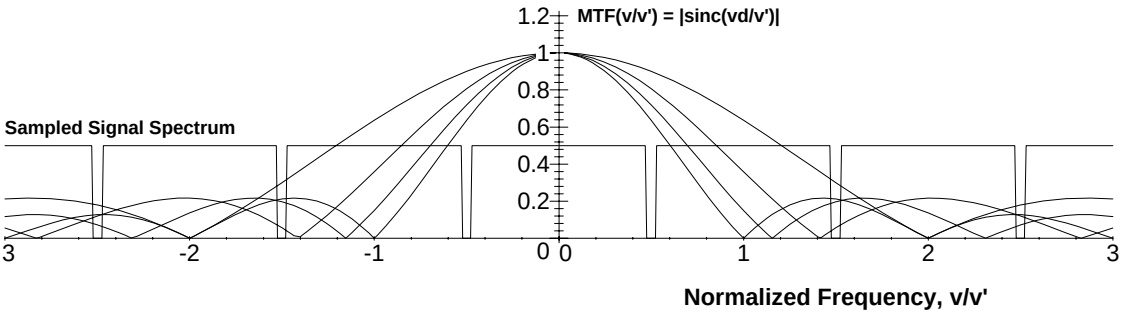


Figure 5-2: The modulation transfer function (MTF) and spectrum of a sampled 2-D signal along a co-ordinate axis for a SLM with square pixels and 100, 75, 50, and 25 percent fill factors.

Modulation transfer functions for SLMs with 100, 75, 50, and 25 percent fill factors are illustrated in the figure. The MTF with the narrowest bandwidth represents a SLM with a 100 percent fill factor while the MTF with the widest

bandwidth represents a SLM with a 25 percent fill factor. When the fill factor is 100 percent, the noise equivalent bandwidth of the MTF is equal to the bandwidth of the signal, and the MTF behaves like a low-pass reconstruction filter. As the SLM fill factor is increased, the noise equivalent bandwidth of the MTF increases, and the reconstruction filter allows more power from the replicated spectra to be reconstructed. The consequences of unity, fractional, and zero fill factors are discussed below.

Unity Fill Factor

The modulation transfer function behaves like a reconstruction filter with noise equivalent bandwidth equal to the bandwidth of the sampled signal. The zero-order spectrum (the spectrum at the origin) is tapered by the MTF and the replicated spectra are not completely attenuated. The highest frequency of the zero-order spectrum is attenuated by 3.9 dB.

Fractional Fill Factor

The modulation transfer function behaves like a reconstruction filter with noise equivalent bandwidth greater than the bandwidth of the sampled signal. The highest frequency of the zero-order spectrum is attenuated by less that 3.9 dB and more of the replicated spectra is reconstructed.

Zero Fill Factor

In the limit as the fill factor approaches zero, the modulation transfer function approaches unity,

$$\lim_{\delta x, \delta y \to 0} \delta y \, \delta x \, \mathrm{sinc}\left(\frac{\nu_x}{1/\delta x}, \frac{\nu_y}{1/\delta y}\right) = 1, \qquad \text{[5-19]}$$

and the bandwidth of the reconstruction filter approaches infinity. Each SLM pixel no longer has a built-in low-pass filter and consequently the zero-order spectrum and all replicated spectra are reconstructed without attenuation.

5.1.4 Summary

A spatial light modulator and its reconstructed spectrum can be described by a set of three complementary parameter pairs; each spatial parameter has a frequency domain complement. The spatial light modulator reconstruction parameters and their complementary frequency domain representations are summarized in Table 5-1. It is clear that bandwidth is determined by sampling period, frequency resolution is determined by sampling interval, and the effective noise bandwidth of the modulation transfer function is determined by the size of the reconstruction aperture. There is a one-to-one relationship between each of the complementary parameters. The relationship between the first two parameter pairs in Table 5-1 is identical to a discrete Fourier transform. The last parameter pair is unique to an optical Fourier transform.

Table 5-1:
SLM reconstruction parameters and their complementary frequency domain representations.

Spatial Domain		→	Frequency Domain	
Sampling Period [µm]	Δx_{SLM}, Δy_{SLM}		Bandwidth [cycles/mm]	$B_x = 1/2\Delta x_{SLM}$ $B_y = 1/2\Delta y_{SLM}$
Sampling Interval [µm]	Gaussian window of waist radius w		Resolution [cycles/mm]	$\Delta\nu_r = 1/2\pi w$
Reconstruction Aperture [µm]	δx_{SLM}, δy_{SLM}		MTF Bandwidth [cycles/mm]	$ENB_x = 1/2\delta x_{SLM}$ $ENB_y = 1/2\delta y_{SLM}$

5.2 Optical Fourier Transformer Characterization

Three relationships between parameters in the spatial and frequency domains were developed in the previous section. Using the values determined for pixel pitch and width in the SLM characterization described in the previous chapter, it is easy to calculate the frequency domain parameters of the optical Fourier transformer. The bandwidth, frequency resolution, and equivalent noise bandwidth of the modulation transfer function are summarized in Table 5-2. The table also includes the fundamental bandwidth of light for a Helium-Neon laser at 632 nm and the optical bandwidth of the single lens system. All spatial frequencies are in units of cycles/cm.

Table 5-2:
Summary of Optical Fourier Transformer Frequency Domain Specifications

Frequency Domain Parameter	ν_x-axis	ν_y-axis	units
Bandwidth, B_x and B_y	62	55	cycles/cm
Frequency Resolution, $\Delta\nu_r$	6		cycles/cm
MTF Bandwidth, ENB_x and ENB_y	89	84	cycles/cm
Fundamental Bandwidth of Light, $1/\lambda$	15 800		cycles/cm
Imaging System Bandwidth, ν_s	3948		cycles/cm

5.2.1 Bandwidth

The spatial bandwidth of an optical Fourier transformer is determined by its SLM pixel pitch and is represented in the frequency domain by the extent of its zero-order spectrum. Figure 5-3 illustrates the spatial bandwidth of the optical Fourier transformer along the ν_x-direction.

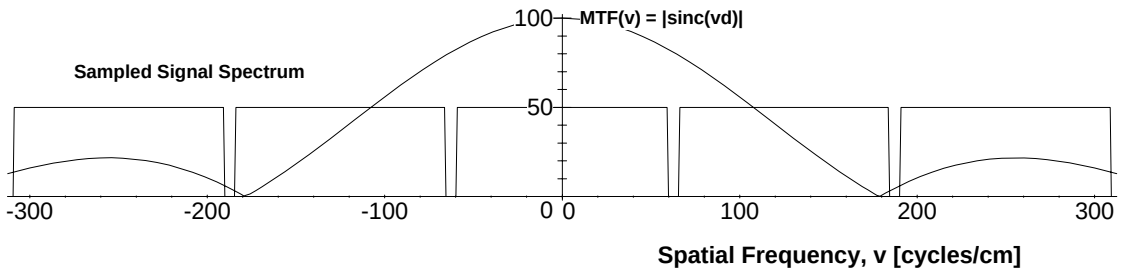


Figure 5-3: Spatial bandwidth of the optical Fourier transformer along the ν_x-axis as defined by the zero-order sampled spectrum and its modulation transfer function (MTF).

The ν_x-axis bandwidth is 62 cycles/cm. The modulation transfer function attenuates the zero-order spectrum by 1.8dB at ±62 cycles/cm. The zero-order spectrum along the ν_y-axis is attenuated by 1.7dB at ±55 cycles/cm.

5.2.2 Frequency Resolution

The frequency resolution of an optical Fourier transformer is determined by the spatial extent or waist-radius of the Gaussian laser beam on the SLM. Figure 5-4 shows the frequency domain of the Fourier transformer for unity input. The zero-order spectrum is shown at the origin and the first-order spectra are shown centred on ν = ±124 cycles/cm. The width of the Gaussian pulses indicates the frequency resolution. The frequency resolution is 6 cycles/cm which is equivalent to a standard deviation of 12 cycles/cm.

5.3 Experimental Results

A selection of the Fourier spectra that were processed by the optical transformer are presented in this section. The 2-D input function written to the SLM, a photograph of its 2-D spectrum in the Fourier plane, and the zero-order 3-D intensity function acquired from the Fourier plane, are illustrated for each processing example. The 3-D intensity functions represent the light intensity

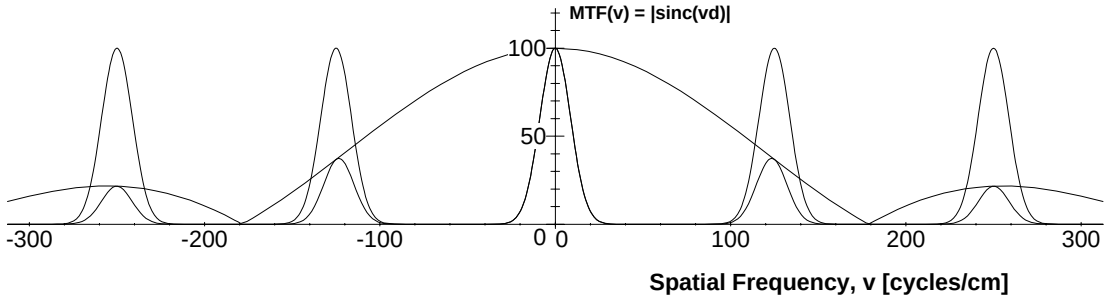


Figure 5-4: Frequency resolution of the optical Fourier transformer. The figure shows the magnitude spectrum of unity input with the modulation transfer function.

observed in the zero-order spectrum by the CCD camera. The captured 2-D images were cropped such that only the information in the zero-order spectrum was retained and all higher-order spectra were discarded. No further post-processing of the raw CCD image was done. The zero-order spectra are displayed on a linear 3-D coordinate axis were the *x*- and *y*-axes are scaled for spatial frequency and the *z*-axis represents light intensity and is proportional to the power of the signal in the Fourier plane. The Fourier spectra illustrated in this section therefore represent the power spectrum of the input signal rather than its amplitude or phase spectrum. Recall that the phase information is lost by the inherent amplitude squaring function of the CCD array.

The figures in this section that illustrate the 2-D input function written to the LCD are photographs of an SLM preview window generated by computer. The preview window shows 21x21 pixels from the LCD display. The area of the SLM previewed by the window is illustrated by the small box in Figure 5-5. The black dot in the box represents the diameter of the laser beam and its diameter is equivalent to the circle drawn in the preview window. The intensity profile of the laser beam and the SLM pixels it illuminates are shown in Figure 5-6. The outer circle in the figure has the same diameter as the back dot in the previous figure and the inner circle represents the HeNe beam diameter. The pixels illuminated

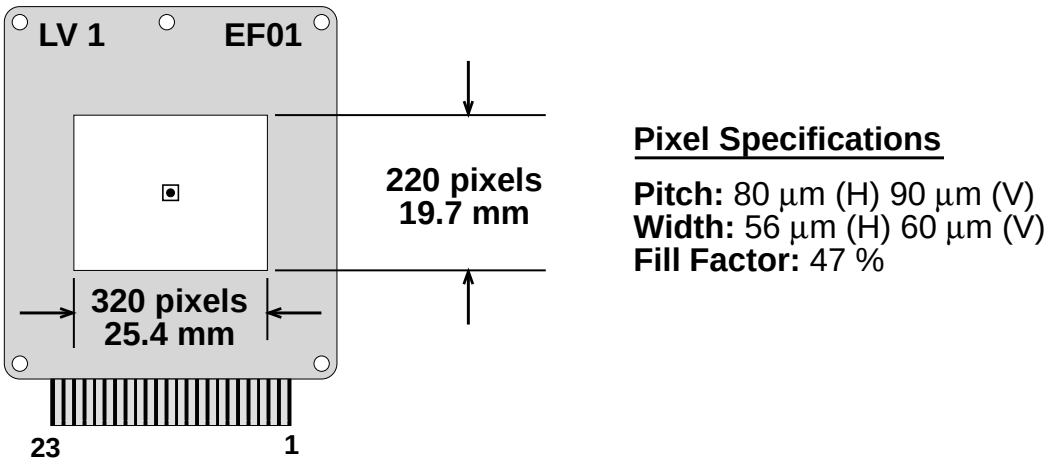


Figure 5-5: The Liquid crystal SLM. The small box in the center of the screen indicates the area that is displayed in the SLM preview window and the black dot represents the circle in the preview window.

by the beam are drawn to scale -- the white boxes represent individual pixels and the dark grid represents the dead space between pixels.

It seemed appropriate to characterize the operation of the optical Fourier transformer with simple 2-D sinusoidal inputs. The low resolution and binary grey-scale nature of the spatial light modulator however restricted the input function to band-limited 2-D square waves. A single sinusoidal input function can be generated by mapping a square wave onto the SLM if its fundamental frequency is greater than one-third of the SLM's bandwidth; only the fundamental frequency will be reconstructed and all its harmonics, which occur at odd multiples of the fundamental frequency, will fall outside the bandwidth of the optical Fourier processor and can be ignored. If the fundamental frequency of the square wave is less than one-third of the bandwidth, then the odd harmonics with frequency less than the bandwidth will appear in the optical Fourier transform spectrum. In addition to at least one sinusoid, the square wave will also contain a DC level. SLM pixels can be either on or off and consequently there is always a DC component in the output spectrum.

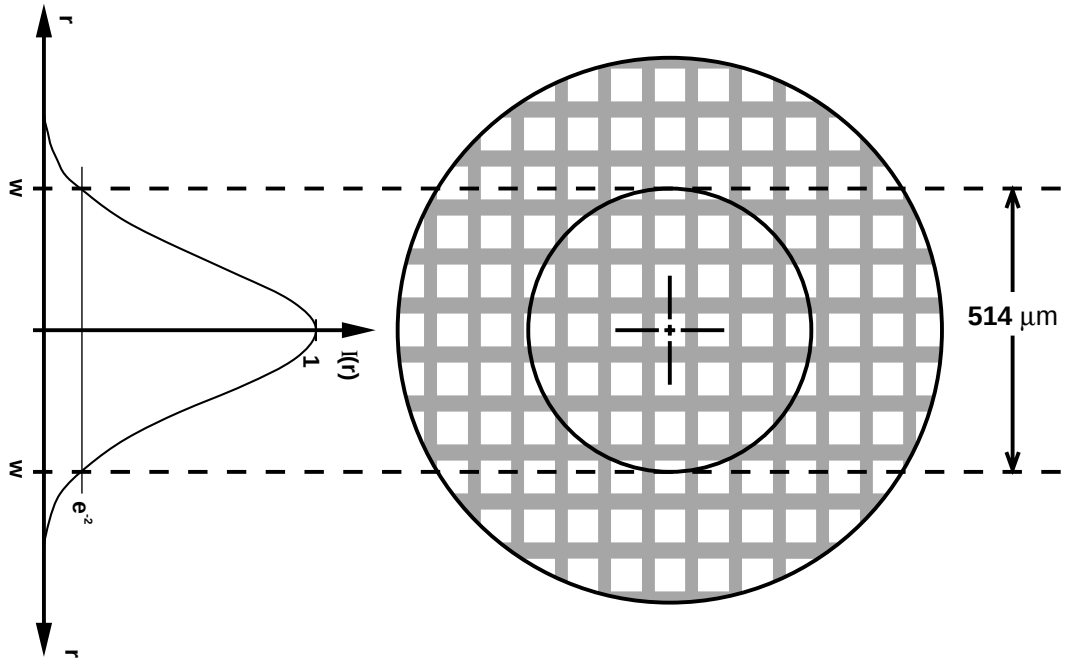
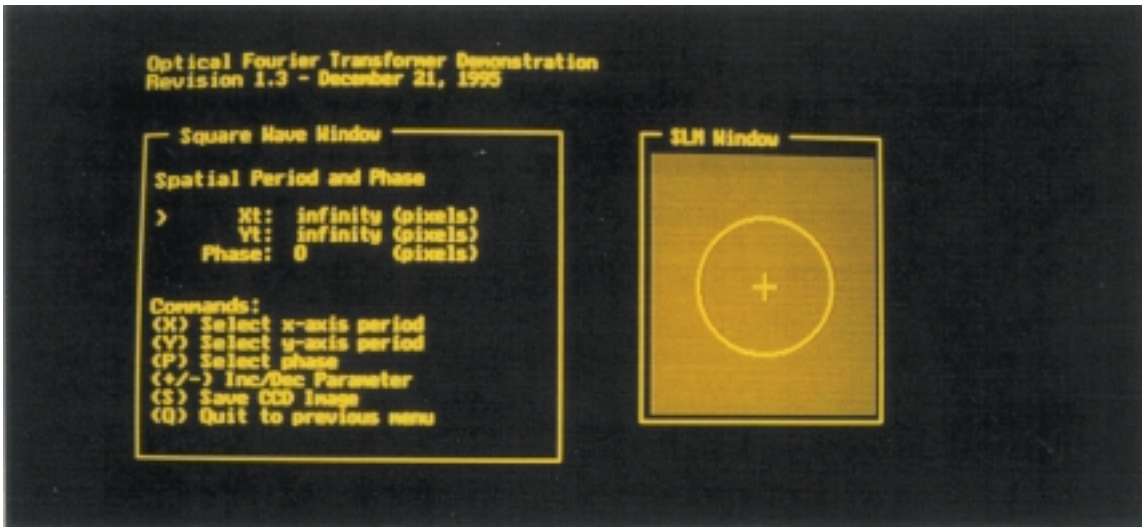
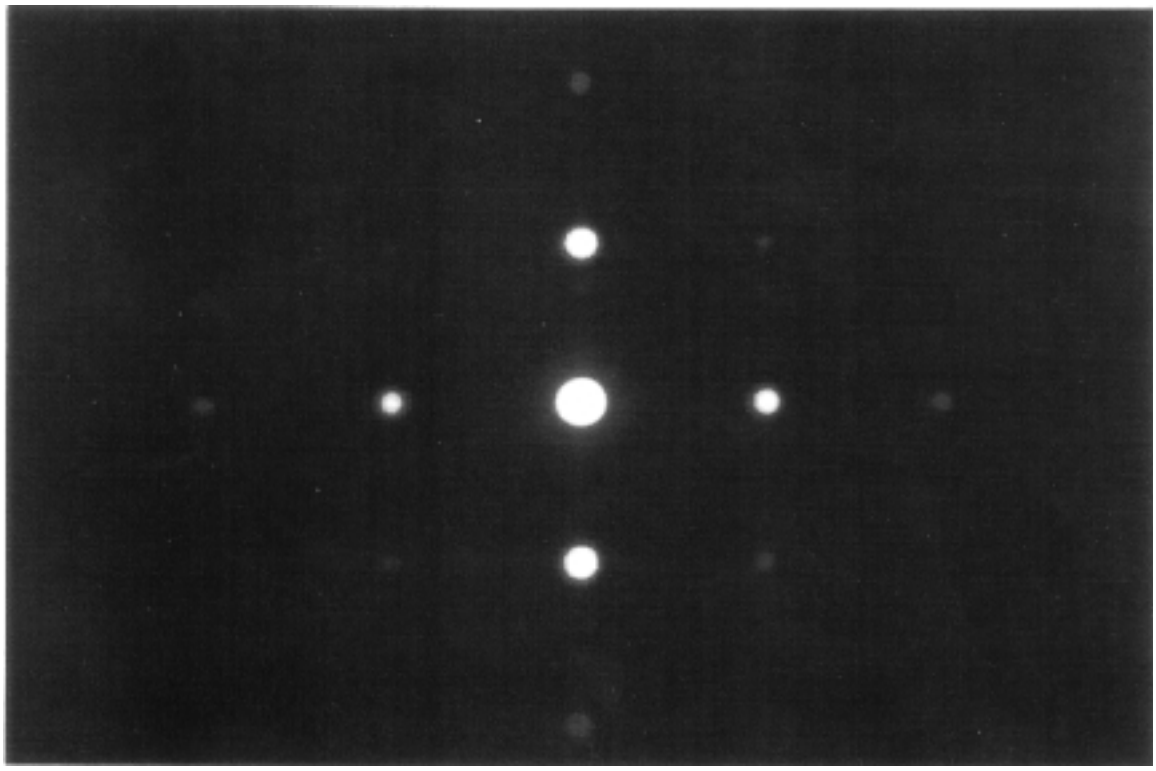


Figure 5-6: The SLM pixels illuminated by the 514 μm diameter beam. Beam intensity is shown and the SLM pixels illuminated by the Gaussian beam are indicated. The white boxes represent pixels and the shaded grid represents dead space.

The presentation of optical Fourier spectra is divided into three sections. The spectrum of a constant input is considered first. The spectrum of a single sinusoid, where its component spatial frequencies along both directions can take on non-zero values, is considered next. Finally the spectrum of several harmonically related sinusoids along a single direction is considered.



(a) SLM Input Plane



(b) Fourier Plane

Figure 5-7: The optical Fourier transform (power spectrum) of a constant input: (a) An illustration of the constant input function f(x,y) = 1 written to the SLM, and (b) its optical transform observed in the Fourier plane.

5.3.1 Constant Input

The constant function $f(x,y) = 1$ and its optical Fourier spectrum are illustrated in Figures 5-7(a) and 5-7(b) respectively; the zero-order 3-D intensity function is illustrated in Figure 5-7(c). The single Gaussian spike at the origin represents the DC component of the input signal. The poor frequency resolution of the system is quite evident in Figure 5-7(c); an ideal Fourier transformer would generate a delta function at the origin.

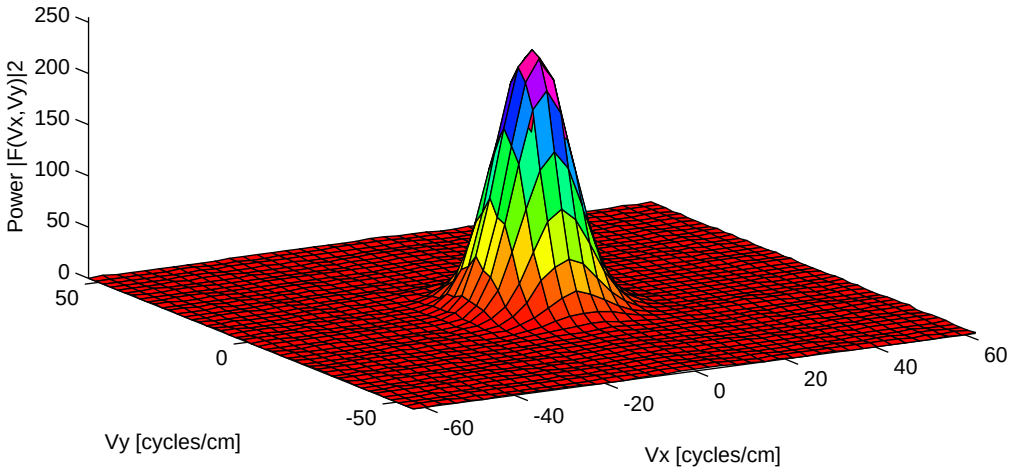


Figure 5-7(c): The zero-order spectrum from Figure 5-7(b). The Gaussian spike at the origin represents the DC component of the signal ($\nu_x = \nu_y = 0$).

The theoretical response, along the ν_x-axis, to a constant input function was plotted in Figure 5-4. The 1-D frequency resolution shown there very closely resembles the frequency resolution indicated by the 2-D spectrum illustrated in Figure 5-7(c). The Gaussian spikes appear to have a similar bandwidth.

5.3.2 Single Cosinusoid Input

Consider the power spectrum of a single cosinusoid whose frequency components along both coordinate axes can assume any value. This function can be represented mathematically by,

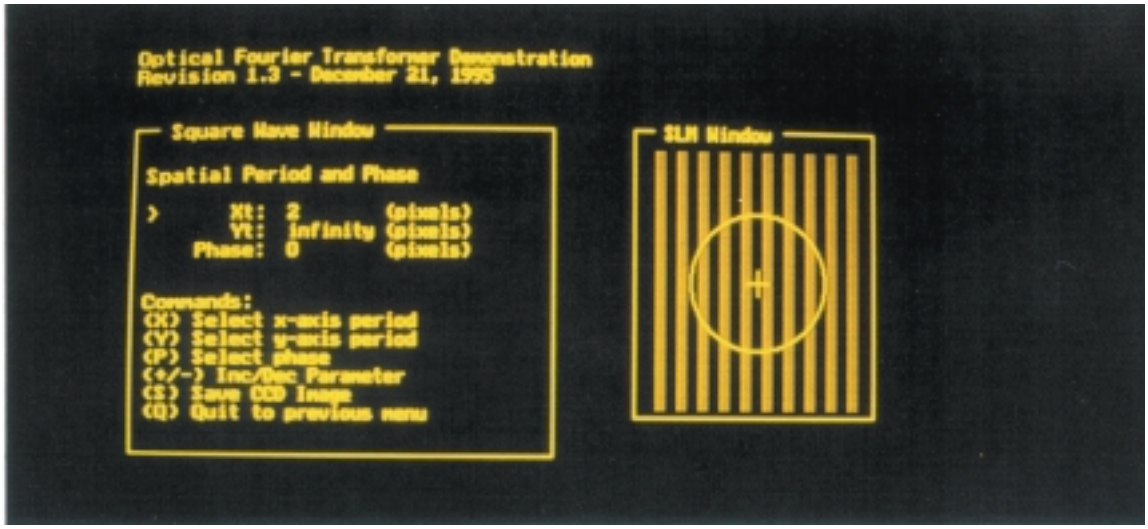
$$f(x,y) = 1 + \cos\left[2\pi\left(\nu_x x + \nu_y y\right)\right], \qquad \textbf{[5-20]}$$

where ν_x and ν_y are the spatial frequency components and must be greater than one-third of the bandwidth in their respective directions to guarantee that the input function consists of only a single cosinusoid. The power spectra of three functions of this form were calculated using the optical Fourier transformer and are illustrated in Figures 5-8 through 5-10. The spatial frequency components for each of the three input functions and the figure number that illustrates its power spectrum, are summarized in Table 5-3.

Table 5-3:
Power spectra of functions containing a constant DC level and a single cosinusoid

Figure Number	Frequency ν_x	Frequency ν_y	
Figure 5-8	B_x = 63	0	cycles/cm
Figure 5-9	0	B_y = 56	cycles/cm
Figure 5-10	B_x = 63	B_y = 56	cycles/cm

A 2-D cosinusoid, periodic in the *x*-direction and constant in the *y*-direction, was written to the SLM and is illustrated in Figure 5-8(a) -- the input cosinusoid has lines of constant phase parallel to the *y*-axis. Its optical Fourier transform (power spectrum) is illustrated in Figure 5-8(b); the spatial frequency components are 63 and 0 cycles/cm along the *x*- and *y*-axis respectively.



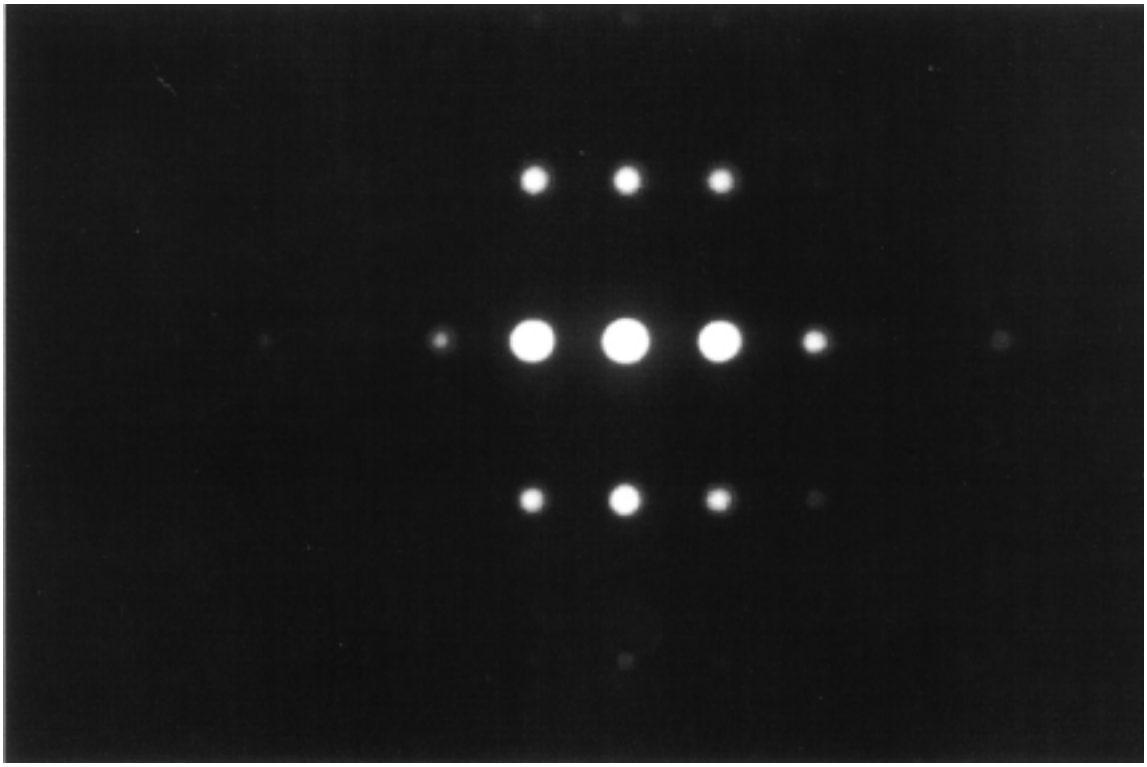


Figure 5-8: The optical Fourier transform (power spectrum) of $f(x,y) = 1 + \cos(2\pi\upsilon_x x)$: (a) The input function written to the SLM, and (b) its optical transform observed in the Fourier plane.

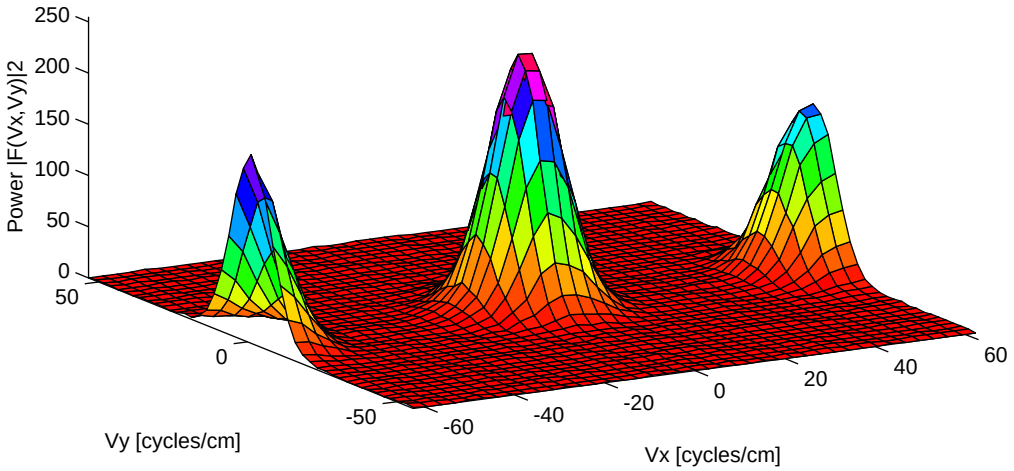
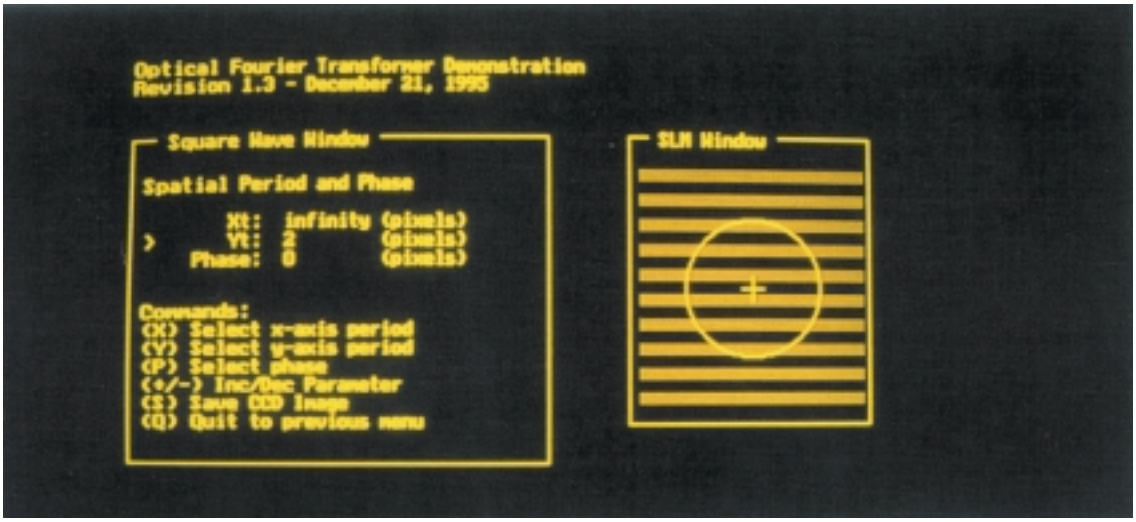


Figure 5-8(c): The zero-order spectrum from Figure 5-8(b). The input function is $f(x,y) = 1 + \cos(2\pi\upsilon_x x)$, where $\upsilon_x = 63\text{cm}^{-1}$.

The zero-order power spectrum in Figure 5-8(c) indicates two components: The Gaussian spike at the origin (0,0) represents the constant DC level and the smaller spikes on the y-axis at (±63,0) represent the single cosinusoidal component. The power spectrum is an even function as should be expected; the input is purely real, its Fourier transform is Hermitian, and consequently its power spectrum should be an even function.

A 2-D cosinusoid, that is constant in the *x*-direction and periodic in the *y*-direction, and its Fourier spectrum, are illustrated in Figures 5-9(a) and 5-9(b) respectively; the spatial frequency components are 0 and 56 cycles/cm along the *x*- and *y*-axis respectively. The input cosinusoid has lines of constant phase parallel to the *x*-axis.

The Gaussian spike at the origin (0,0) in the zero-order power spectrum illustrated in Figure 5-9(c), represents the constant DC level and the smaller spikes on the *x*-axis at (0,±56) represent the single cosinusoidal component.



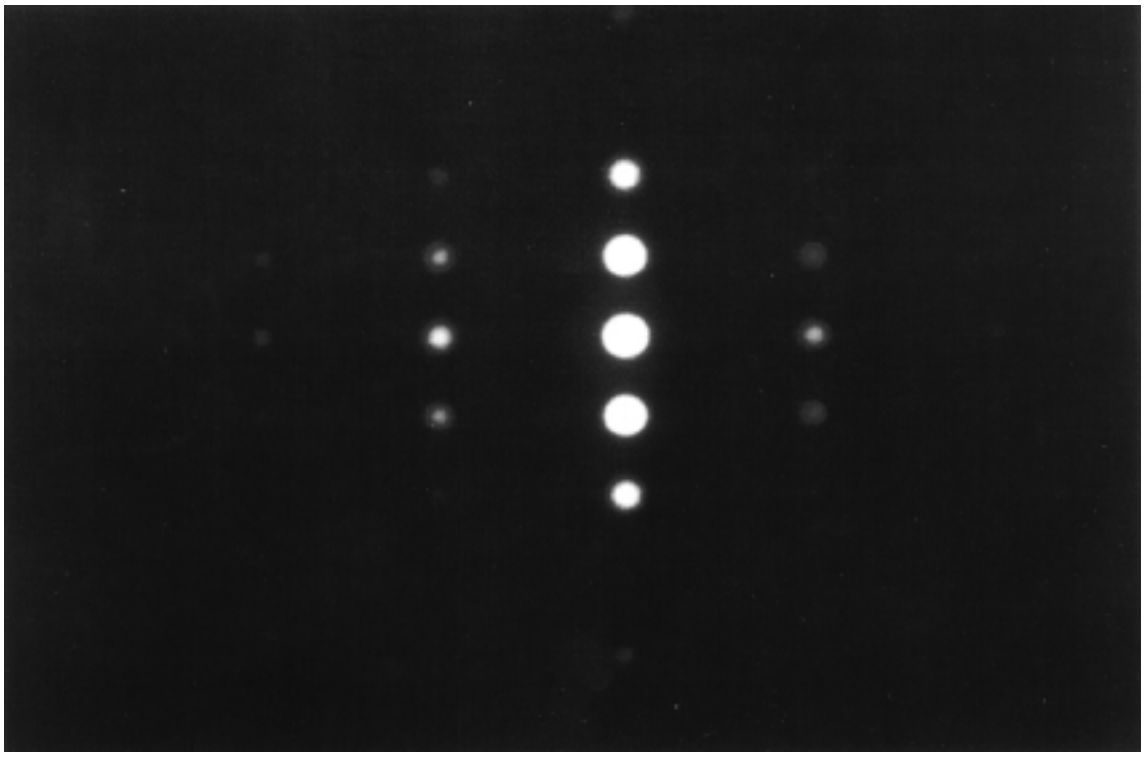


Figure 5-9: The optical Fourier transform (power spectrum) of $f(x,y) = 1 + \cos(2\pi\upsilon_y y)$: (a) The input function written to the SLM, and (b) its optical transform observed in the Fourier plane.

Figures 5-10(a) and 5-10(b) illustrate a 2-D cosinusoid that is periodic in both the *x*- and *y*-directions, and its Fourier spectrum, respectivly; the spatial frequency components are 63 and 56 cycles/cm along the *x*- and *y*-axis respectively. The lines of constant phase make an angle of approximately 45° with the x-axis.

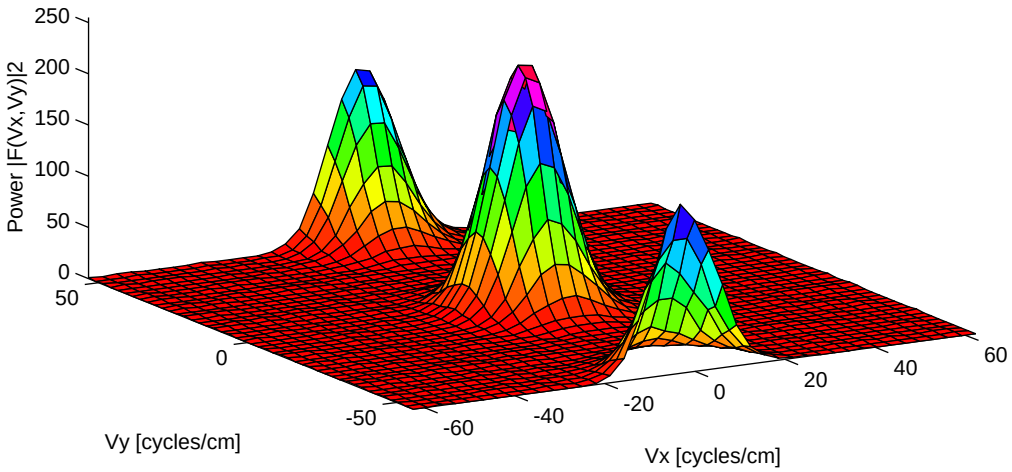
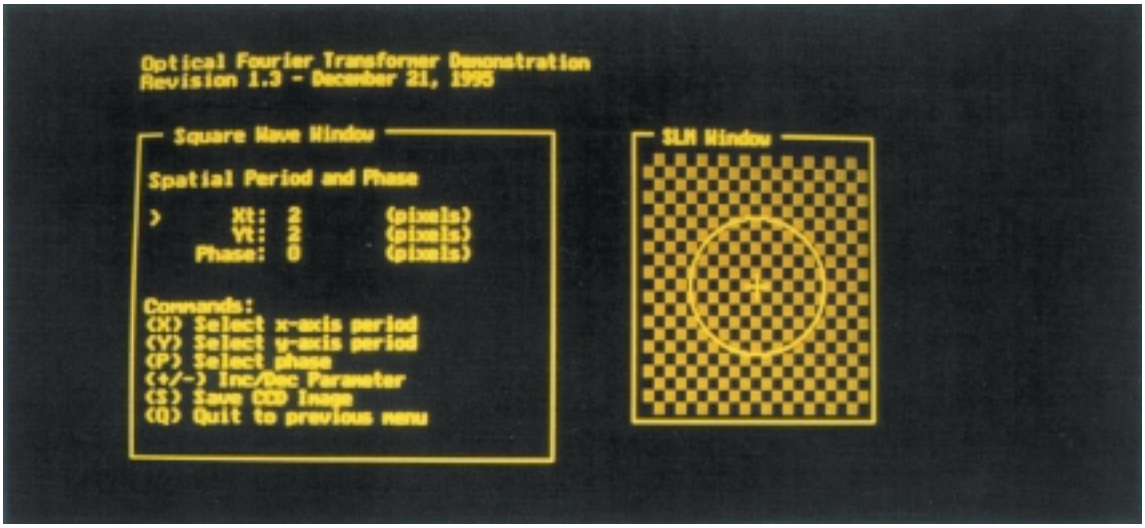


Figure 5-9(c): The zero-order spectrum from Figure 5-9(b). The input function is $f(x,y) = 1 + \cos(2\pi\upsilon_y y)$, where $\nu_y = 56\text{cm}^{-1}$.

Again the Gaussian spike at the origin (0,0) in the power spectrum of Figure 5-10(c) represents the constant DC level. The smaller spikes in the four corners of the xy-plane at (±63,±56) represent the single sinusoidal component. The Fourier transform of a single cosinusoid should produce two, rather than four, spikes in the frequency domain; the two theoretical spikes should lie on a line through the origin whose angle with the ν_x-axis is predetermined by the slope of the input cosinusoid's lines of constant phase.



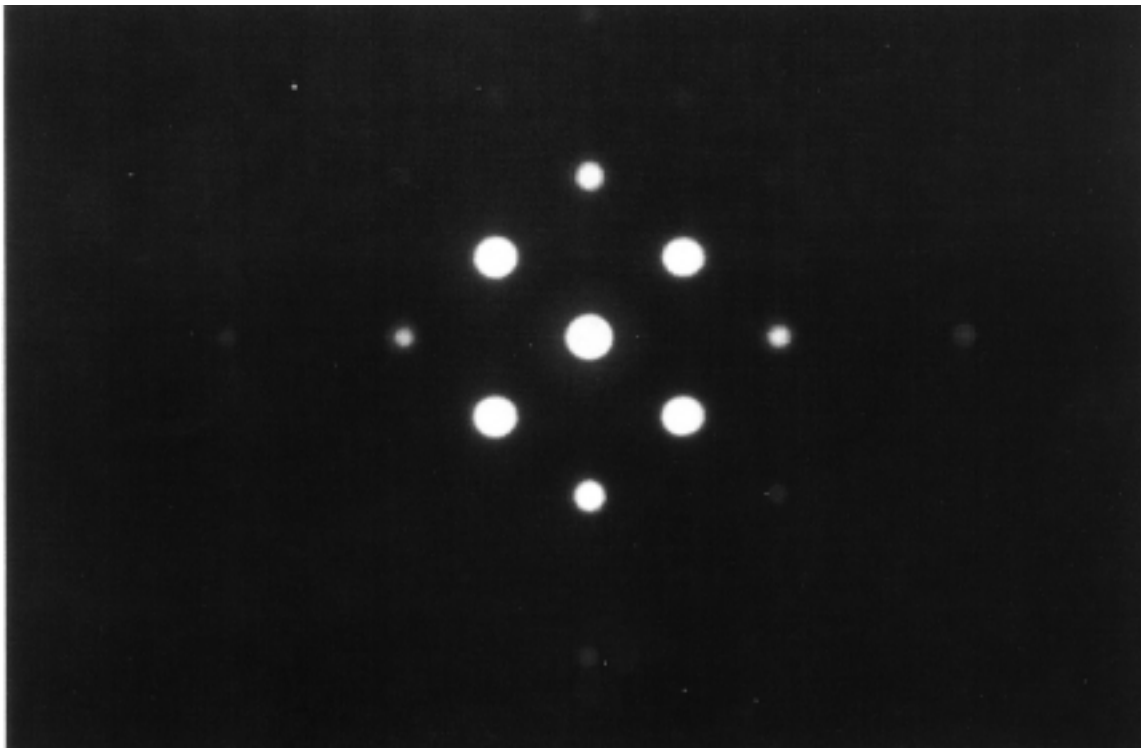


Figure 5-10: The optical Fourier transform (power spectrum) of f(x,y) = cos[2π($\nu_x x + \nu_y y$)]: (a) The input function, and (b) its optical transform observed in the Fourier plane.

The second pair of spikes in the power spectrum of Figure 5-10(c) is an artifact generated by the spatial light modulator. In the limit of the SLM's resolution, cosinusoids placed on the SLM with lines of constant phase inclined at 45° to the *x*-axis are represented as a checker-board pattern rather than cosinusoids with lines of constant phase with either positive or negative slopes; The checker-board pattern is really a superposition of two cosinusoidal functions with reciprocal slopes of constant phase. In the limit of SLM resolution, the optical Fourier transform produces two sets of spike-pairs, one for each of the two cosinusoidal patterns on the SLM.

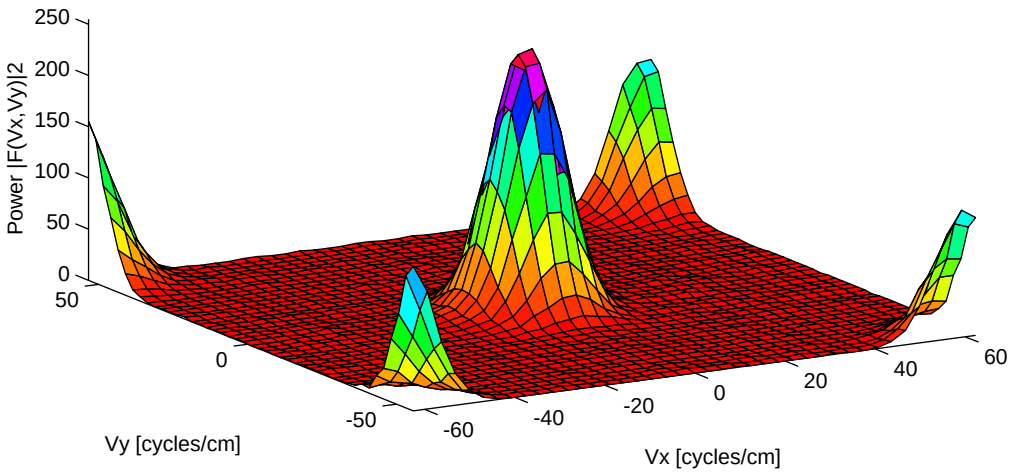


Figure 5-10(c): The zero-order spectrum from Figure 5-10(b). The input function is $f(x,y) = 1 + \cos[2\pi(63x + 56y)]$.

5.3.3 Multiple Cosinusoid Input

Consider the power spectrum of several harmonically related cosinusoids along a particular direction. This input function can be represented mathematically by,

$$f(x,y) = 1 + \sum_{i \equiv \text{odd}} \sin\left(2\pi \nu_i y\right), \qquad \text{[5-21]}$$

where ν_i is the spatial frequency of the i^{th} cosinusoid in the y-direction. The cosinusoids are harmonically related due to the square wave nature of the spatial light modulator input; the fundamental frequency is represented by ν_1 and the odd harmonics are represented by ν_i where i = 3, 5, 7, ... The power spectra of four of these functions were calculated using the optical Fourier transformer and are illustrated in Figures 5-11 through 5-14. The spatial frequency of component cosinusoids and the number of the figure that illustrates its power spectrum, are summarized in Table 5-4.

Table 5-4:
Summary of power spectra containing a constant DC level and several cosinusoids. All spatial frequencies are in cycles/cm.

	Fundamental	Odd Harmonics (3rd, 5th, and 7th)		
	ν_1	ν_3	ν_5	ν_7
Figure 5-11	(1/2) B_y = 27.8			
Figure 5-12	(1/3) B_y = 18.5	(3/3) B_y = 55.6		
Figure 5-13	(1/5) B_y = 11.1	(3/5) B_y = 33.4	(5/5) B_y = 55.6	
Figure 5-14	(1/7) B_y = 8.1	(3/7) B_y = 24.3	(5/7) B_y = 40.4	(7/7) B_y = 55.6



Figure 5-11: The optical Fourier transform (power spectrum) of $f(x,y) = 1 + \cos(2\pi\upsilon_1 y)$: (a) The input function, and (b) its optical transform observed in the Fourier plane.

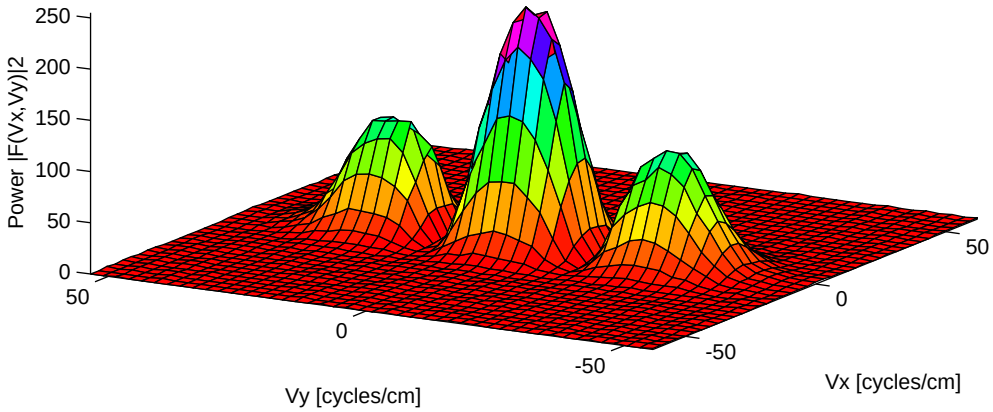


Figure 5-11(c): The zero-order spectrum from Figure 5-11(b). The input function is $f(x,y) = 1 + \cos(2\pi\upsilon_0 y)$, where $\nu_1 = 27.8\text{cm}^{-1}$.

A single cosinusoid with a DC offset and its Fourier spectrum are illustrated in Figures 5-11(a) and 5-11(b). The spatial frequency in the *x*-direction is zero (the *x*-axis spatial frequency component is assumed to be zero for the remainder of this section) and the spatial frequency in the *y*-direction is 27.8 cycles/cm. This corresponds to a 2-D input function with lines of constant phase parallel to the *x*-axis.

The Gaussian spike at (0,0) in the power spectrum of Figure 5-11(c) represents the input function's DC offset, and the two spikes at (0,±27.8) on the *x*-axis represent the single cosinusoid with spatial frequency 27.8 cycles/cm.

A square wave with a pitch of 6 pixels (18.5 cycles/cm) is illustrated in Figure 5-12(a). Its Fourier spectrum consists of two harmonically related cosinusoids with a DC offset as illustrated in Figure 5-12(b) and 5-12(c). The two cosinusoids have spatial frequencies in the *y*-direction of 18.5 and 55.6 cycles/cm and correspond to a three term approximation to an offset square



Figure 5-12: The optical Fourier transform (power spectrum) of $f(x,y) = 1 + \sum\cos(2\pi\upsilon_i y)$: (a) The input function, and (b) its optical transform observed in the Fourier plane.

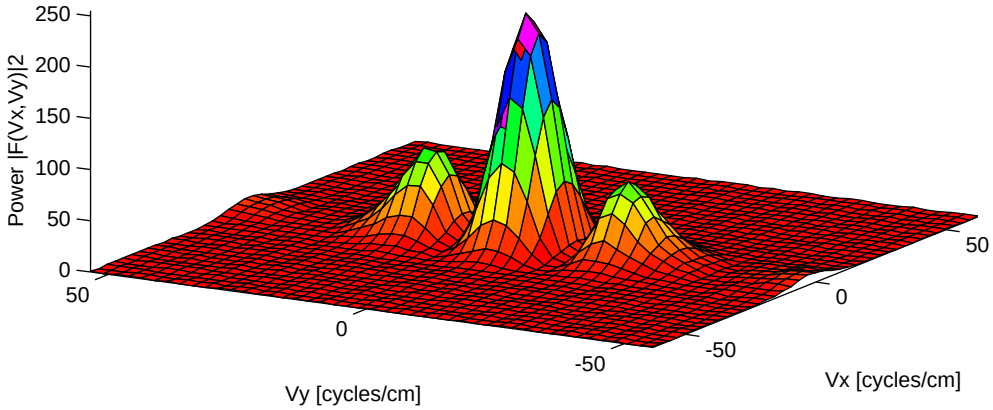


Figure 5-12(c): The zero-order spectrum from Figure 5-12(b). The input function is $f(x,y) = 1 + \sum \cos(2\pi \upsilon_i y)$, where $\upsilon_1 = 18.5$, and $\upsilon_3 = 55.6\text{cm}^{-1}$.

wave with lines of constant phase parallel to the *x*-axis.

There are five Gaussian spikes in the zero-order power spectrum of Figure 5-12(c) corresponding to the DC offset (0,0), the fundamental cosinusoid (0,±18.5), and the third harmonic (0,±55.6). The harmonics are just detectable on the endpoints of the y-axis. Recall that the relative intensities of the components of a square wave are 1, 3^{-2}, 5^{-2}, 7^{-2}, ... where 1 is the amplitude squared of the fundamental, 3^{-2} is the amplitude squared of the third harmonic, and so on. Qualitatively speaking, the amplitude squared, or power, of the Gaussian spikes in Figure 5-12(c), seem to follow this rule.

A square wave with a pitch of 10 pixels (11.1 cycles/cm) is illustrated in Figure 5-13(a). The power spectrum consists of a constant DC offset, a fundamental cosinusoid, and two odd harmonics, and is illustrated in Figure 5-13(b) and 5-13(c). The input function represents a four-term approximation to an offset square wave of fundamental frequency 11.1 cycles/cm.

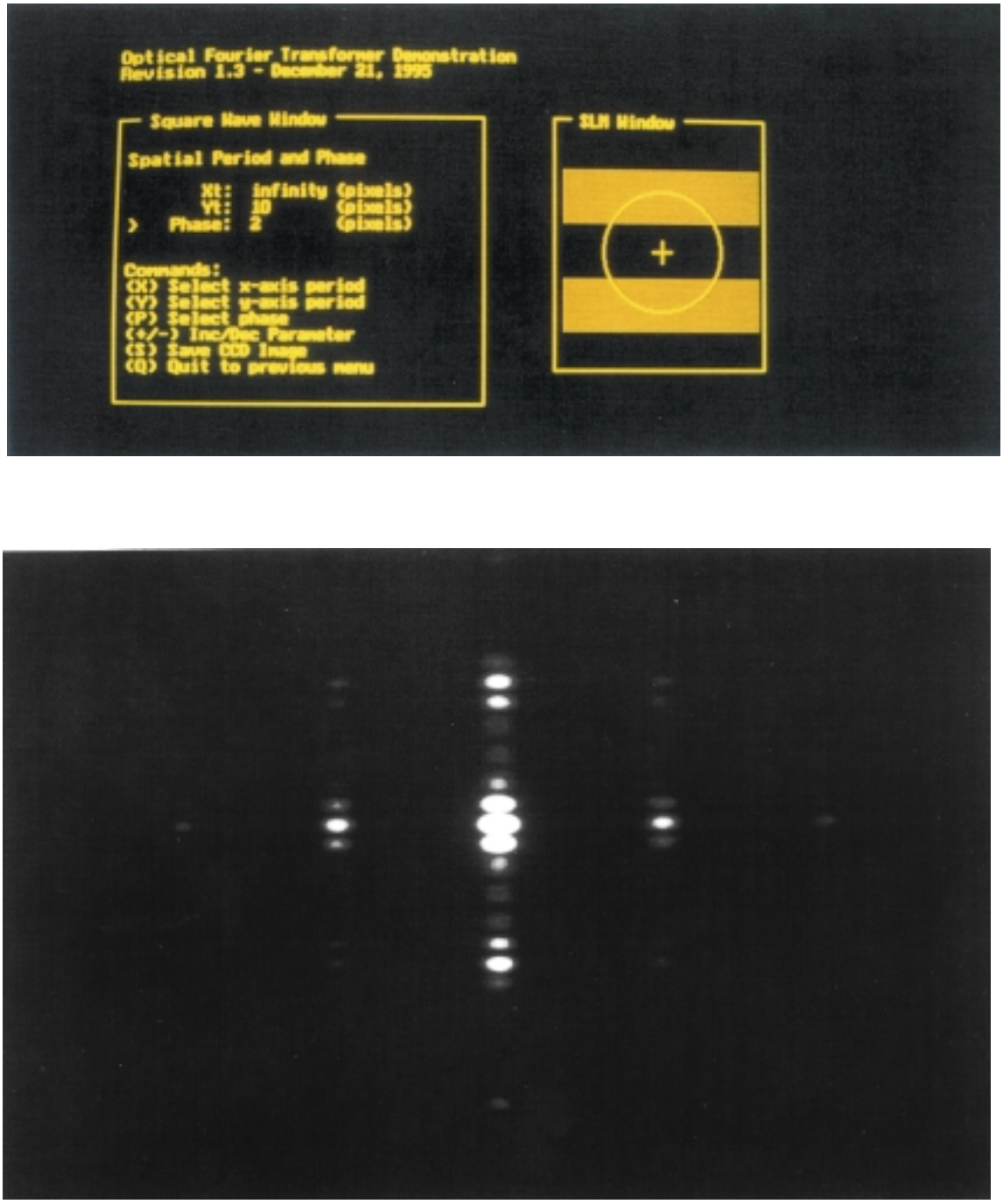


Figure 5-13: The optical Fourier transform (power spectrum) of $f(x,y) = 1 + \sum\cos(2\pi\upsilon_i y)$: (a) The input function, and (b) its optical transform observed in the Fourier plane.

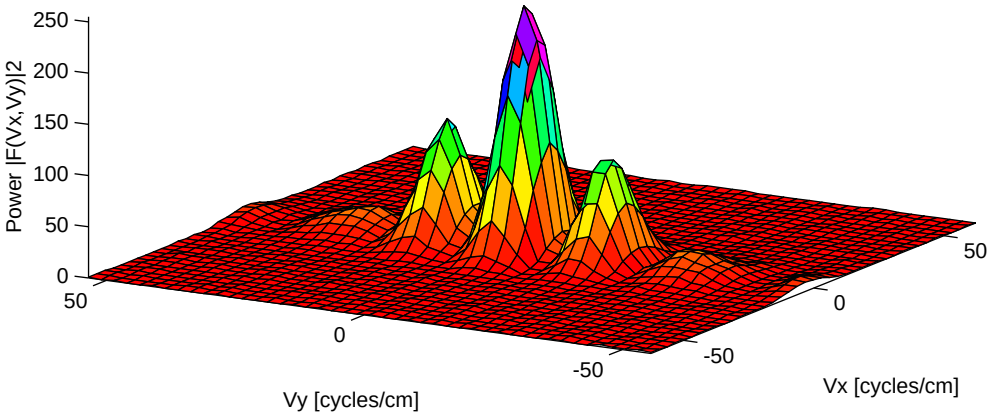


Figure 5-13(c): The zero-order spectrum of Figure 5-13(b). The input function is $f(x,y) = 1 + \sum \cos(2\pi \upsilon_i y)$, where $\upsilon_i = \{11.1, 33.4, 55.6\}$ cm^{-1}.

As expected there are seven Gaussian spikes in the power spectrum of Figure 5-13(c), which correspond to the DC level (0,0), the fundamental frequency (0,±11.1), the third harmonic (0,±33.4), and the fifth harmonic (0,±55.6). The spikes of the fifth harmonic are again just noticeable at the endpoints of the *y*-axis.

The final power spectrum in this series is illustrated in Figure 5-14. A square wave with a pitch of 14 pixels (8.1 cycles/cm) is illustrated in Figure 5-14(a) and its Fourier spectrum, shown in Figure 5-14(b), is built from a superposition of a DC offset, a fundamental cosinusoid at 8.1 cycles/cm, and the next three odd harmonics. The function represents a five term approximation to an offset 2-D square wave.

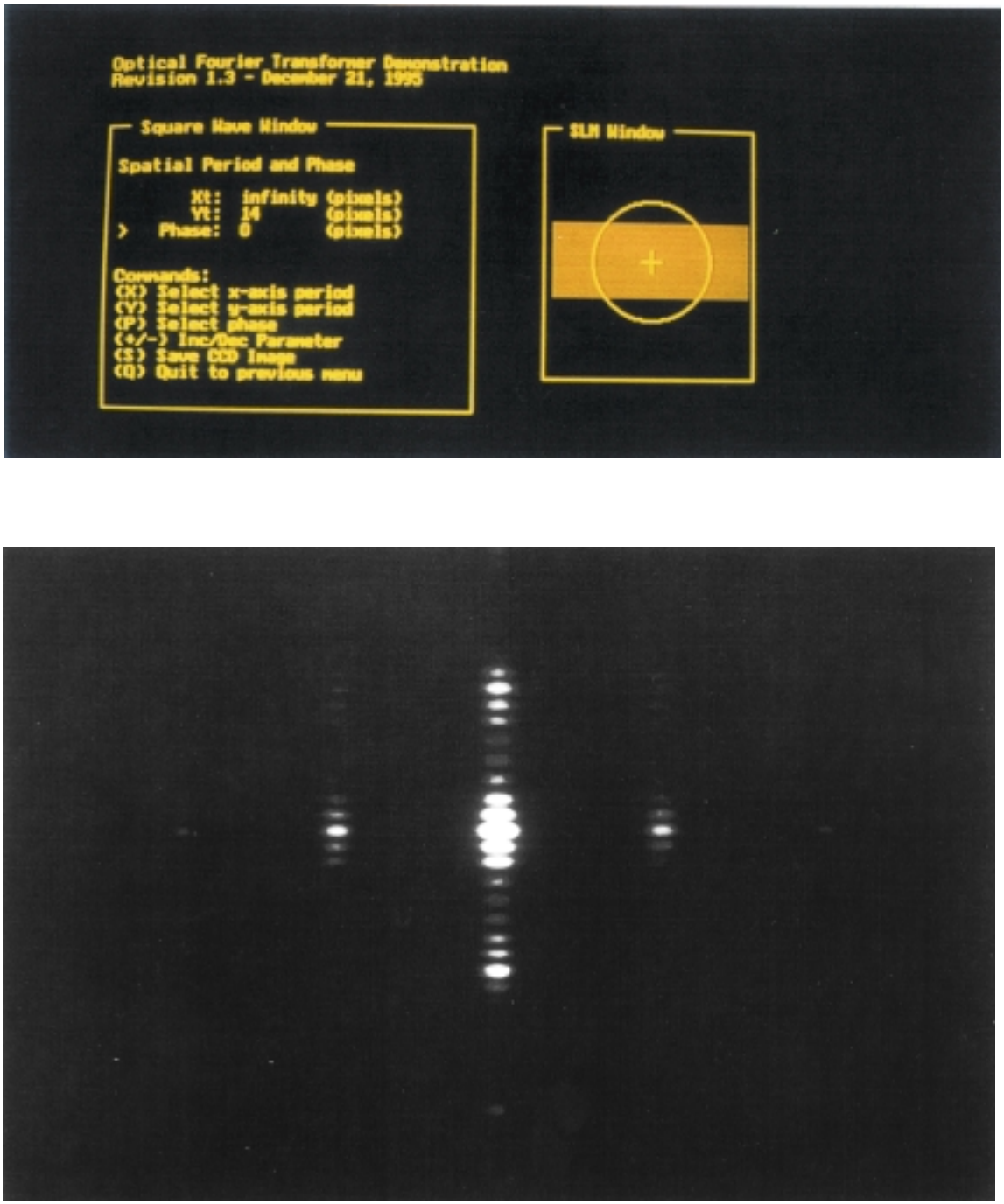


Figure 5-14: The optical Fourier transform (power spectrum) of $f(x,y) = 1 + \sum\cos(2\pi\upsilon_i y)$: (a) The input function, and (b) its optical transform observed in the Fourier plane.

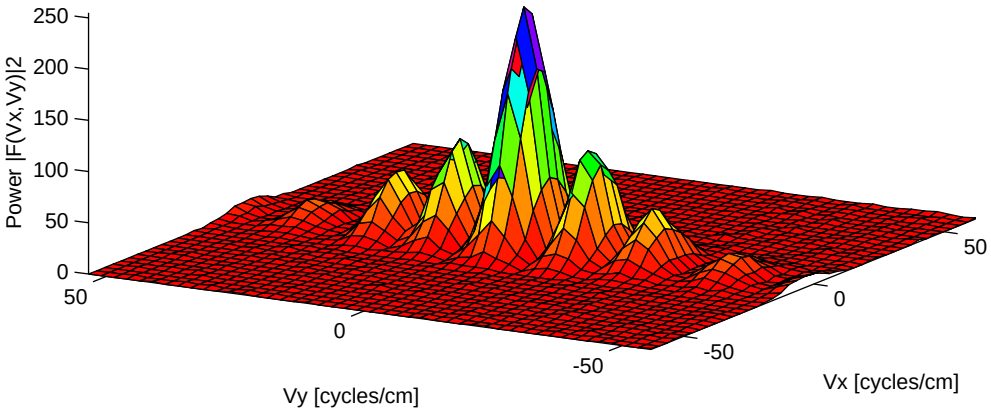


Figure 5-14(c): The zero-order spectrum from Figure 5-14(b). The input function is $f(x,y) = 1 + \sum \cos(2\pi \upsilon_i y)$, where $\boldsymbol{\nu}_i = \{8.1, 24.3, 40.4, 55.6\}$ cm^{-1}.

There are nine Gaussian spikes in the zero-order spectrum of Figure 5-14(c), corresponding to the DC level (0,0), the fundamental frequency (0,±8.1), the third harmonic (0,±24.3), the fifth harmonic (0,±40.4), and finally the seventh harmonic (0,±55.6) at the end points of the *y*-axis.

The power spectra illustrated in Figures 5-14(b) and 5-14(c) represents the limit of resolution of the optical Fourier transformer. The Gaussian spikes in a power spectrum of a six-term approximation to a square wave (fundamental frequency, $\boldsymbol{\nu}_1$ = 6.2 cycles/cm) were not easily resolvable. This observation seems to confirm the calculated frequency resolution of 6 cycles/cm from Table 5-2.

Chapter 6
Summary and Conclusions

A computer-controlled optical Fourier transformer was constructed to demonstrate the computational potential of optical signal processing. The optical processor calculated the Fourier transform, specifically the power spectrum, of arbitrary 2-D input functions at video rates. An arbitrary 2-D input function was written to a twisted nematic liquid crystal display (TN-LCD), which served as a spatial light modulator (SLM), in the front focal plane of a Fourier lens. The output power spectrum was read by a CCD (charge-coupled device) array in the back focal plane of the Fourier lenes. The spatial light modulator was designed to modulate the amplitude of the optical wavefronts incident on it and preserve their phase. Only binary amplitude modulation was possible at each pixel in the spatial light modulator. The CCD array recorded the magnitude squared of the complex amplitude incident on it; the optical processor calculated the power spectrum of an input function and consequently all the phase information of the Fourier transform was lost.

6.1 Analog and Digital Processing

The optical Fourier transform discussed in this work is fundamentally analog in nature whereas the discrete or fast Fourier transform as calculated by a digital system, is by definition digital or discrete. When an analog signal is processed digitally it must first be converted into a discrete form using an analog-to-digital converter (ADC) before it can be processed. Generally the signal is then processed with a discrete Fourier transform (DFT), or another discrete signal processing algorithm, and converted back to an analog form with a digital-to-analog converter (DAC). This digital processing paradigm is illustrated schematically in Figure 6-1(a).

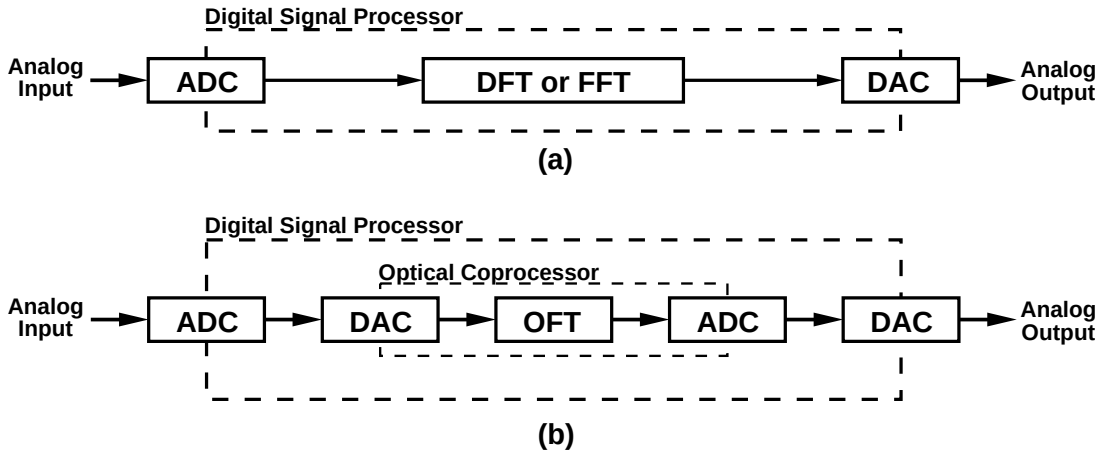


Figure 6-1: Processing an analog signal with (a) a digital signal processor, and (b) a digital signal processor with an optical coprocessor.

Processing an analog signal in a digital architecture with an optical Fourier transform (OFT) coprocessor rather than the discrete Fourier transform (DFT) is illustrated in Figure 6-1(b). Note the back-to-back conversions from analog-to-digital-to-analog at both the input and output of the system. The conversion of the analog signal to a digital format is required only for signal storage and transport; all signal processing is analog in nature. Obviously systems that do not require the intermediate digital signal format can exploit the potential of optical signal processing to a far greater degree.

6.2 Advantages and Disadvantages

The primary advantage of an optical Fourier transformer over a digital implementation is speed. The information throughput that is possible with a massively parallel optical architecture dedicated to Fourier transformation is very impressive. Consider the throughput of a fast Fourier transform (FFT) algorithm implemented in hardware on a dedicated DSP (digital signal processor) chip. The fastest DSP chips at the time of writing could process a complex 1024-point FFT in less than 0.8 ms. This corresponds to an information throughput of

slightly better than one million complex points per second. Now consider an optical Fourier transformer with a 1kHz frame rate equipped with a 1024 by 1024 pixel spatial light modulator and CCD array--these fast high-resolution imaging devices are available today. The information throughput of this optical system is more than one billion pixels per second; this represents an increase in throughput of more than three orders of magnitude over the dedicated DSP chip. The DSP chip is based on VLSI (very large scale integration) which is a relatively mature technology. By comparison optical signal processing is a young technology whose potential has only partially been exploited.

Optical signal processing and the Fourier transformer demonstrated in this work do have some very significant disadvantages over conventional electronic hardware. Optical signal processing has great potential, but the technology required to implement it has not been fully developed. There is a huge infrastructure of conventional electronic computer systems and digital signal processors in the world today: these systems are inexpensive and they work well. The technology is well understood and is nearing maturity. By comparison, optical signal processing is very powerful but it has not been developed to the same extent as has conventional electronics. The technology is not as well understood and development tends to be expensive and slow.

Two other minor disadvantages deserve attention. The hardware associated with optical signal processing tends to be difficult to work with, and more importantly, often quite expensive. Alignment, vibration, humidity and other considerations must be addressed in an optical signal processor but are not as crucial for an electronic digital signal processor. Secondly, a signal that is processed by a series of cascaded operations tends to be more accurate when the processing is done digitally rather than by an analog process. In an analog processor small errors that are introduced in an initial processing state may be

propagated through the system and this error is amplified as the signal moves through the system. The accuracy of a digital processor is limited only by the resolution of its quantization.

6.3 Suggestions for Further Work

There is a very wide scope for further research in the field of optical computing and signal processing. Several suggestions for further work specific to this particular project are outlined below.

6.3.1 Increase Input Plane Size

The resolution of the spatial light modulator used to construct the optical Fourier processor in this work was 320 by 220 pixels. The Helium-Neon laser illuminated a circular region of the SLM roughly equivalent to the beam's diameter; the illuminated region of the SLM had a diameter of about six pixels and consequently less than one percent of the SLMs active area was utilized as the input plane. A properly designed beam expander could increase the diameter of the beam incident on the SLM and at the same time preserve the plane wave nature and Gaussian intensity profile of the beam. A larger spatial domain would allow larger input functions to be written to the SLM and better frequency resolution in the frequency domain as was shown in section 5.1.2.

6.3.2 Spatial Light Modulation

The spatial light modulator used in the optical Fourier processor was designed for binary intensity modulation at video rates. Several improvements could be made here.

Using the same twisted nematic display, gray-scale amplitude or phase modulation is possible according to Gregory [35] and Konforti [49]. Gray-scale amplitude modulation would require the design and construction of new video electronics. Phase modulation (binary or gray-scale) would require the electro-optic transfer function that describes the voltage-phase relationship to be determined (the voltage-transmission curve was illustrated in Figure 4-2). As has been pointed out by Barns [8] and others, non-twisted (sometimes called birefringent) nematic liquid crystal displays are better for phase modulation than the twisted variety used in the current optical Fourier processor.

The power spectrum calculated by the optical Fourier processor was not always even function as would be expected for a real valued input. This leads one to believe that in these isolated cases the Fourier transform was not Hermitian and that the spatial light modulator was independently modulating the phase and amplitude of incident wavefronts. This phenomena could be investigated with possible application to amplitude independent phase modulation.

Ferroelectric liquid crystal spatial light modulators are becoming available off-the-shelf and claim sub-microsecond switching times. A high-speed ferroelectric liquid crystal device could be incorporated into the optical Fourier processor to provide both amplitude and phase modulation, Day [22].

6.3.3 Recovery of Phase Information

Photodetectors such as photodiodes and CCD arrays are responsive to the photon flux (magnitude squared of wavefront amplitude) incident on them, and are insensitive to optical phase. For this reason they are referred to as square-law detectors. It is possible to measure the complex amplitude (magnitude and phase) of an incident wavefront by mixing it with a coherent reference, and

measuring their superposition with a square-law detector. The interference (or beating) between the two fields is reflected in the electric signal provided by the detector and consequently the signal contains information about both the amplitude and phase of the optical signal. When the frequency of the optical signal to be detected is equal to that of the reference, this detection technique is referred to as optical homodyning (or coherent optical detection) as opposed to direct optical detection.

The amplitude and phase information contained in the square-law detector's intensity profile can be fully recovered by interfering a plane wave reference with the Fourier transform at the detector. If a reference with constant amplitude and zero phase delay is interfered with the Fourier transform, the real part of the Fourier transform can be recovered from the intensity profile. Similarly, if a reference with constant amplitude and a 90° phase delay is interfered with the Fourier Transform, the imaginary part of the Fourier transform can be recovered from the intensity profile. Using in-phase and quadrature reference beams and two CCD arrays, the real and imaginary parts of the optical Fourier transform could be measured simultaneously.

List of References

1. Alt, P., and Pleshko, P., "Scanning Limitations of Liquid-Crystal Displays," *IEEE Transactions* on Electron Devices, ED-21(2), pp. 146-155, February 1974.

2. Apt, C., and Little, A., "Perfecting the picture," *IEEE Spectrum*, pp. 60-66, July 1985.

3. Amako, J., "Wave-front control using liquid-crystal devices," *Applied Optics* (32)23, pp. 4323-4329, August 1993.

4. Amako, J., and Sonehara, T., "Kinoform using an electrically controlled birefringent liquid-crystal spatial light modulator," *Applied Optics* 30(32), pp. 4622-4628, November 1991.

5. Anderson, J., et al., Materials Science, London England: Nelson, 1974.

6. Andres, P., et al., "White-light Fourier transformer with low chromatic aberration," *Applied Optics* 31(23), pp. 4682-4687, August 1992.

7. Banerjee, P., and Poon, T., Principles of Applied Optics, Homewood: Irwin and Aksen Associates, 1991.

8. Barnes, T., et al., "Reconfigurable Holographic Optical Interconnections Using a Phase-Only Nematic Liquid Crystal Spatial Light Modulator," *Third International Conference on Holographic Systems, Components and Applications*, Conference paper, pp. 142-146, September 1991.

9. Barnes, T., et al., "Phase-only modulation using a twisted nematic liquid crystal television," *Applied Optics* 28(22), pp. 4845-4852, November 1989.

10. Baur, G., "Optical Characteristics of Liquid Crystal Displays," in The Physics and Chemistry of Liquid Crystal Devices, Edited by Sprokel, G., New York: Plenum Press, 1980.

11. Birecki, H., and Kahn, F., "Accurate Optical Measurement of Small Tilt Angles in Thin Twisted Nematic Layers," in The Physics and Chemistry of Liquid Crystal Devices, Edited by Sprokel, G., New York: Plenum Press, 1980.

12. Born, M., and Wolf, E., Principles of Optics: Electromagnetic Theory of Propagation, Interference and Diffraction of Light, Fifth Edition, Oxford: Pergamon Press, 1975.

13. Bracewell, R., The Fourier Transform and Its Applications, Second Edition, Revised, New York: McGraw-Hill, 1986.

14. Brody, P., "Active-matrix TFTs are in trouble. Cadmium selenide is the answer," *Information Display*, February 1992.

15. Bylander, E., "Liquid Crystal Displays," Chapter 7 in Electronic Displays, New York: McGraw-Hill, 1979.

16. Casasent, D., and Xia, S., "Phase Correction of Light Modulators," *Optics Letters* 11(6), pp. 398-400, June 1986.

17. Clark, N., and Lagerwall, S., "Submicosecond bistable electro-optic switching in liquid crystals," *Applied Physics Letters* 36(11), pp. 899-901, June 1980.

18. Collings, N., et al., "Evolutionary development of advanced liquid crystal spatial light modulators," *Applied Optics* 28(22), pp. 4740-4747, November 1989.

19. Cooper, I., et al., "Dynamic frequency plane correlator," *IEE Proceedings* 133J(1), pp. 70-76, February 1986.

20. Crossland, W., Davey, A., and Vass, D., "Liquid Crystal Spatial Light Modulators For Optical Interconnects and Space Switching," *IEE Colloquium on Optical Connection and Switching Networks for Communication and Computing*, Conference paper, Digest No. 076, pp. 16/1-4, May 1990.

21. Davis, J., et al., "High Efficiency Optical Reconstruction of Binary-Phase Only Filters Using the Hughs Liquid Crystal Light Valve," *Applied Optics* 26(5), pp. 929-933, March 1987.

22. Day, S., "An analysis of phase modulation by liquid crystal elecro-optic effects," *IEE Colloquium on Two-Dimensional Optoelectronic Device Arrays*, Conference paper, Digest No. 158, pp. 8/1-4, October 1991.

23. Doorn, C. van, et al., "Influence of the Device Parameters on the Performance of Twisted-Nematic Liquid Crystal Matrix Displays," in The

Physics and Chemistry of Liquid Crystal Devices, Edited by Sprokel, G., New York: Plenum Press, 1980.

24. Drabik, T., et al., "2D Silicon/Ferroelectric Liquid Crystal Spatial Light Modulators," *IEEE Micro*, pp. 67-76, August 1995.

25. Feitelson, D., Optical Computing: A Survey for Computer Scientists, Cambridge: The MIT Press, 1992.

26. Fukushima, S., Kurokawa, T., and Ohno, M., "Ferroelectric liquid-crystal spatial light modulator achieving bipolar image operation and cascadability," *Applied Optics* 31(32), pp. 6859-6868, November 1992.

27. Fukushima, S., et al., "Bistable spatial light modulator using ferroelectric liquid crystal," *Optics Letters* 15(5), pp. 285-287, March 1990.

28. Gurtler, R., and Maze, C., "Liquid crystal displays," *IEEE Spectrum*, pp. 25-29, Novermber 1972.

29. Garoff, S., and Meyer, R., "Electroclinic Effect at the A-C Phase Change in a Chiral Smectic Liquid Crystal," *Physical Review Letters* 38(15), pp. 848-851, April 1977.

30. Gennes, P.-G. de, The Physics of Liquid Crystals, Oxford England: Clarendon Press, 1993.

31. Gonzalez, R., and Woods, R., Digital Image Processing, New York: Addison-Wesley, 1992.

32. Goodman, J. et al., "Fully parallel, high speed incoherent optical method for performing discrete Fourier transforms," *Optics Letters* 2(1), pp. 1-3, January 1978.

33. Goodman, J., Introduction to Fourier Optics, New York: McGraw-Hill, 1968.

34. Gooch, C., and Tarry, H., "Optical characteristics of twisted nematic liquid-crystal films," *Electronics Letters* 10(1), pp. 2-4, January 1974.

35. Gregory, D., Kirsch, J., and Tam, E., "Full complex modulation using liquid-crystal televisions," *Applied Optics* 31(2), January 1992.

36. Gregory, D., "Real-time pattern recognition using a modified liquid crystal television in a coherent optical correlator," *Applied Optics* 25(4), pp. 467-469, February 1986.

37. Hamilton, M., and Powers, B., "Real-time Joint Transform Correlator with Phase Conjugation for Distortion Correction," *Optics Letters* 12(8), pp. 549-550, August 1987.

38. Hehring, J., and Kmetz, A., "Ultimate Limits for Matrix Addressing of RMS-Responding Liquid-Crystal Displays," *IEEE Transactions on Electronic Devices* ED-26(5), pp. 795-806, May 1979.

39. Heilmeir, G., and Zanoni, L., "Guest-host interactions in nematic liquid crystal: A new electro-optic effect," *Applied Physics Letters* 13(3), pp. 91-92, August 1968.

40. Hughes, K., et al., "Optical preprocessing using liquid crystal televisions," *Applied Optics* 26(6), 1042-1044, March 1987.

41. Inglis, A., Video Engineering, New York: McGraw-Hill, 1993.

42. Jain, A., Fundamentals of Digital Image Processing, Englewood Cliffs: Prentice-Hall, 1989.

43. Javidi, B., et al., "Application of a wire-grid-mirror liquid-crystal light valve in a nonlinear joint transform correlator," *Applied Optics* 33(14), pp. 2834-2841, May 1994.

44. Johnson, J., "White-light optical Fourier transform device," *Applied Optics* 31(23), pp. 4688-4692, August 1992.

45. Juday, R., "Correlation with a spatial light modulator having phase and amplitude cross coupling," *Applied Optics* 28(22), pp. 4865-4869, November 1989.

46. Kitagawa, K., et al., "Mechanism of Misalignment Failure of Liquid-Crystal Display Devices," *IEEE Transactions on Reliability* 40(3), pp. 296-301, August 1991.

47. Kmetz, A., "Liquid-Crystal Display Prospects in Perspective," *IEEE Transactions on Electron Devices*, ED-20(11), pp. 954-961, November 1973.

48. Kobayashi, Y., et al., "Real-time velocity measurement by the use of a speckle-pattern correlation system that incorporates a ferroelectric liquid-crystal spatial light modulator," *Applied Optics* 33(14), pp. 2785-2794, May 1994.

49. Konforti, N., Marom, E., and Wu, S.-T., "Phase-Only Modulation with Twisted Nematic Liquid Crystal Spatial Light Modulators," *Optics Letters* 13(3), pp. 251-253, March 1988.

50. Leenhouts, F., Schadt, M., and Fromm, H.-J., "Electro-optic characteristics of a new liquid crystal display with an improved grey-scale capability," *Applied Physics Letters* 50(21), pp. 1468-1470, May 1987.

51. Lien, A., and Takano, H., "Cell gap measurement of filled twisted nematic liquid crystal displays by a phase compensation method," *Journal of Applied Physics* 69(3), pp. 1304-1309, February 1991.

52. Lien, A., "Simultaneous measurement of twist angle and cell gap of a twisted nematic cell by an optical method," *Conference Record of the 1991 International Display Research Conference*, Conference paper, pp. 192-194, October 1991.

53. Lien, A., "Optimization of the Off-States for Single-Layer and Double Layer General Twisted Nematic Liquid-Crystal Displays," *IEEE Transactions on Electronic Devices* 36(9), pp. 1910-1914, September 1989.

54. Liu, H.-K., and Chao, T.-H., "Liquid crystal television spatial light modulators," *Applied Optics* 28(22), pp. 4772-4780, November 1989.

55. Liu, H.-K., Davis, J., and Lilly, R., "Optical-Data-Processing Properties of a Liquid-Crystal Television Spatial Light Modulator," *Optics Letters* 10(12), pp. 635-637, December 1985.

56. Lu, K., and Saleh, B., "Complex amplitude reflectance of the liquid crystal light valve," *Applied Optics* 30(17), pp. 2354-2362, June 1991.

57. McKnight, D., Johnson, K., and Serati, R., "256 x 256 liquid-crystal-on-silicon spatial light modulator," *Applied Optics* 33(14), pp. 2775-2784, May 1994.

58. McKnight, D., Vass, D., Sillitto, R., "Development of a spatial light modulator: a randomly addressed liquid-crystal-over-nMOS array," *Applied Optics* 28(22), pp. 4757-4762, November 1989.

59. Moddel, G., et al., "High-speed optically addressed spatial light modulator," *Applied Physics Letters* 55(6), pp. 537-539, August 1989.

60. Mok F., et al., "Real-Time Computer-Generated Holograms by Means of Liquid Crystal Television Spatial Light Modulator," *Optics Letters* 11(11), pp. 748-750, November 1986.

61. Morozumi, S., at al., "LCD Full-Color Video Projector," *SID 86 Digest (Society for Information Display, Playa del Rey, Calif.)*, pp. 375-378, 1986.

62. Morozumi, S., et al., "Latest developments in liquid crystal television displays," *Optical Engineering* 23(3), pp. 241-246, May/June 1984.

63. Mukohzaka, N., et al., "Diffraction efficiency analysis of a parallel-aligned nematic-liquid-crystal spatial light modulator," *Applied Optics* 33(14), pp. 2804-2811, May 1994.

64. O'Brien, D., et al., "Dynamic holographic interconnects that use ferroelectric liquid-crystal spatial light modulators," *Applied Optics* 33(14), pp. 2795-2803, May 1994.

65. Oppenheim, A., and Schafer, R., Digital Signal Processing, Englewood Cliffs: Prentice-Hall, 1975.

66. Patel, J., and Werner, K., "Ferroelectrics: ready for prime time?," *Information Display*, pp. 14-16, October 1992.

67. Patel, J., "Electro-optics of ferroelectric liquid crystals," *Optical Engineering* 26(2), pp. 129-133, February 1987.

68. Patel, J., and Goodby, J., "Properties and applications of ferroelectric liquid crystals," *Optical Engineering* 26(5), pp. 373-384, May 1987.

69. Pedrotti, F., and Pedrotti, L., Introduction to Optics, Englewood Cliffs: Prentice-Hall, 1987.

70. Priestly, E., Wojtowicz, P., and Sheng, P., Introduction to Liquid Crystals, New York: Plenum Press, 1975.

71. Sakai, H., and Ohtsubo, J., "Image subtraction using polarization modulation of liquid-crystal television," *Applied Optics* 31(32), pp. 6852-6858, November 1992.

72. Saleh, B., and Teich, M., Fundamentals of Photonics, New York: John Wiley and Sons, 1991.

73. Schadt, M., and Leenhouts, F., "Electro-optical performance of a new, black-white and highly multiplexable liquid display," *Applied Physics Letters* 50(5), pp. 236-238, February 1987.

74. Schadt, M., and Helfrich, W., "Voltage-dependent optical activity of a twisted nematic liquid crystal," *Applied Physics Letters* 18(4), pp. 127-128, February 1971.

75. Scheffer, T and Nehring, J., "Investigation of the electro-optic properties of 270^{o} chiral nematic layers in the birefringent mode," *Journal of Applied Physics* 58(8), pp. 3022-3031, October 1985.

76. Scheffer, T., and Nehring, J., "A new, highly multiplexable liquid crystal display," *Applied Physics Letters* 45(10), pp. 1021-1023, November 1984.

77. Self, S., "Focusing of spherical Gaussian beams," *Applied Optics* 22(5), pp 658-661, March 1983.

78. Tai, A., "Low-cost LCD spatial light modulator with high optical quality," *Applied Optics* 25(9), pp. 1380-1382, May 1986.

79. Toyoda, H., et al., "Real-time displacement measurement using pattern correlation system incorporating an ultra-high-speed shutter camera and parallel aligned nematic liquid crystal spatial light modulators (PAL-SLMs)," *1994 IEEE Instrumentation and Measurement Technology Conference*, pp. 1345-1348, 1994.

80. Underwood, I., et al., "Improving the performance of liquid-crystal-over-silicon spatial light modulators: issues and achievements," *Applied Optics* 33(14), pp. 2768-2774, May 1994.

81. Wheland, G., "Stereoisomerism," Chapter 21 in Advanced Organic Chemistry, 2nd edition, New York: Wiley, 1949.

82. Young, M., "Low-cost LCD video display for optical processing," *Applied Optics* 25(7), pp. 1024-1026, April 1986.